International School for Advanced Studies

Theory and Numerical Simulation of Condensed Matter

Non-Equilibrium Phenomena in Strongly Correlated Systems

Thesis submitted for the degree of

Doctor Philosophiæ

Candidate
Giacomo Mazza

Supervisor
Prof. Michele Fabrizio

Academic year 2014/15

Part I

Introduction

Chapter 1

Non-equilibrium physics in correlated systems

Many phenomena in nature take place far away from thermodynamic equilibrium, ranging from the microscopic processes governing biological systems to large-scale climatic events. Condensed matter systems make no exception to this rule. Indeed, off-equilibrium behaviors often appear in response to external stimuli, such as the coupling to the electromagnetic radiation or the application of driving fields. These represent standard tools for probing solid state systems. Nevertheless, an equilibrium, or at least nearly equilibrium, description revealed to be extremely successful in capturing the main physical properties.

The success of the equilibrium description can be traced back to different reasons. First of all, this is related to the experimental time resolution. In fact, typical observation times are often much longer than those needed to reach an equilibrium state. To fix some number the typical time scales of electron-electron and electron-phonon interactions, responsible of the relaxation, are of the order of $10-100$ fs and 100 fs -10 ps respectively. Moreover, under these conditions, a sufficiently weak perturbation determines only small fluctuations around equilibrium so that the system can be considered for all practical purposes in thermal equilibrium. This fact establishes an important connection between the outcomes of experiments carried out in the so-called *linear response regime* and the equilibrium properties of a solid state system.

In the last decade this scenario acquired a new dimension thanks to a series of major experimental breakthroughs which allowed the investigations of non-equilibrium effects in condensed matter systems and provided a new powerful tool complementary to ordinary quasi-equilibrium experiments.

The application of these new techniques to correlated materials is particularly worthwhile. The properties of these systems are determined by the presence of valence electrons in d or f shells. Because of their more localized nature, these electrons experience a strong Coulomb repulsion, which is at the origin of very unusual physical properties. As a matter of fact, the equilibrium characterization of these compounds led to the disclosure of a plethora of remarkable phenomena among which metal-to-insulator transitions and high-temperature superconductivity are the most striking examples.

The occurrence of a variety of different, and often competing, phases is distinctive of a huge complexity brought-about by the entanglement between different degrees of

freedom (*e.g.* charge, spin, orbital, lattice) whose mutual role, in several cases, still has to be fully clarified. Not surprisingly, the development of various non-adiabatic probing techniques rapidly demonstrated an enormous potential in unveiling a rich off-equilibrium phenomenology for these systems. We may identify two main aspects.

The first one is related to the achievement of a deeper understanding of the basic mechanisms which govern the physics of correlated materials. In particular, the possibility to follow the relaxation dynamics of an excited state provides a unique view on the interactions among the different degrees of freedom taking places over different time scales. This represents a powerful tool for disentangling their different contributions in different regions of a complex phase diagram. On the other hand, the non-equilibrium investigation of correlated materials may lead to the disclosure of new physical phenomena which can not be observed via standard equilibrium probes. For instance, a non-equilibrium perturbation may either induce a dynamical transition between competing phases or push the system into states which are hidden or absent at equilibrium. These kind of phenomena stimulate a lot of interest since they may open the way towards the control of the physical properties of complex materials on very short time scales, a fundamental step for future outstanding technological applications.

In this thesis, we discuss the theoretical description of few relevant cases which represent different examples of non-equilibrium phenomena in correlated materials. In particular, we will focus on the dynamics following a sudden excitation and the coupling to an external driving field.

As a first example we consider the dynamics across a phase transition, namely we explore the possibility of driving a phase transition as the result of a sudden excitation, as *e.g.* the coupling with a short light pulse. We consider systems showing different equilibrium phases and study the conditions under which the off-equilibrium dynamics may lead to non-trivial dynamical phase transitions.

A different case is represented by the dynamics induced by a driving electric field. This problem is particularly relevant for the possible applications of correlated materials in electronic devices. Here we consider the paradigmatic case of a correlated material coupled to external sources which impose a finite bias across the system. We analyze the formation and the properties of the non-equilibrium stationary states in which a finite current flows through the system. This allows us to study the non-linear response properties of a correlated system. In this context, a particularly relevant aspect is the problem of the dielectric breakdown of a Mott insulator, namely the formation of conducting states in the Mott insulating phase. In this thesis we explore different mechanisms leading to such possibility. First we discuss a quantum tunneling mechanism of carriers driven across the insulating gap by the effect of strong electric-fields. Eventually, we discuss the possibility of a resistive transition from an insulating to a metallic state induced by the application of an external electric-field.

In the next two Chapters we give an overview of the experimental and theoretical background useful to contextualize the work reported in the rest of the thesis.

Chapter 2

New perspectives on correlated systems

The development of non-equilibrium techniques in probing condensed matter systems opened new perspectives and opportunities in the challenging investigation of correlated materials. This has been made possible by a series of major experimental breakthroughs which allowed the observation of the relaxation dynamics in condensed matter systems. In this Chapter we review the main experimental facts that triggered a fast increasing interest in the non-equilibrium properties of correlated materials.

2.1 From cold atoms to pump-probe experiments

The progresses in controlling, probing and manipulating ultra cold atomic quantum gases in optical lattices [1] represented crucial steps towards the observation of the non-equilibrium dynamics in quantum many body systems. In these systems it is possible to artificially create almost arbitrary lattice structures, with the opportunity of controlling the interaction strength between atoms either by tuning the scattering length via Feshbach resonances or adjusting the depth of the optical lattice. In this context, the high degree of tunability combined with the almost perfect isolation and the long characteristic time scales ($\sim 0.1 - 100$ ms) give the unique opportunity of observing the unitary quantum dynamics in many-body interacting systems. For instance, in these systems the non-equilibrium dynamics can be accessed following the evolution of the gas after a rapid change of the optical lattice (Fig. 2.1). In general, this procedure also corresponds to a rapid change of the interaction strength between atoms.

In the last decade this kind of experiments pointed out a series of unusual and non-trivial dynamical behaviors in cold atomic gases. These facts boosted an intense theoretical activity focused on the fundamental questions brought about by the unitary evolution of quantum many body systems [2]. A pioneering example is represented by the trapping into long-lived metastable state in a one-dimensional Bose-gas initially split in two coherent wave packets of opposite momentum [3]. This example pointed out a very special dynamical evolution in which the two wave packets recollide periodically, so that the non-equilibrium momentum distribution does not reach a steady state even after several

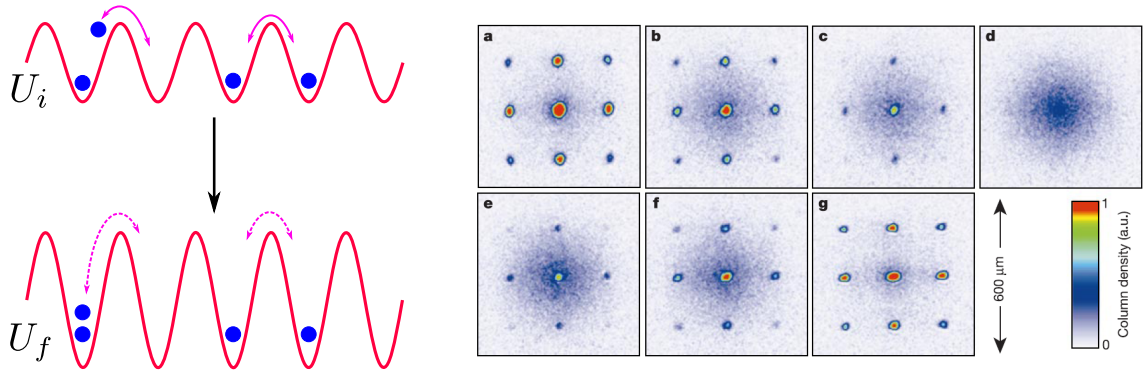

Fig. 2.1: Example of non-equilibrium dynamics in cold atoms experiments. (Left) Sketch of an optical lattice whose depth is suddenly increased. This corresponds to a sudden increase of the interaction strength between atoms. (Right) Adapted from Ref. [4]. Collapse and revival dynamics for a Bose condensate suddenly after a sudden change of the optical lattice depth.

hundreds of oscillations. Another interesting example concerns the dynamics across a phase transition induced in a Bose gas. In this case the system is suddenly driven by changing the optical lattice depth from the weakly interacting superfluid regime to the Mott insulating phase. The resulting dynamics shows that the order parameter does not disappear. Instead remarkable collapse and revival oscillation of the condensate are observed during the time evolution [4] (Fig. 2.1).

Cold atoms systems represent artificial realizations of simple model Hamiltonians describing the low-energy physics of more complex systems. The development of time-resolved spectroscopy techniques allowed to extend the investigation of non-equilibrium dynamics to real solid state materials. Such advancement has been made possible thanks to considerable improvements in the laser technology which considerably pushed forward the experimental time resolutions [5]. This has been made possible thanks to the progresses in handling the light-matter interaction, as *e.g.* the use of coherent light amplification and non-linear optics techniques [6], which enabled the generation of ultrashort laser pulses with femtosecond duration.

Such possibility allowed to induce an *ultrafast* [1] excitation in the system and investigate its relaxation dynamics in the so-called *pump-probe* setup. In these experiments, a short $(10-100$ fs) and intense laser pulse (*pump*) is used to drive out-of-equilibrium the system. A second pulse (*probe*) is sent after a delay time Δt to probe the transient state of the sample. The variation of the delay time Δt allows to study the evolution of the transient state during the relaxation back towards thermal equilibrium (Fig 2.2). With this setup several different techniques have been developed, ranging from pump-probe optical spectroscopy to time-resolved photomession and x-ray diffraction.

The application of these techniques to the study of correlated systems opens new in-

[1] Faster or of the same duration with respect to the fastest (electronic) time scales in a solid state system.

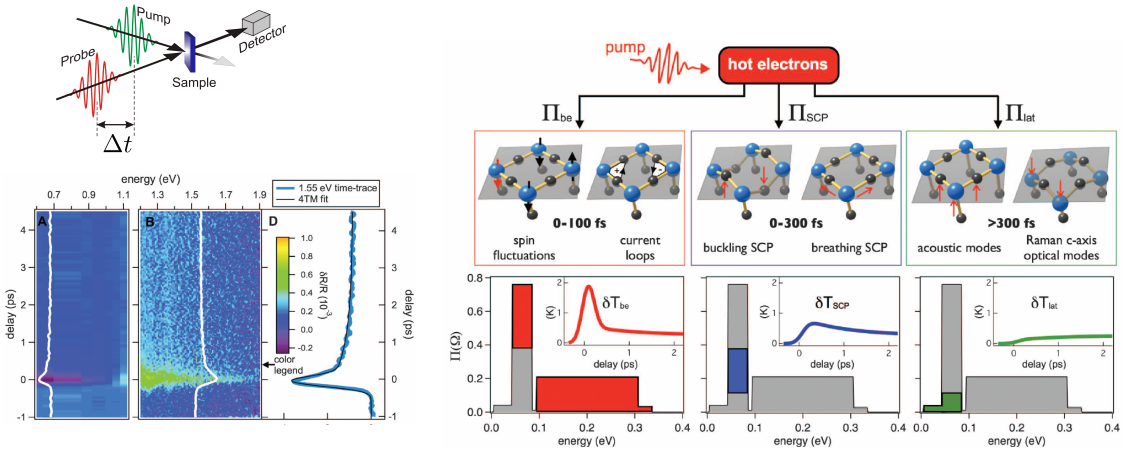

Fig. 2.2: Dynamics in a pump-probe experiment. (Left) Top: Schematic view of a pump-probe setup. The probe pulse (red) is delayed (Δt) with respect to the pump pulse (green). Bottom: Adapted from Ref. [7]. Time- and frequency- dependent reflectivity of the optimally doped $Bi_2Sr_2Ca_{0.92}Y_{0.08}CuO_{8+\delta}$ at $T = 300$ K. (Right) Adapted from Ref. [7]. Various contributions to the phononic glue. The electronic temperature relaxes to its equilibrium value due to the exchange with bosonic excitations at different time scales: Bosonic excitations of electronic origin (red contribution in the left panel; $\tau \sim$ 0-100 fs), phonons strongly coupled with electrons (blue contribution in the middle panel; $\tau \sim$ 0-300 fs) and the rest of lattice phonons (green contribution in the right panel; $\tau >$ 300 fs). The possible various mechanisms determining the bosonic excitations are shown in the the top panels.

teresting perspectives. Indeed, the investigation of the relaxation dynamics of a system excited by an ultrafast pulse can give useful informations on the interplay between the different degrees of freedom. This is because different degrees of freedom are usually characterized by different energy scales. Therefore, the investigation of the response at different time scales opens the possibility of dynamically disentangle the multiple intertwined degrees of freedom. A paradigmatic example is given by the interplay between the electronic and lattice degrees of freedom. In such a situation one can envisage a dynamics in which electron-electron interactions cause a fast thermalization to an high effective temperature of the electron gas [8], which eventually slowly relaxes back due to the electron-phonon interactions. Such hierarchy in the dynamics of a solid can be observed in pump-probe experiments and, for instance, it has been successfully exploited to disentangle the electronic and phononic contribution to the bosonic glue in a high-T_c cuprate superconductor [7] (Fig. 2.2).

2.2 Non-equilibrium investigation of complex phase diagrams

The relaxation dynamics of an excited solid provides a novel point of view on the nature of the competing mechanisms which are usually hidden at equilibrium. On the other hand, the possibility to induce non-equilibrium transient states opens an intriguing scenario for systems excited on the verge of a phase transition or in which the equilibrium state is close to other metastable competing phases. In fact, since transient states can be long-lived or maintained alive by means of driving fields, this possibility may open the way towards the controlled manipulation of complex phase diagrams. In the next sections we give few details on the relevant examples of non-equilibrium investigation of correlated materials' phase diagrams.

2.2.1 High-T_c superconductors and light control of superconductivity

High temperature superconductivity is one of most fascinating phenomena characterizing the phase diagram of many correlated materials. As highlighted by the last example of the previous section, cuprate compounds, due to the elusive nature of the mechanisms which determine their rich phase diagram, represent the ideal playground for investigations in non-equilibrium conditions.

A particularly relevant question in the physics of cuprate superconductors is whether the carrier dynamics is determined by some retarded interaction or is entirely dominated by the high-energy excitations originated from the Coulomb repulsion. In this respect the use of the time-resolved spectroscopy can give valuable insights. For instance, the analysis of the transient reflectivity in the compound $Bi_2Sr_2Ca_{0.92}Y_{0.08}CuO_{8+\delta}$ revealed the presence of high-energy excitations underlying the superconducting transition [9]. On the other hand, the direct observation of the retarded interaction between electrons and bosonic excitations of antiferromagnetic origin building up, in the normal phase, on the femtosecond scale has been reported in a recent experiment [10]. Other important non-equilibrium investigations of cuprate compounds involve the use of time- and momentum-resolved techniques. For instance, the strong momentum space anisotropy of cuprates has been shown to reflect into a strongly anisotropic recombination rate of Cooper pairs after an ultrafast excitations [11]. Conversely, a peculiar suppression and recovery dynamics of coherent quasi-particles suggested a non-trivial relation between nodal excitations and superconductivity which is hidden at equilibrium [12]. In this same context, the interplay between electronic correlations and the pseudo-gap physics has been revealed observing the evolution of photo-induced antinodal excitations [13].

These examples represent a non-exhaustive list of the possible insights on the strongly debated phenomenon of high-temperature superconductivity achievable from the observation of the relaxation dynamics on very short time scales. Another intriguing application of the time dependent techniques is related to the active light manipulation of such state of matter. A pioneering experiment in this direction showed the occurrence of a transient

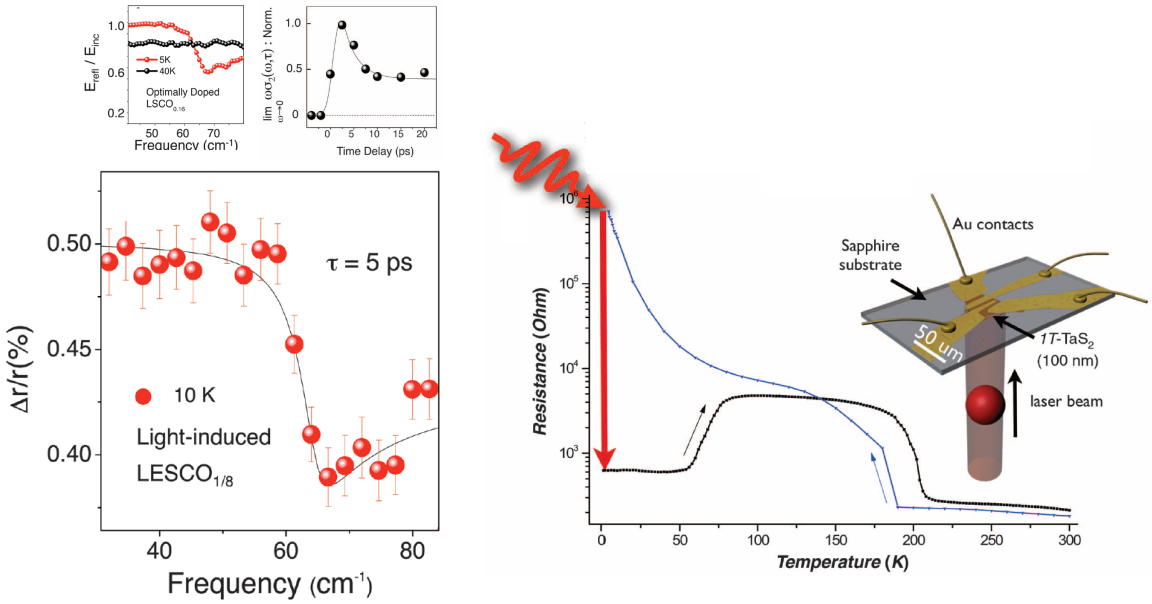

Fig. 2.3: Examples of photo-induced transition in correlated materials (Left) Adapted from Ref. [14]. Light induced superconductivity in the cuprate compound $La_{1.675}Eu_2Sr_{0.125}CuO_2$. Main plot: transient $c-$axis reflectance measured with respect to the unperturbed one after $\tau = 5$ ps the excitation pulse at $T = 10$ K where the unperturbed system is stripe ordered. The appearance of a Josephson plasma edge at $\sim$ 60 cm^{-1} signals the transient superconducting state. The equilibrium reflectances in the superconducting and insulating system are reported in the top left panel. The time-stability of the condensate is shown in top right panel. (Right) Adapted from Ref. [15]. Drop of the resistivity in tantalum disulfide $1T - TaSa_2$ at $T = 1.5$ K caused by a single 35 fs pulse with fluence $\sim$ 1 mJ/cm^2. The black arrow indicates the stability of the light-induced transition upon temperature increase.

superconductive state in the cuprate compound $La_{1.675}Eu_2Sr_{0.125}CuO_2$ [14] appearing after a mid-infrared pulse excitation. This transient state is detected by the appearance of a sharp Josephson plasma resonance (Fig. 2.3 left) in the $c-$axis transient reflectance and it has been shown to last longer than 100 ps after the excitation. This occurrence has been addressed to the melting of the striped phase which is the stable phase of the system and which prevent superconductivity in equilibrium conditions [16].

Furthermore, experiments focusing on the transient dynamics induced in the bi-layer compound $YBa_2Cu_3O_{6+x}$ above the superconducting critical temperature T_c, showed that the transient state is characterized by unusual spectroscopic properties qualitatively similar to the redistribution of spectral weight observed at the equilibrium superconducting transition [17, 18]. This has been interpreted as a fingerprint of an enhancement of the transport coherence. Such interpretation is prone to a suggestive translation to the hypothesis of a light-induced superconducting states extending far above T_c [18]. Such kind of experiments are not only related to cuprate compounds but have recently addressed the transient dynamics in the organic compound K_3C_{60} [19]. Potentially such occurrences may have an enormous impact in the field of high-temperature superconductivity. Nevertheless, the current issue is strongly debated. Few indications in this directions come

from the analysis of the non-linear lattice dynamics induced by the pump pulse [20] and even less theoretical results are available at this stage.

2.2.2 Photo-induced Mott transitions

The fingerprint of strong correlation is the presence of sharp metal-to-insulator transitions induced by the change of external parameters, *e.g.* temperature, pressure or chemical doping. Interestingly, ultrafast injection of electronic excitations can also be used to induce an insulator-to-metal Mott transition. The latter can be either associated to the fast redistribution of carriers or to a sudden increase of the effective temperature.

This possibility was first realized in halogen-bridged Nickel chain charge transfer insulator. The appearance of a strongly renormalized gap and finite sub-gap conducting state were detected after the ultrafast light stimulation of the insulating state [21]. This was related to carriers injected by photo-doping which eventually recombine driving the relaxation towards the originally gapped state in few picoseconds. The formation of sub-gap quasi-particle excitations has been also detected in archetypical Mott insulator compound La_2CuO_4 excited across the charge-transfer gap. Analogously, the ultrafast response displays transient features similar to small doping variations [22].

A similar experiment carried out using the time-resolved photoemission technique highlighted the instantaneous collapse and recovery (within 1 ps) of the insulating gap in the quasi-two dimensional layered compound $1T-TaSa_2$ [23]. In this case the driving mechanism was related to the heating of the electronic cloud rather than to the photo-injection of carriers. On the same compound, a subsequent experiment revealed the sudden drop of about three order of magnitude of the electrical resistivity following the sudden excitation ($\tau \sim 30$ fs) of the insulating charge ordered state, which is thermodynamically stable at the very low temperature of $T = 1.5$ K [15] (Fig. 2.3 right). Strikingly, this sudden drop was found to be stable in time, up to one week, and robust against the temperature increase up to $T \sim 100$ K. These observations were interpreted invoking the effect of photo-injected carriers which, instead of relaxing back to the originally gapped state, drive the reorganization of charge order with the formation of domain walls that stabilize the pulse-induced transient state.

More recently, a long-lived induced metallic state accompanied by the sharp collapse of the insulating gap has been revealed in a VO_2 compound using time resolved photoemission spectroscopy [24]. Interestingly, also in this case photo-doping has been invoked to explain this result. However, in this case the photo-injected carriers result in a strong increase of the Coulomb interaction screening which in turn is responsible of the transition.

2.2.3 Electric-field induced dielectric breakdown

Application of electric fields is maybe the oldest perturbation used to destabilize an insulating state in favor of a conducting one. In ordinary semiconductors this happens through the carriers promotion from valence to conduction band due to quantum tunneling [27]. This mechanism represents one of the building blocks of semiconductor based electronics. The idea of inducing the same kind of transition in Mott insulators opens an interesting

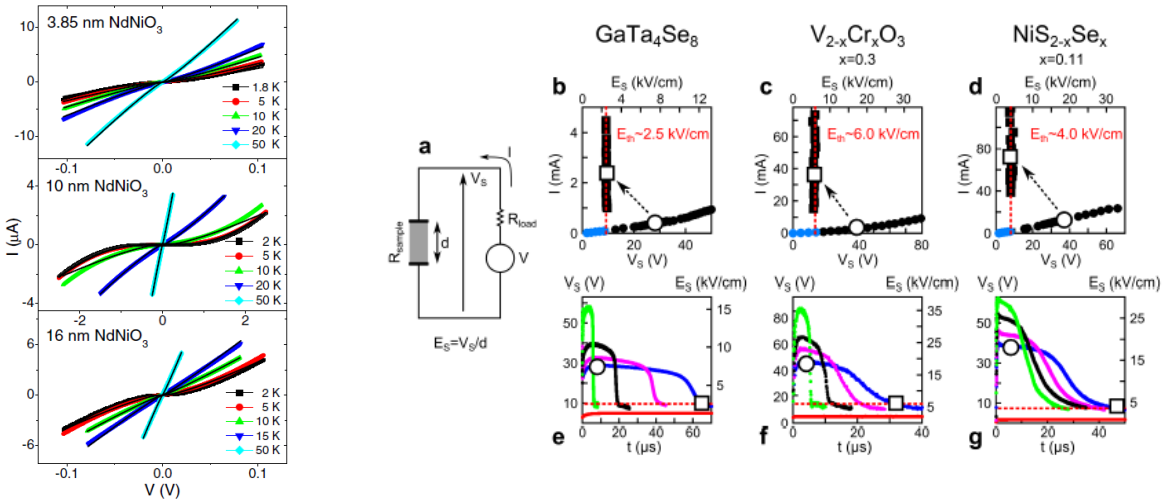

Fig. 2.4: Tunnel-breakdown VS resistive switch. (Left) Adapted from Ref. [25]. Current-bias characteristics in $NdNiO_3$ thin films. The linear behavior in the high-temperature metallic phase (light blue curve) turns into an exponential activated one in the low temperature insulating phase (black curve). This occurrence suggests a tunnel-like formation of conducting states (see Sec. 3.2.2). (Right) Adapted from Ref. [26]. Resistive switch in three paradigmatic Mott-insulators. Bottom panels: Voltage-drop across the samples while a series of pulses of different duration and intensity are applied (in each panel the intensity increases from right to left). After a certain delay time the samples undergoes a fast transition between high and low resistance states. Top panels: Current-bias characteristics before and after the breakdown. These latter shows an almost vertical behavior at a threshold field E_{th}.

scenario on the search for novel technological applications beyond standard , *i.e.* Si-based, electronics [28]. Indeed, while in ordinary semiconductors the insulating behavior is fixed by the chemistry and lattice structure, the gap in a Mott insulator is a collective property originated by the electrons mutual repulsion. Thus, an hypothetical electric field driven insulator-to-metal transition is expected to suddenly free all the previously localized electrons, driving the formation of a completely new kind of electric breakdown mechanism. Governing this effect has an immense impact to the engineering of new generation devices, which could overcome the current limitation of the semiconductor-based technology, such as *e.g.* the device miniaturization which is restricted by fundamental physical effects such as the carrier density fluctuations [29].

The experimental study of this possibility based on different Mott insulating compounds or oxide based prototype devices, pointed out the existence of different breakdown mechanisms [30]. These can hardly by understood in terms of a universal theoretical description, nevertheless a schematic organization can be derived.

The simplest way to use an electric field to turn the Mott insulating state into a metallic one is to induce a change in the carrier concentration. This can be done in field-effect transistors which use a double-layer gating setup [31]. In the case of devices built with wide-gap Mott insulators as Ni [32] or Cu [33] monoxides, the systems were shown to acquire a very bad metallic character with performances even worse than conventional

semiconducting devices. On the other hand, a completely different result has been observed in a similar setup built with VO_2 [34]. Indeed, in this case massive conducting channels in the bulk of the system appear as a consequence of a relatively small charge surface accumulation.

The direct application of electric-fields in Mott-insulator leads to a likewise diversified phenomenology. For instance, the conducting properties of thin films of $NdNiO_3$ [25], investigated well below the metal-to-insulator transition temperature, reveal an exponential current activation which suggests a tunnel-like formation of conducting states (Fig. 2.4 left). On the contrary, several examples of avalanche-mechanism driving the dielectric breakdown under the application of electric field are known. For example, this has been firstly observed in one- (Sr_2CuO_3 and $SrCuO_2$) [35] and two- ($La_{2-x}Sr_xNiO_4$) [36] dimensional Mott insulators, where in the latter case the breakdown was related to the depinning of the charge ordered state. Moreover, a similar mechanism has been revealed in the organic Mott insulator $\kappa - (\text{BEDT-TTF})_2\text{Cu}[\text{N}(\text{CN})_2]\text{Br}$ [37].

More recent experiments on narrow gap Mott insulators V_2O_3, $NiS_{2-x}Se_x$ and $GaTa_4Se_8$ [26, 38] showed the possibility to trigger a very fast transition from an high- to a low-resistance state (Fig. 2.4 right) by means of electric-field pulses of different durations and intensities. Remarkably, the observed threshold fields are orders of magnitude smaller than what expected from a simple estimation based on the insulating gap. The presence of metastable metallic phase which nucleate under the effect of the electric field and generate the avalanche mechanism has been invoked to explain such occurrence [26, 39].

The presence of metastable phases can be crucial for the transition driven by the application of external fields. Indeed, recent results in two-dimensional crystals of tantalum disulfide $1T-TaSa_2$ highlighted the possibility to induce by means of an external bias a cascade of resistive transitions corresponding to different metastable states [40].

Chapter 3

Theoretical description of non-equilibrium phenomena and overview of the main results

The fast development of the experimental investigation of correlated systems in non-equilibrium conditions has not been sustained by an equivalent rapid development of the theoretical understanding. Despite a number of results have been put forward in this context, many challenges, even at a fundamental level, are still open and call for further investigations. The slowing down of the theoretical investigation of non-equilibrium physics is related to major methodological challenges in describing both correlation effects and large perturbations, *i.e.* beyond the linear response regime, with the same level of accuracy.

Major difficulties come from the fact that far from equilibrium it is not possible to describe the physical properties of a system in terms of its ground state and low-lying excited states. At equilibrium this is possible because the relevant excited state that determine the physical properties are automatically selected by the temperature. On the contrary, the non-equilibrium properties of a system are determined, in principle, by an arbitrary number of excited states. Therefore, the distribution function is not set by temperature, being instead determined by the dynamical evolution of the system itself. Evidently, this requires a more extended knowledge to fully characterize the non-equilibrium state of the system.

On the other hand, the effects of strong correlations cannot be taken into account within a single particle picture. Despite the huge progresses made in the last decades, a comprehensive description of correlated systems still represents a major challenge even in equilibrium conditions. As a consequence, the theoretical investigation of non-equilibrium phenomena in correlated systems requires to merge these two aspects, giving rise to a tremendously difficult problem to tackle. In the last years a big effort has been devoted to develop new ideas and techniques which enabled the investigation of the off-equilibrium dynamics of strongly correlated system.

In the following we shall discuss some of the recent theoretical results. The focus is on the dynamics following sudden excitations and the problem of non-equilibrium transport induced by external driving fields. These are the main subjects of the work reported in

the rest of the thesis, which we shall introduce at the end of the Chapter.

3.1 Response to sudden excitations

3.1.1 Quantum quenches and dynamical transitions

The simplest theoretical framework for describing the dynamics following an ultrafast excitation of the system is the so-called *quantum quench* protocol, namely the dynamics following the sudden change of a control parameter. In practice, given an Hamiltonian $\mathcal{H}(u_i)$ which depends on a parameter u_i with ground state $|\Psi_i\rangle$, the quench dynamics corresponds to the evolution of the initial ground state of $\mathcal{H}(u_i)$ with a different Hamiltonian $\mathcal{H}(u_f)$, being $u_f \neq u_i$. Rephrasing this statement, the quench protocol corresponds to the evolution of an initial excited state which mimics the effect of the instantaneous injection of electronic excitations following the coupling to an intense ultrashort laser pulse. It is important to note that in most cases the quench dynamics is limited to *isolated system*. Therefore this approach represents a reliable approximation of the transient dynamics in real systems only for the very early times when the dynamics is still not affected by the thermal path.

Despite the simplicity of the protocol, the dynamics of an initially excited state in an isolated system poses serious questions which are actually at the basis of the quantum statistical mechanics [41]. The central issue concerns the problem of *thermalization*, namely the relaxation towards a thermal equilibrium state. In this case, the naïve expectation is that the initial energy injection should translate into an effective heating of the system. Therefore the system relaxes to a state with an increased effective temperature. However, the unitary quantum evolution cannot describe the relaxation to equilibrium of a pure state to a thermal one, which corresponds by its definition to a mixed state. To overcome this limitation, suitable extension of this simple concept of thermalization have been introduced considering, for example, the relaxation of few observables to the value predicted by a Boltzmann-Gibbs ensemble at an effective temperature:

$$\lim_{t\to\infty} \frac{1}{t} \int_0^t d\tau \langle \Psi(\tau)|\mathcal{O}|\Psi(\tau)\rangle = \mathrm{Tr}\left[\rho_{eff}\mathcal{O}\right] \quad \text{with} \quad \rho_{eff} = e^{-\beta_{eff}\mathcal{H}}. \tag{3.1}$$

Although several ideas have been introduced so far [42, 43], the true mechanisms leading to thermalization are still not fully clarified and, as a matter of fact, in several cases thermalization has been shown to be slowed down [44, 45] or even absent [46, 47]. Indeed, relaxation towards a stationary state is often characterized by non-trivial dynamical evolutions, with the trapping into long-lived metastable states and the appearance of different dynamical regimes featuring different time scales. Different dynamical regimes can also be sharply separated by some critical points which define the so-called *dynamical transitions* [48–50]. A paradigmatic example is given by the interaction quench dynamics in the single band Hubbard model, which corresponds to the dynamics of an uncorrelated Fermi sea in the presence of a local electron-electron repulsion [44, 48, 49]. This dynamics was initially addressed using a perturbative approach based on the flow equation method

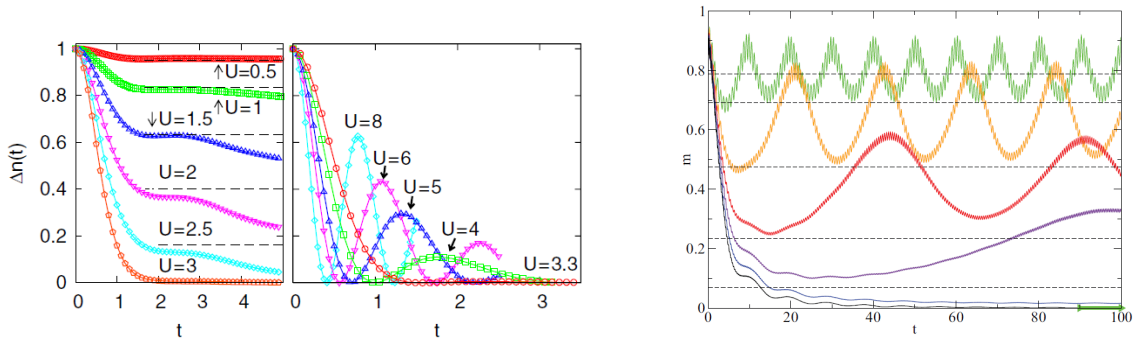

Fig. 3.1: Examples of dynamical transition and dynamics across a phase transition. Left: Adapted from Ref. [48] Dynamical transition in the half-filled single band Hubbard model within non-equilibrium DMFT. The dynamical transition is signaled by the fast thermalization of the jump at the Fermi-level for $U \approx 3.3$ and the appearance of a collapse and revival dynamics in the strong quench regime. Right: Adapted from Ref. [51]. Quench dynamics of the staggered magnetization in the half-filled Hubbard model studied within time-dependent Gutzwiller Approximation. Non thermal ordered states display a finite long-time order parameter (dashed lines) whereas the corresponding effective temperature is larger than the Néel one, as shown by the zero thermal value of the order parameter highlighted by the arrow.

[44] and later within the framework of Dynamical Mean Field Theory (DMFT) [48] and the Gutzwiller approximation [49]. The results of such investigations revealed that for weak quenches the system gets trapped at long times into a quasi-stationary regime in which quasi-particles are formed with a finite jump non-equilibrium distribution function that only on a longer time scale has been argued to approach a Fermi-Dirac distribution at finite temperature [44]. A sharp crossover at intermediate value U_c^{dyn} at which fast thermalization occurs, indicates a dynamical transition towards a strong quench regime in which the dynamics shows collapse and revival oscillations [48, 49] (Fig. 3.1 left).

The existence of a dynamical critical point have been reported in several models [52–56], showing that the dynamics after a sudden excitation cannot be simply related to an increase of the effective temperature. This circumstance is particularly relevant for another interesting class of quench dynamics, those across a phase transition for which a given symmetry may be broken or restored during the unitary evolution. Paradigmatic examples include the dynamics of the ferromagnetic order parameter in the fully connected Ising model [57, 58] or the dynamics of the antiferromagnetic (AFM) order parameter [51, 59, 60] which at zero-temperature is stabilized by the effect of electron-electron repulsion. In particular, in this latter case it has been shown that for quenches both to weaker and to stronger interaction parameter, long-lived ordered states exist despite the fact that their expected effective temperature is above the Néel transition (Fig. 3.1 right). These examples show that the unitary dynamics in isolated systems may lead to stable ordered states which can not be reached through conventional thermal pathways. The understanding of the mechanisms governing such non-equilibrium transitions is the starting point for the investigation of the possible dynamical transitions induced by ultrafast

excitations in more complex models.

3.1.2 Dynamics in photo-excited systems

A more realistic description of the dynamics following an ultrafast excitation requires to consider the coupling between the correlated system and a short pulse of electromagnetic radiation. The coupling with the light pulse induces a sudden redistribution of the carriers that may strongly modify the state of the system, possibly leading to the formation of long-lived metastable phase sustained by a slow recombination rate. As we discussed in the previous Chapter, a particular relevant case is that of the photo-excitation of a Mott insulator. In fact, the photo-injection of high energy excitations may drive the transition towards transient [21, 23] or stable [15, 24] metallic phases.

The nature of the photo-induced states in Mott insulator has been investigated within the framework of the single band Hubbard model [61, 62]. It was shown that the approach to the steady state becomes exponentially slow as the interaction is larger than the bandwidth because of the inefficient recombination of electron-holes pairs [63, 64]. The long-lived transient state is characterized by a pump-induced transfer of the spectral weight from the lower to the upper Hubbard band similar to the effect of the temperature increase [61]. Moreover, the direct comparison between the chemically doped and the photo-doped Mott insulators reveals that the latter is characterized by bad conducting properties with a very low-mobility of the photo-doped carriers [62]. These results show that within this description the pump excitation induces a small modification of the electronic properties of the insulating state. Therefore, a true photo-induced Mott transition, as *e.g.* observed in Ref. [24], is not retrieved within this framework.

A different point of view has been taken in Ref. [65] considering a more realistic toy-model shaped on the electronic structure of the archetypal compound V_2O_3 [66]. It is shown that, due to the presence of additional orbital degrees of freedom, the photo-induced excitations across the gap are indeed able to drive a transition to a stable metallic state driven by the sudden melting of the insulating gap [65]. These results open new interesting perspectives for the description of the photo-induced excitations in correlated systems.

3.2 Non-linear transport in strong electric fields

Another crucial aspect is related to the class of experiments probing the effects of strong electric fields (see Sec. 2.2.3). In this case, we can identify two main theoretical issues which are object of intense investigations, namely the approach and formation of non-equilibrium stationary states and the mechanisms leading to the breakdown of the insulating state.

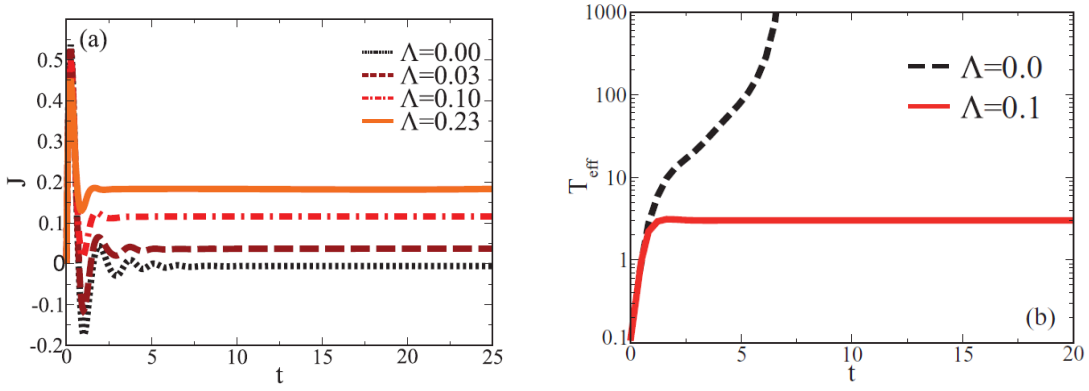

Fig. 3.2: Approach to a stationary state in the driven Hubbard model. Adapted from Ref. [67]. Left: Current dynamics showing the suppression of Bloch oscillation in the dissipationless regime ($\Lambda = 0$) and the formation of stationary currents in the presence of dissipation ($\Lambda \neq 0$). Right: Dynamics of the effective temperature. In the dissipationless regime the effective temperature quickly diverges, while it reaches a stationary value when a finite coupling with the bath is considered.

3.2.1 Approach to a non-equilibrium steady state

The approach to a stationary state in the case of a constant driving field shows different aspects with respect to the sudden excitations described in the previous sections. Indeed, while in the latter case the excitation results in a finite energy injection inside the system, the effect of a driving field may induce a continuous energy injection which has to be dissipated either by the internal degrees of freedom or by some external environment. The balancing between the energy injection and dissipation leads to the formation of non-equilibrium stationary states with a finite current flowing. As a matter of fact, it has been shown that in several cases this may be prevented if an external dissipative mechanism is not taken into account [67–69].

For instance, this happens in non-interacting systems. In this case the formation of a stationary state is prevented by the periodic structure of the lattice which leads to the formation of the *Bloch oscillations*, namely the periodic motion of the electrons within the Brillouin zone leading to a zero net current. A finite current is then retrieved introducing the scattering with an external fermionic reservoir [68, 69].

On the other hand, the introduction of the electron-electron interaction does not seem to be sufficient condition for the formation of a stationary state. Indeed, it has been shown that this leads to the suppression of Bloch oscillations [67, 70, 71] but no finite current is observed (Fig. 3.2 left). In Ref. [67], where the dynamics of the driven Hubbard model has been addressed by means of non-equilibrium DMFT, this fact has been related to the continuous heating of the system provided by the electric field which in turn determines a fast divergence of the effective temperature (Fig. 3.2 right). In this case, the coupling with local fermionic baths has been shown to be sufficient to drive the formation of a non-

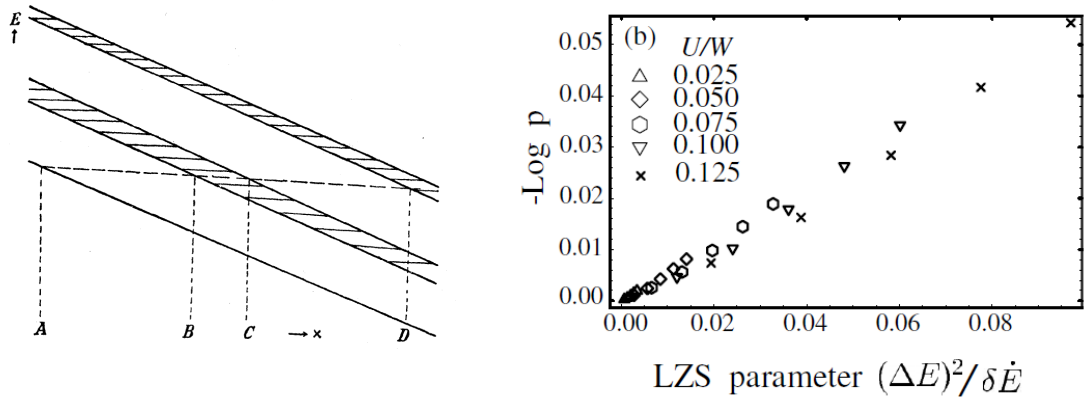

Fig. 3.3: Landau-Zener breakdown in band and Mott insulators. Left: Adapted from Ref. [27]. Sketch of a semiconductor energy bands tilted by the applied electric-field. The shading represents avoided regions through which a carrier from the conduction can tunnel to the valance band with a probability given by Eq. 3.2. Right: Adapted from Ref. [75]. Tunnel probability in a ring threaded by a time dependent magnetic flux as a function of the Landau-Zener parameter. The $p \propto \exp(-(\Delta E)^2/\delta\dot{E})$ behavior supports the tunneling scenario for the breakdown of the Mott insulator.

equilibrium stationary state [67]. Such dissipation mechanism has been further exploited to address the occurrence of a dimensional crossover triggered by strong electric fields [72, 73] and the role of Joule heating [74].

The necessity of a dissipative mechanism even in the presence of the electron-electron interaction, may be related to the fact that the dynamics does not account for all the scattering processes that would lead to the formation of a stationary state in the absence of an external thermostat. For example, this may be the case of a finite size system [75] where only a finite number of degrees of freedom is considered. On the other hand, for a system in the thermodynamic limit this may be due to the approximation used that neglects some scattering process. For instance, in the case of the DMFT approach [67] this may be related to the freezing of spatial fluctuations. However at this stage, due to the absence of a reliable method to properly treat all the scattering processes in the thermodynamic limit, these hypotheses still have be confirmed.

In general, the properties of the non-equilibrium stationary state in a driven correlated system strongly depend on the kind of dissipation mechanisms considered and on the interaction strengths. The resulting I-V characteristics may display relevant features beyond the linear regime, as the appearance of a negative differential conductance [67, 73, 74, 76–78] or contributions of the high-energy incoherent spectral weight [74].

3.2.2 Dielectric breakdown in Mott insulators

Insulating systems represent a special case for the formation of current-carrying states in strong electric fields. In ordinary band insulators this is a very old problem which goes

back to the early 30s with the pioneering work by Zener [27]. In this case, the possibility to induce a finite current was related to the Landau-Zener [79, 80] quantum tunneling of carriers from the valence to the conduction bands tilted by the external field (Fig. 3.3 left). This leads to an exponential activation for the transmission probability across the gap as a function of the applied field [27]

$$\gamma \sim E e^{-E_{th}/E} \tag{3.2}$$

where the threshold field E_{th} depends on the size of the insulating gap. A roughly estimation gives $E_{th} \sim \Delta/\xi$, where Δ is the size of the gap and ξ is the characteristic length scale for an excitation across the gap: $\xi \sim aW/\Delta$, being a the lattice spacing and W the bandwidth. A different mechanism governing the dielectric breakdown phenomenon is based on the avalanche effect driven by an impact ionization. In this scenario the electrons accelerated by the external field further excite electron-hole pairs leading to an exponential proliferation of carriers. Anyway in both avalanche and Zener scenario, the breakdown is driven by the promotion of carriers from conduction to valence band and the threshold field is governed by the size of the insulating gap.

The theoretical understanding of the mechanisms leading to the dielectric breakdown in Mott insulating systems is motivated by the large number of experiments exploring such possibility and the related impact in the search for new electronic devices. Early works tackled the problem considering finite one-dimensional systems [75, 81] where the dynamics can be computed exactly for small enough sizes or by means of time-dependent Density Matrix Renormalization Group in larger systems [82, 83]. An exact solution was carried-out in the case of small rings threaded by a time dependent magnetic flux [75]. Even though the periodic structure of the system does not allow the formation of a genuine steady state, the formation of metallic-like currents for large fields has been detected observing a linear behavior in the short-time current dynamics. This occurrence has been related to the non-adiabatic Landau-Zener tunnel between the low-lying many-body levels induced by the fast variation of the time dependent flux. This fact is supported by the computation of the tunnel probability showing a remarkable agreement with the predictions based on the computation of the the Landau-Zener parameter $(\Delta E)^2/\dot{\delta E}$, being ΔE the gap of the non-crossing levels and $\dot{\delta E}$ the rate of variation of their energy difference (Fig. 3.3 right).

While the tunneling to low-excited states dominating the short-time behavior is understood by the Landau-Zener mechanism, the long-time behavior relevant for the actual breakdown has been analyzed in terms of the Schwinger ground-state decay rate [84] in a larger one-dimensional systems using time-dependent DMRG [81]. Remarkably, the ground state decay-rate can be reproduced by the same functional form in band and Mott insulators, where in the latter case the threshold field is determined by the Landau-Zener prediction substituting the gap between conductance and valence bands with the gap between lower and upper Hubbard bands. A similar analysis led to similar results in the case of a one-dimensional spin polarized insulators [85].

The extension of such analysis to larger dimensional systems is limited by the impossibility of an exact solution in dimensions larger than one. In these cases, the dielectric

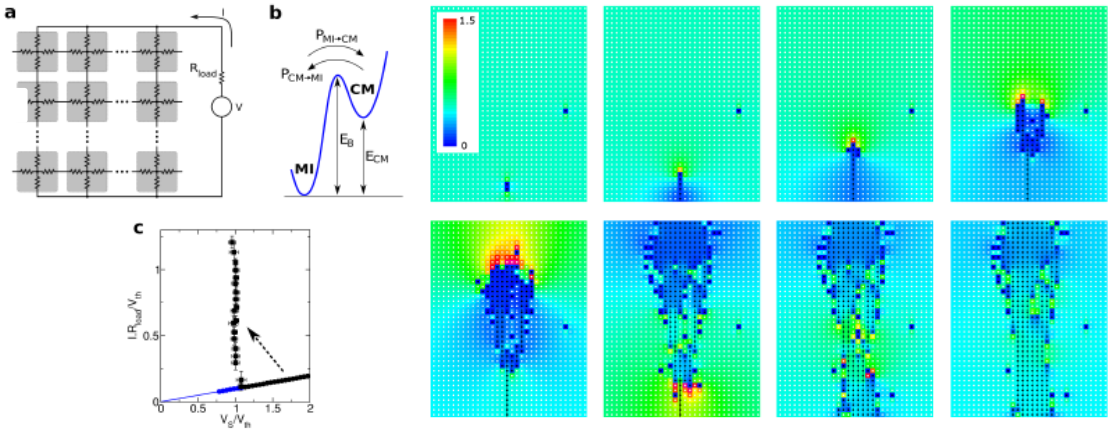

Fig. 3.4: Avalanche formation of conducting channel in a Mott insulator. Adapted from Ref. [26]. Left: Resistor network phenomenological model. Each node of the resistor network can be in either in the Mott insulator (MI) or Paramagnetic metal (PM) state characterized respectively by a high and low resistance. The two states are separated by an energy barrier that can be overcome with finite probability in both directions. The resulting I-V characteristic shows a remarkable agreement with the experimental one (see Fig. 2.4) Right: Snapshots at different times of the resistance map of the network showing the avalanche formation of filamentary conducting paths.

breakdown has been studied within DMFT [86–89] either assuming the existence of a steady-state [86, 87] or following the field induced real-time dynamics [88, 89]. The overall indication of such studies is that of a Landau-Zener breakdown consistent with the exponential activation of the current given by the original Zener formula [27], with a threshold field controlled by the Mott-Hubbard gap.

A different analysis, approaching the dielectric breakdown problem from a different point of view, has been considered in Ref. [26]. In this case the starting point is the observation that the Landau-Zener scenario is not able to describe the experimental outcomes of the resistivity switch experiments in narrow gap Mott insulator (see Sec. 2.2.3), either for what concern the predicted threshold field, which would be of order of few V/nm hence orders of magnitude larger than the experimental observations, and the shape of the I-V characteristic which instead suggests an avalanche-like mechanism [38]. Starting from the first-order character of the Mott transition the authors considered a simple phenomenological model in which the stable insulating solution coexists with a metastable metal in some energy landscape. The system can overcome the energy barrier in both directions with a finite probability and the effect of the electric field is that of modifying such transition probability lowering the barrier height. Therefore, considering the whole system as a resistor network in which each node represents an independent portion which can be either in the insulating or metallic state, a good reproduction of the experimental I-V characteristics has been obtained (Fig. 3.4 left). According to this phenomenological model, the resistive transition coincides with the avalanche formation of filamentary conductive channels originated from the nucleation of a large enough metallic region (Fig. 3.4

right). Therefore the threshold field is not related to the size of the insulating gap, possibly explaining the discrepancy between the Landau-Zener estimation and the experimental results.

3.3 This thesis

The general overview discussed in the previous sections highlights a series of open theoretical issues which are crucial for the investigation of the non-equilibrium physics of correlated materials. Some of these involve fundamental theoretical questions concerning for instance the unitary quantum dynamics in isolated systems of initially excited states, while a more direct comparison with the experimental panorama is related to the problems involving the coupling with external ultrafast excitations or electric fields beyond the linear regime. In the present thesis we look at both of these two directions bringing our attention towards two main questions, namely the problem of dynamical phase transitions driven by the unitary evolution of excited states in isolated systems and the description of electric-field driven correlated systems.

In the first case (Chap. 4), we look at the conditions for which a generic excited system undergoes a dynamical phase transition during the unitary dynamics of an initial excited state. For systems displaying at equilibrium a phase diagram with some symmetry broken phase we relate this possibility to specific features in the many-body energy spectrum which drive the equilibrium phase transition and fix the conditions for the restoration or breaking of symmetry during the unitary evolution of an excited state. In particular, this is related to the hypothesis that the many-body spectrum is divided into symmetry broken and symmetry unbroken states which are separated by a *broken symmetry edge*. We explicit check this hypothesis for the case of quench dynamics in the fully connected Ising model and further exploit this idea to access exotic non-equilibrium superconducting states in the half-filled repulsive Hubbard model.

The rest of the work (Chap. 5 and 6) is devoted to the properties of electric-field driven correlated systems. To begin with, we fully characterize the non-equilibrium properties of a schematic model of correlated material, described within the framework of the single band Hubbard model, attached to external sources (leads) which impose a finite bias across the sample (Chap. 5). Studying the dynamics within the time-dependent Gutzwiller (TDG) approximation we characterize the formation of non-equilibrium stationary states and describe the resulting non-linear current-bias characteristics. In the case of an insulating system this will lead us to discuss the problem of the dielectric breakdown within this framework. Combining the outcome of the numerical simulations and analytical calculations in the stationary regime we conclude that a tunneling mechanism similar to the Landau-Zener one drives the formation of conducting states across the sample.

Motivated by the fact that, as discussed in Sec. 2.2, several systems under different conditions do not follow the expectations of the Zener breakdown mechanism, in Chap. 6 we focus on a possible different mechanisms driving the electric breakdown in Mott insulators. Here we start from the assumption that the single-band Hubbard model rep-

resents a too crude simplification of a correlated materials, and despite capturing the main features of the equilibrium properties may fail in the description of the electronic properties under a large electric field. To this extent we consider a Hubbard model with the inclusion of an extra orbital degree of freedom, mimicking the multi-orbital nature of most correlated materials. Within the framework of Dynamical Mean Field Theory (DMFT) we demonstrate that in this case an electric field smaller than the insulating gap is able to drive a sharp insulator-to-metal transition which stabilizes a gap-collapsed metallic phase that was only metastable at equilibrium. Comparing these results with that of the single band Hubbard model we show that this occurrence represents a novel mechanism for the dielectric breakdown in Mott insulating systems.

Part II

Results

Chapter 4

Quantum quenches and dynamical phase transitions

4.1 Introduction

As discussed in Chap. 2 an interesting class of non-equilibrium experiments focus on the dynamics across phase transitions. In cold atoms systems this can be achieved by changing some of the experimental conditions, as *e.g.* the optical lattice depth, while in real materials ultrafast pump excitations give the possibility to drive the systems into a transient state which may cross some phase transition line.

A simple way to devise this opportunity comes from the fact that the perturbation results in an energy injection which is supposed to effectively heat the system raising its temperature. Thus if the equilibrium phase diagram has a transition between a low-temperature phase and a high-temperature one, such effective temperature increment is supposed to drive the phase transition.

In reality, the problem is not as trivial as the above statement would suggest. Indeed, we have seen that the picture based on the instantaneous increase of the temperature induced by the sudden excitation is not so obvious and, as a matter of fact, several examples show its breakdown. This is even less trivial in the case of a system excited across a phase transition. In fact, across a thermodynamic transition ergodicity is either lost or recovered; hence it is not obvious at all that the unitary time evolution of an initial non-equilibrium quantum state should bring about the same results as, at equilibrium, the adiabatic change of a coupling constant or temperature.

The above questions are related to the problem of thermalization, a fundamental issue of quantum statistical mechanics [90, 91]. In this chapter, without entering in such debate, we address the problem of dynamical phase transitions, highlighting a possible connection with the occurrence in the many-body eigenvalue spectrum of *broken-symmetry edges*, namely special energies that mark the boundaries between symmetry-breaking and symmetry-invariant eigenstates. This provides a justification for understanding why a system undergoes a dynamical phase transition once initially supplied with enough excess

energy. In particular, this circumstance is not related to any thermalization hypothesis.

In the following we shall give an argument for the existence of such energy edge in the many-body spectrum of models undergoing a quantum phase transition to a broken-symmetry phase that survives up to a critical temperature. Thus, we will explicitly show such occurrence in the specific case of the fully-connected Ising model in a transverse field and discuss its role in the prediction of the phase transitions induced by the quench dynamics. Eventually, we will show that a broken-symmetry edge can exist even in models which does not have a thermodynamic phase transition of this kind. In fact, considering the specific case of the fermionic repulsive Hubbard model we will show that the presence of a broken symmetry edge leads to an unexpected quench dynamics characterized by the appearance of non-equilibrium superconducting states which are not accessible by standard thermal pathways.

4.2 Symmetry broken edges

Let us imagine a system described by a Hamiltonian $\mathcal{H}$, which undergoes a quantum phase transition, the zero-temperature endpoint of a whole second-order critical line that separates a low-temperature broken-symmetry phase from a high-temperature symmetric one, see Fig. 4.1 where g is the coupling constant that drives the phase transition. For the sake of simplicity, and also because it will be relevant later, let us assume that the broken symmetry is a discrete Z_2 - all arguments below do not depend on this specific choice - with order parameter

$$\langle \sigma \rangle = \frac{1}{V} \sum_i \langle \sigma_i \rangle \in [-1, 1], \tag{4.1}$$

which is not a conserved quantity, i.e. $\Big[\sigma, \mathcal{H}\Big] \neq 0$, and where $V \to \infty$ is the volume and i labels lattice sites. Below the quantum critical point $g < g_c$, Fig. 4.1, the ground state is doubly degenerate and not Z_2 invariant. If $\mid \Psi_\pm \rangle$ are the two ground states, they can be chosen such that

$$\langle \Psi_\pm \mid \sigma \mid \Psi_\pm \rangle = \pm m, \qquad \text{with } m > 0.$$

On the contrary, for $g > g_c$, the ground state is unique and symmetric, i.e. the average of σ vanishes. Since the symmetry breaking survives at finite temperature, see Fig. 4.1, one must conclude that, besides the ground state, a whole macroscopic set of low energy states is Z_2 not-invariant. The ergodicity breakdown in a symmetry broken phase specifically implies that these states, in the example we are dealing with, are grouped into two subspaces that are mutually orthogonal in the thermodynamic limit, one that can be chosen to include all eigenstates with $\langle \sigma \rangle > 0$, the other those with $\langle \sigma \rangle < 0$. Since the symmetry is recovered above a critical temperature, then there should exist a high energy subspace that includes symmetry invariant eigenstates. We argue that there should be a special energy in the spectrum, a *broken-symmetry edge* E_*, such that all eigenstates with $E < E_*$ break the symmetry, while all eigenstates above E_* are symmetric.

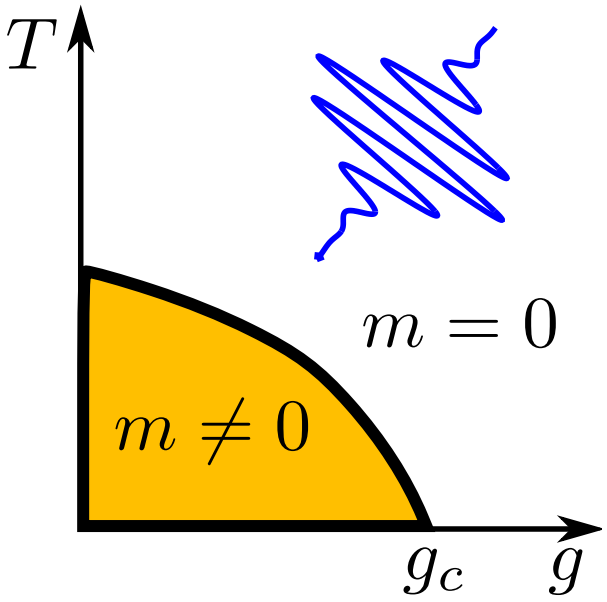

Fig. 4.1: Schematic picture of the dynamics across a phase transition. Schematic picture of a model showing a low temperature broken symmetry phase characterized by some order parameter $m \neq 0$ and a high temperature symmetric phase for which $m = 0$. The two phases are separated by a second order line which ends in a quantum critical point for $g = g_c$. We sketched an ultrafast excitation possibly driving the dynamical phase transition.

In the case where the Hamiltonian has additional symmetries besides Z_2, hence conserved quantities apart from energy, we claim that, within each subspace invariant under these further symmetries, there must exist an edge above which symmetry is restored, even though its value may differ from one subspace to another as is the case in the model discussed in the next section.

Let us for instance focus on any of these subspaces. The Z_2 symmetry implies that all eigenstates are even or odd under Z_2. The order parameter σ is odd, hence its average value is strictly zero on any eigenstate, either odd or even. Nevertheless, we can formally define an order parameter $m(\Psi_E)$ of a given eigenstate $\mid \Psi_E\rangle$ through the positive square root of

$$m\big(\Psi_E\big) = \sqrt{\lim_{|i-j|\to\infty} |\langle \Psi_E \mid \sigma_i \sigma_j \mid \Psi_E \rangle|}. \tag{4.2}$$

We denote by

$$\rho_{SB}(E) = \mathrm{e}^{V\, S_{SB}(\epsilon)}, \tag{4.3}$$

the density of symmetry-breaking eigenstates, namely those with $m(\Psi_E) > m_0$, where m_0 is a cut-off value that vanishes sufficiently fast as $V \to \infty$, being $\epsilon = E/V$ and $S_{SB}(\epsilon)$ their energy and entropy per unit volume. Seemingly, we define

$$\rho_{SI}(E) = \mathrm{e}^{V\, S_{SI}(\epsilon)}, \tag{4.4}$$

the density of the symmetry-invariant eigenstates, $m(\Psi_E) \leq m_0$, with $S_{SI}(\epsilon)$ their entropy. We claim that there exists an energy $E_* = V\epsilon_*$ that marks the microcanonical continuous phase transition in that specific invariant subspace, such that

$$\lim_{V\to\infty} S_{SI}(\epsilon) = 0, \qquad \text{for } \epsilon < \epsilon_*, \tag{4.5}$$

$$\lim_{V\to\infty} S_{SB}(\epsilon) = 0, \qquad \text{for } \epsilon > \epsilon_*. \tag{4.6}$$

We do not have a rigorous proof of the above statement, but just a plausible argument. Let us suppose to define the average $m(E) > m_0$ of the order parameter over the symmetry-breaking eigenstates through

$$m(\epsilon) = \frac{1}{\rho_{SB}(E)} \sum_{\Psi_{E'}} m\big(\Psi_{E'}\big)\, \delta\big(E' - E\big). \tag{4.7}$$

The actual microcanonical average is thus

$$\overline{m}(\epsilon) = \frac{\rho_{SB}(E)}{\rho_{SB}(E) + \rho_{SI}(E)}\, m(\epsilon). \tag{4.8}$$

In the thermodynamic limit $V \to \infty$, hence $m_0 \to 0$, the continuous phase transition would imply the existence of an energy ϵ_* such that, for $\epsilon \lesssim \epsilon_*$, $\overline{m}(\epsilon) \sim (\epsilon_* - \epsilon)^\beta$, while $\overline{m}(\epsilon > \epsilon_*) = 0$. Since the entropy ratio on the r.h.s. of Eq. (4.8) is either 1 or 0 in the thermodynamic limit, we conclude that the critical behavior comes from $m(\epsilon \lesssim \epsilon_*) \sim (\epsilon_* - \epsilon)^\beta$, which, by continuity, implies $m(\epsilon > \epsilon_*) = 0$, namely that there are no symmetry-breaking eigenstates with finite entropy density above ϵ_*, hence Eq. (4.6). This further suggests that symmetry-breaking and symmetry-invariant eigenstates exchange their role across the transition, which makes also Eq. (4.5) plausible.

We may also try to generalize the above picture to the most common situation of a first order phase transition. In this case we expect two different edges, $\epsilon_1 < \epsilon_*$. Below ϵ_1 the entropy density of symmetry-invariant states $S_{SI}(\epsilon)$ vanishes in the thermodynamic limit, while above ϵ_*, the actual edge for symmetry restoration, it is $S_{SB}(\epsilon)$ that goes to zero.

If we accept the existence of such an energy threshold, then we are also able to justify why a material, whose equilibrium phase diagram is like that of Fig. 4.1, may undergo a dynamical phase transition once supplied initially with enough excess energy so as to push it above E_*. We mention once more that the above arguments are not at all a real proof. However, they can be explicitly proven in mean-field like models, like the fully connected Ising model that we discuss in the section 4.3. There, we explicitly demonstrate that the dynamical transition occurs because above a threshold energy there are simply no more broken-symmetry eigenstates in the spectrum. We believe this is important because it may happen that such an energy threshold, hence such a dynamical transition, exists also in models whose phase diagram is different from that of Fig. 4.1, as we are going to discuss in section 4.4.

4.3 Fully connected Ising model in transverse field

Broken symmetry edge

We consider the Hamiltonian of an Ising model in a transverse field

$$\begin{aligned} \mathcal{H} &= -\sum_{i,j} J_{ij}\, \sigma_i^z \sigma_j^z - h \sum_i \sigma_i^x \\ &= -\frac{1}{N} \sum_{\mathbf{q}} J_{\mathbf{q}}\, \sigma_{\mathbf{q}}^z \sigma_{-\mathbf{q}}^z - h\, \sigma_{\mathbf{0}}^x, \end{aligned} \tag{4.9}$$

where N is the number of sites,

$$\sigma_{\mathbf{q}}^a = \sum_i \mathrm{e}^{-i\mathbf{q}\cdot\mathbf{r}_i}\, \sigma_i^a,$$

is the Fourier transform of the spin operators, and $J_{\mathbf{q}}$ the Fourier transform of the exchange. In the (mean-field) fully-connected limit, $J_{\mathbf{q}} = J\,\delta_{\mathbf{q0}}$, the model (4.9) simplifies into

$$\mathcal{H} = -\frac{1}{N}\, \sigma_{\mathbf{0}}^z \sigma_{\mathbf{0}}^z - h\, \sigma_{\mathbf{0}}^x = -\frac{4}{N} S^z S^z - 2h\, S^x, \tag{4.10}$$

having set $J = 1$ and defined the total spin $\mathbf{S} = \boldsymbol{\sigma}_{\mathbf{0}}/2$. It turns out that the Hamiltonian Eq. (4.10) can be solved exactly. We shall closely follow the work by Bapst and Semerjian, [92] whose approach fits well our purposes. For reader's convenience we will repeat part of Bapst and Semerjian's calculations. We start by observing that the Hamiltonian (4.10) commutes with the total spin operator $\mathbf{S}\cdot\mathbf{S}$, with eigenvalue $S(S+1)$, so that one can diagonalize $\mathcal{H}$ within each $S \in [0, N/2]$ sector, whose eigenvalues are $g(S)$ times degenerate, where

$$g(S) = \binom{N}{\frac{N}{2}+S} - \binom{N}{\frac{N}{2}+S+1}, \tag{4.11}$$

is the number of ways to couple N spin-1/2 to obtain total spin S. We define

$$S = N\Big(\frac{1}{2} - k\Big), \tag{4.12}$$

where k, for large N, becomes a continuous variable $k \in [0, 1/2]$. For a given S, a generic eigenfunction can be written as

$$\mid \Phi_E\rangle = \sum_{M=-S}^{S} \Phi_E(M) \mid M\rangle, \tag{4.13}$$

where $\mid M\rangle$ is eigenstate of S^z with eigenvalue $M \in [-S, S]$. One readily find the eigenvalue equation [92]

$$\begin{aligned} E\,\Phi_E(M) &= -\frac{4}{N}\,M^2\,\Phi_E(M) \\ &\quad -h\Big[\sqrt{S(S+1)-M(M-1)}\;\Phi_E(M-1) \\ &\quad +\sqrt{S(S+1)-M(M+1)}\;\Phi_E(M+1)\Big]. \end{aligned} \tag{4.14}$$

We now assume N large keeping k constant. We also define

$$m = \frac{2M}{N} \in [-1+2k, 1-2k],$$

so that, at leading order in N, after setting $E = N\epsilon$ and

$$\Phi_E(M) = \Phi_\epsilon(m),$$

the Eq. (4.14) reads

$$\begin{aligned} \epsilon\,\Phi_\epsilon(m) &= -m^2\,\Phi_\epsilon(m) - \frac{h}{2}\sqrt{(1-2k)^2-m^2} \\ &\quad \left[\Phi_\epsilon\left(m-\frac{2}{N}\right)+\Phi_\epsilon\left(m+\frac{2}{N}\right)\right]. \end{aligned} \tag{4.15}$$

Following Ref. [92], we set

$$\Phi_\epsilon(m) \propto \exp\big[-N\,\phi_\epsilon(m)\big], \tag{4.16}$$

where the proportionality constant is the normalization, so that

$$\begin{aligned} \Phi_\epsilon\left(m\pm\frac{2}{N}\right) &\propto \exp\left[-N\,\phi_\epsilon\left(m\pm\frac{2}{N}\right)\right] \\ &\simeq \Phi_\epsilon(m)\,\mathrm{e}^{\mp 2\,\phi'_\epsilon(m)}, \end{aligned}$$

Upon substituting the above expression into (4.15), the following equation follows

$$\phi'_\epsilon(m) = \frac{1}{2}\,\mathrm{arg\,cosh}\left(-\frac{\epsilon+m^2}{h\sqrt{(1-2k)^2-m^2}}\right). \tag{4.17}$$

For large N, in order for the wave function (4.16) to be normalizable, we must impose that: (*i*) the $\Re\mathrm{e}\,\phi'_\epsilon(m) \geq 0$; (*ii*) the $\Re\mathrm{e}\,\phi'_\epsilon(m)$ must have zeros, which, because of (*i*), are also minima. As showed in Ref. [92], these two conditions imply that the allowed values of the energy are

$$\min\Big(f_-(m)\Big) \leq \epsilon \leq \mathrm{Max}\Big(f_+(m)\Big),, \tag{4.18}$$

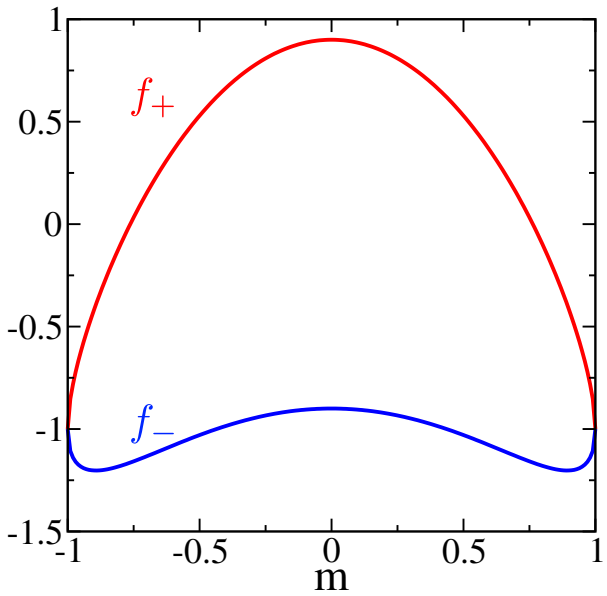

Fig. 4.2: Allowed eigenvalues for the fully connected Ising model. The two function $f_+(m)$ and $f_-(m)$ for $k = 0$ and $h = 0.9$. The allowed values of the eigenvalues are those between the minimum of f_- and the maximum of f_+.

where

$$f_+(m) = -m^2 + h\sqrt{(1-2k)^2 - m^2}, \tag{4.19}$$
$$f_-(m) = -m^2 - h\sqrt{(1-2k)^2 - m^2}. \tag{4.20}$$

At fixed k, the lowest allowed energy is thus

$$\epsilon_{\min}(k) = \min\left(f_-(m)\right) = -(1-2k)^2 - \frac{h^2}{4}, \tag{4.21}$$

and occurs at

$$m^2(k) = (1-2k)^2 - \frac{h^2}{4}, \tag{4.22}$$

if $h \leq h(k) = 2(1-2k)$, otherwise the minimum energy occurs at $m = 0$,

$$\epsilon_{\min}(k) = f_-(0) = -h\,(1-2k). \tag{4.23}$$

It follows that the actual ground state is always in the $k = 0$ subspace and has energy

$$\epsilon_0 = \begin{cases} -1 - \frac{h^2}{4} & \text{if } h \leq h(0) = 2, \\ -h & \text{if } h > h(0). \end{cases} \tag{4.24}$$

In Fig. 4.2 we plot the two functions $f_+(m)$ and $f_-(m)$ for $k = 0$ and $h = 0.9 < h(0)$. As shown by Bapst and Semerjian, [92] whenever $f_-(m)$ has a double minimum as in Fig. 4.2, any eigenstate with energy below $\epsilon < \epsilon_* = f_-(m = 0)$ is doubly degenerate in

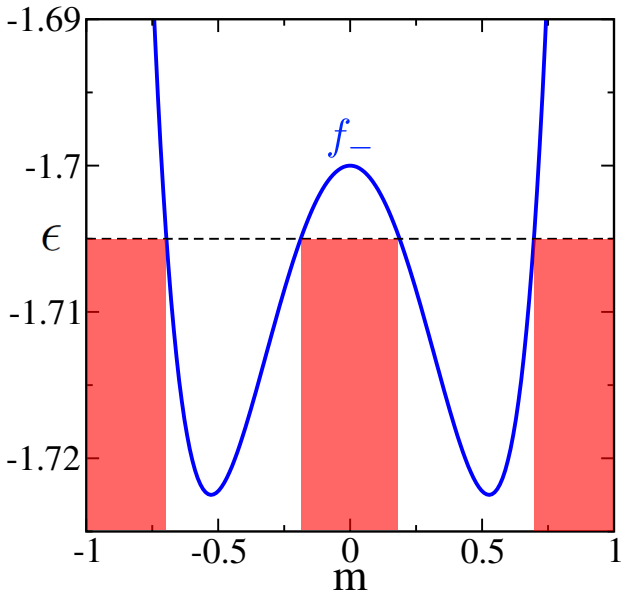

Fig. 4.3: Exponential vanishing of the wave-function tails. For a given energy $\epsilon < \epsilon_*$, we draw the region where the wave function vanishes exponentially as $N \to \infty$.

the thermodynamic limit $N \to \infty$, being localized either at positive or at negative m, thus not invariant under Z_2. On the contrary, the eigenvalues for $\epsilon \geq \epsilon_*$ are not degenerate and are Z_2 symmetric. More specifically, any eigenfunction $\Phi_\epsilon(m)$ has evanescent tails that vanish exponentially with N in the regions where $f_-(m) > \epsilon$ and $f_+(m) < \epsilon$. In Fig. 4.3 we show in the case $\epsilon < \epsilon_*$ the regions of evanescent waves. In this case, one can construct two eigenfunctions, each localized in a well, see the figure, whose mutual overlap vanishes exponentially for $N \to \infty$. This result also implies that the ground state, which lies in the $k = 0$ subspace, spontaneously breaks Z_2 when $h < h(0)$, hence $h(0) = 2 = h_c$ is the critical transverse field at which the quantum phase transition takes place. Such a degenerate ground state is actually a wave packet centered either at $m = +\sqrt{1 - h^2/4}$ or at $-\sqrt{1 - h^2/4}$, see Eq. (4.22).

More generally, it follows that for any given k and $h < h(k) = 2(1-2k)$ there is indeed a "broken-symmetry edge"

$$\epsilon_*(k) = -h\,(1 - 2k), \tag{4.25}$$

that separates symmetry breaking eigenstates at $\epsilon < \epsilon_*$ from symmetric eigenstates at higher energies. In particular, in the lowest energy subspace with $k = 0$, the edge is $\epsilon_*(0) = -h$. Therefore, although in the simple mean-field like model Eq. (4.10), one can indeed prove the existence of energy edges that separate symmetry invariant from symmetry breaking eigenstates. We also note that subspaces corresponding to different k have different $\epsilon_*(k)$.

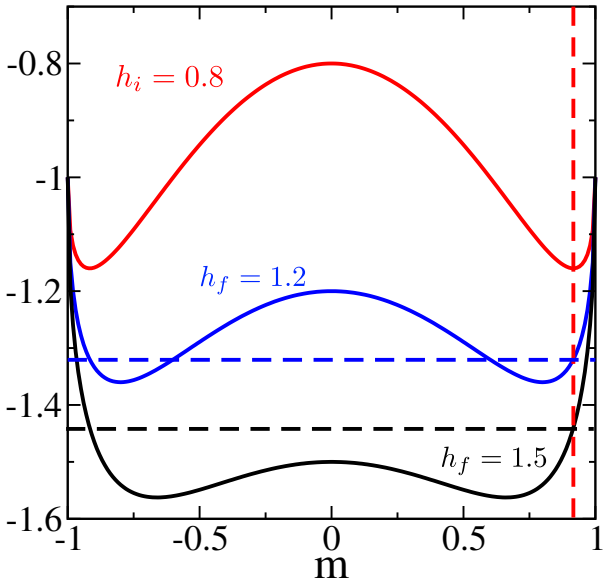

Fig. 4.4: Pictorial view of the quench dynamics for the fully connected Ising model. The upper curve (red) corresponds to the Hamiltonian for $t < 0$ characterized by $h_i = 0.8$. We assume that for negative time the wave function is the ground state for $m > 0$, which corresponds to the minimum of the curve at positive m_i, dashed vertical line. The intermediate curve (blue) corresponds to $f_-(m)$ for $h_f = 1.2$, while the lowest curve (black) to $h_f = 1.5$. The intercepts $\epsilon = f_-(m_i)$ define the lower bound of allowed energies.

Quench dynamics

The quench dynamics we examine corresponds to propagating the ground state at $h = h_i$ with a different transverse field $h = h_f$. In the specific case of a fully-connected model, this problem has been addressed by Refs. [57] and [58]. In particular, it has been found [58] that for $h_i < h_c$, i.e. starting from the broken-symmetry phase, a dynamical transition occurs at $h_f = h_* = (h_c + h_i)/2$. For $h_f \geq h_*$, the symmetry is dynamically restored, while, below, it remains broken as in the initial state.

If, instead of a sudden increase from $h_i < h_c$ to h_f, one considers a linear ramp

$$h(t) = \begin{cases} h_i + (h_f - h_i)\,\dfrac{t}{\tau} & \text{for } t \in [0, \tau], \\ h_f & \text{for } t > \tau, \end{cases}$$

then the critical h_* increases and tends asymptotically to the equilibrium critical value $h_c(0)$ for $\tau \to \infty$ [93], as expected for an adiabatically slow switching rate. This result demonstrates that the dynamical transition is very much the same as the equilibrium one, and it occurs for lower fields h only because of anti-adiabatic effects, which is physically plausible.

We now show how such a dynamical transition is related to the symmetry-restoration edge previously defined. We therefore imagine to start from the ground state at an initial $h_i < h_c$, which occurs in the subspace of $k = 0$, i.e. maximum total spin $S = N/2$, and let it evolve with the Hamiltonian at a different $h_f > h_i$. We note that, since S is

conserved, the time-evolved wave function will stay in the subspace $k = 0$. The ground state at h_i is degenerate, and we choose the state with a positive average of m, which is a wave-packet narrowly centered around $m_i = \sqrt{1-(h_i/2)^2}$. For very large N, when the contributions from the evanescent waves in the regions where $\Re\mathrm{e}\phi'_\epsilon(m) > 0$ can be safely neglected, the initial wave function decomposes in $k = 0$ eigenstates of the final Hamiltonian with eigenvalues ϵ such that $f_-(m_i) \leq \epsilon \leq f_+(m_i)$. In Fig. 4.4 we show graphically the condition $\epsilon \geq f_-(m_i)$ for $h_i = 0.6$ and two values of $h_f = 1.2, 1.5$. We note that the minimum value of the allowed energy for $h_f = 1.2$ belongs to the subspace of symmetry broken states, while for $h_f = 1.5$ it belongs to the subspace of symmetric states. It follows that, while for $h_f = 1.2$ the long time average of m will stay finite, for $h_f = 1.5$ it will vanish instead. The critical $h_f = h_*$ is such that $f_-(m_i) = f_-(0) = -h_*$, namely $h_* = 1 + h_i/2 = (h_c + h_i)/2$, which is indeed the result of Ref. [58]. Therefore, the dynamical restoration of the symmetry is intimately connected to the existence of an energy threshold. When the initial wave function decomposes into eigenstates of the final Hamiltonian that all have energies higher than that threshold, then the long time average of the order parameter vanishes although being initially finite.

We note that the dynamical transition in this particular example is related to the equilibrium quantum phase transition, but it is actually unrelated to the transition at finite temperature [92]. In fact, at a given value of the transverse field $h < h_c$, all eigenstates within the subspaces with $k \geq h_c - h$ are symmetric, while those with smaller k have still low-energy symmetry-breaking eigenstates. Since the degeneracy $g(S)$, see Eq. (4.11), increases exponentially in N upon lowering S, hence raising k, the entropic contribution of the symmetric subspaces at large k will dominate the free energy and eventually drive the finite temperature phase transition. On the contrary, the quench-dynamics is constrained within the subspace at $k = 0$, hence it remains unaware that in other subspaces the eigenstates at the same energy are symmetric.

This observation is important and makes one wonders how the above result can survive beyond the fully-connected limit. Indeed, as soon as the Fourier transform of the exchange $J_{\mathbf{q}}$, see Eq. (4.9), acquires finite components at $\mathbf{q} \neq \mathbf{0}$, states with different total spin, hence different k, start to be coupled one to each other – the total spin ceases to be a good quantum number, the only remaining one being the total momentum. Therefore, symmetry-breaking eigenstates at low k get coupled to symmetric eigenstates at large k. In this more general situation, there are no rigorous results apart from the pathological case of one-dimension, where the energy above which symmetry is restored actually coincides with the ground state energy. However, we mention that a recent attempt to include small $\mathbf{q} \neq \mathbf{0}$ fluctuations on top of the results above, i.e. treating

$$-\frac{1}{N}\sum_{\mathbf{q}\neq\mathbf{0}} J_{\mathbf{q}}\,\sigma^z_{\mathbf{q}}\sigma^z_{-\mathbf{q}} \tag{4.26}$$

as a small perturbation of the *bare* Hamiltonian

$$\mathcal{H}_0 = -\frac{J_{\mathbf{0}}}{N}\,\sigma^z_{\mathbf{0}}\sigma^z_{\mathbf{0}} - h\,\sigma^x_{\mathbf{0}},$$

suggests that the dynamical transition in the quench does survive [93], which we take as an indirect evidence that the energy edge does, too. We suspect the reason being that, once symmetry-breaking and symmetry-invariant eigenstates of same energy get coupled by (4.26), the new eigenstates, being linear combinations of the former ones, will all be symmetry-breaking. As a result, the broken-symmetry edge will end to coincide approximately with $\epsilon_*(k = 0)$, *i.e.* with the maximum value among all the formerly independent subspaces.

4.4 Non-equilibrium superconducting states in the repulsive Hubbard model

Broken Symmetry Edge

In Sec. 4.2 we inferred the existence of a threshold energy by the existence of a finite temperature phase transition that ends at $T = 0$ into a quantum critical point. However, we found in the previous section an energy edge above which symmetry is restored that is actually unrelated to the finite temperature phase transition, while it is only linked to the quantum phase transition. This suggests that such an edge could exists in a broader class of situations. In some simple cases, one can actually prove its existence without much effort. Let us consider for instance the fermionic Hubbard model in three dimensions, with Hamiltonian

$$\mathcal{H} = -\sum_{i,j,\sigma} t_{ij} \left(c^\dagger_{i\sigma} c_{j\sigma} + H.c. \right) + \frac{U}{2} \sum_i (n_i - 1)^2, \tag{4.27}$$

where $U > 0$ is the on-site repulsion. In the parameter space where magnetism can be discarded, the low energy part of the spectrum is that of a normal metal, hence all eigenstates are expected to be invariant under the symmetries of the Hamiltonian $\mathcal{H}$, namely translations, spin-rotations and gauge transformations. We observe that the high-energy sector of the many-body spectrum obviously corresponds to the low energy spectrum of the Hamiltonian $-\mathcal{H}$. The latter is characterized by an opposite band dispersion, which determines a rearrangement of the occupied states in momentum space, but, more importantly, by an attractive rather than repulsive interaction. As a result of the Cooper instability, the ground state of this Hamiltonian is characterized by a finite superconducting order parameter which survives up to a critical temperature for each value of the attractive interaction. Therefore, the low-energy spectrum of $-\mathcal{H}$ must comprise eigenstates $\mid \Psi \rangle$ with superconducting off-diagonal long range order,

$$\lim_{|i-j| \to \infty} \langle \Psi \mid d^\dagger_{i\uparrow} d^\dagger_{i\downarrow} \, d_{j\downarrow} d_{j\uparrow} \mid \Psi \rangle = \mid \Delta \mid^2 > 0, \tag{4.28}$$

which are not invariant under gauge transformations. Since these are identically the high-energy eigenstates of the original repulsive Hamiltonian Eq. (4.27), it follows that the upper part of its many-body spectrum contains eigenstates with off-diagonal long range

order. Thus, there must exist a special energy threshold above which superconducting eigenstates appear in the spectrum.

Suppose to prepare a wave function that initially has $|\Delta(t=0)|^2 > 0$, see Eq. (4.28), and let it evolve with the Hamiltonian $\mathcal{H}$, Eq. (4.27). If its energy is high enough, so that its overlap with the upper part of the spectrum is finite, then $|\Delta(t\to\infty)|^2 > 0$, otherwise $|\Delta(t\to\infty)|^2 \to 0$, signaling once again a dynamical transition that, unlike the previous example of section 4.3, is now accompanied by the emergence rather than disappearance of long-range order. This surprising result was already conjectured by Rosch *et al.* in Ref. [63] as a possible metastable state attained by initially preparing a high energy wave function with all sites either doubly occupied or empty at very large U. Here we showed that that such a superfluid behavior is robust and it is merely a consequence of the high energy spectrum of $\mathcal{H}$, which contains genuinely superconducting eigenstates. We finally observe that these states have negative temperature, hence are invisible in thermodynamics unless one could effectively invert the thermal population [94, 95].

Quench Dynamics

While the existence of a high-energy subspace of superfluid eigenstates of the Hamiltonian (4.27) is evident by the above discussion, it is worth showing explicitly its consequences in the out-of-equilibrium dynamics. To this end, we span the high energy part of the spectrum preparing the system in an initial state $|\Psi(t=0)\rangle$ with energy $E = \langle\Psi|\mathcal{H}|\Psi\rangle > E_{eq}$, where E_{eq} is the ground state energy, and let it evolve in time with Hamiltonian (4.27). In particular, we consider an initial wave function with a finite order parameter

$$\Delta_0 \equiv \Delta(t=0) = \langle\Psi(0)\mid c^\dagger_{i\uparrow}c^\dagger_{i\downarrow} + c_{i\downarrow}c_{i\uparrow}\mid\Psi(0)\rangle, \tag{4.29}$$

choosing $|\Psi(0)\rangle = |\Psi_\lambda\rangle$ the ground state of the BCS Hamiltonian

$$\mathcal{H}_{\rm BCS} = +\sum_{i,j,\sigma} t_{ij}\left(c^\dagger_{i\sigma}c_{j\sigma} + H.c.\right) + \sum_i \left(\lambda\, c^\dagger_{i\uparrow}c^\dagger_{i\downarrow} + H.c.\right), \tag{4.30}$$

where the sign of the hopping is changed with respect to (4.27), and λ is a control parameter that allows to vary the energy of the system by tuning the value of Δ_0 (see inset of figure 4.6). It is important to point out that the sign of the hopping has been changed in order to obtain a wave function with energy greater with respect to the case with original sign and has no connection with the previous discussion on the inversion of the spectrum of the Hamiltonian (4.27).

Since the repulsive Hubbard model proved insoluble so far, we simulate the unitary quantum dynamics using the time-dependent Gutzwiller (TDG) approximation [49, 96]. In brief, the time-evolved wave function is approximated by the form

$$|\Psi(t)\rangle \simeq \prod_i \mathcal{P}_i(t)\,|\Psi_0(t)\rangle, \tag{4.31}$$

where $\mathcal{P}_i(t)$ is a non-hermitian time-dependent variational operator that acts on the Hilbert space at site i, and $|\Psi_0(t)\rangle$ an uncorrelated wave function. Both variational operators $\mathcal{P}_i(t)$ and uncorrelated wave function $|\Psi_0(t)\rangle$ are determined through the saddle

point of the action

$$\mathcal{S} = \int dt \, \langle \Psi(t) | i \frac{\partial}{\partial t} - \mathcal{H} | \Psi(t) \rangle. \tag{4.32}$$

The latter is computed within the Gutzwiller approximation. Without entering into the details of the method which we recall in Appendix A, here we highlight the main steps that lead to the dynamical equations which completely determine the dynamics within the TDG approximation. For a detailed review see Ref. [97].

The action Eq. 4.32 on the wave function 4.31 can be analytically computed assuming the limit of infinite coordination number and imposing the following constraints on the variational ansatz

$$\langle \Psi_0(t) | \mathcal{P}_i^\dagger(t) \mathcal{P}_i(t) | \Psi_0(t) \rangle = 1 \tag{4.33}$$

$$\langle \Psi_0(t) | \mathcal{P}_i^\dagger(t) \mathcal{P}_i(t) \mathcal{C}_i | \Psi_0(t) \rangle = \langle \Psi_0(t) | \mathcal{C}_i | \Psi_0(t) \rangle, \tag{4.34}$$

being $\mathcal{C}_i$ the local single particle matrix. Therefore, the representation of the Gutzwiller projectors in terms of site dependent matrices $\hat{\Phi}_i(t)$ in the so-called mixed basis representation [98] (see App. A.1) leads, upon the enforcement of the saddle-point condition, to the two coupled Schrödinger equations

$$i \frac{\partial |\Psi_0(t)\rangle}{\partial t} = \mathcal{H}_*[\hat{\Phi}(t)] |\Psi_0(t)\rangle \tag{4.35}$$

$$i \frac{\partial \hat{\Phi}(t)}{\partial t} = \frac{U}{2} (\hat{n}_i - 1)^2 \hat{\Phi}(t) + \langle \Psi_0(t) | \frac{\partial \mathcal{H}_*[\hat{\Phi}(t)]}{\partial \hat{\Phi}^\dagger(t)} | \Psi_0(t) \rangle. \tag{4.36}$$

The Hamiltonian $\mathcal{H}_*$ in equation (4.35) is an effective hopping Hamiltonian which is obtained substituting

$$c_{i,\sigma}^\dagger \rightarrow R[\hat{\Phi}(t)] d_{i\sigma}^\dagger + Q^*[\hat{\Phi}(t)] d_{i,\sigma} \tag{4.37}$$

$$c_{i,\sigma} \rightarrow R^*[\hat{\Phi}(t)] d_{i\sigma} + Q[\hat{\Phi}(t)] d_{i,\sigma}^\dagger \tag{4.38}$$

in the bare hopping Hamiltonian

$$H_0 = -t \sum_{i,j\sigma} c_{i\sigma}^\dagger c_{j\sigma} + h.c. \tag{4.39}$$

The hopping renormalization factors $R[\hat{\Phi}(t)]$ and $Q[\hat{\Phi}(t)]$ depend in time through the matrix $\hat{\Phi}(t)$ and they are obtained via standard calculation within Gutzwiller approximation (see App. A.2). Defining $\tau(t) \equiv |R(t)|^2 - |Q(t)|^2$ and $\Delta(t) \equiv 2Q(t)R(t)$ (the dependency on the matrix $\hat{\Phi}$ is understood) the effective hopping Hamiltonian becomes a BCS like Hamiltonian with time dependent couplings

$$\mathcal{H}_*[\hat{\Phi}(t)] = \sum_{\mathbf{k}} \psi_{\mathbf{k}}^\dagger \begin{pmatrix} \tau(t)\epsilon_{\mathbf{k}} & \Delta(t)\epsilon_{\mathbf{k}} \\ \Delta^*(t)\epsilon_{\mathbf{k}} & -\tau(t)\epsilon_{\mathbf{k}} \end{pmatrix} \psi_{\mathbf{k}} \tag{4.40}$$

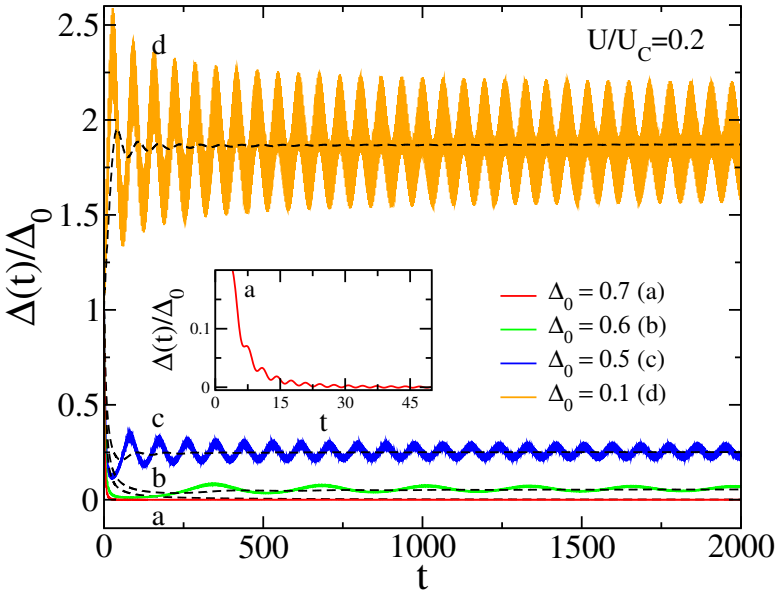

Fig. 4.5: Non-equilibrium superconducting states in the repulsive Hubbard model. Time evolution of the superconducting order parameter $\Delta(t)$ for a repulsive $U = 0.2U_c$, where U_c is the critical repulsion at the Mott transition, and four different initial values Δ_0, the curves a, b, c and d. We also show in the inset the early time relaxation of $\Delta(t)$ in case a. Time is in units of the inverse of half the bandwidth. We observe that the curves b, c and d maintain a finite order parameter, unlike the curve a, although it corresponds to the largest initial $\Delta_0 = 0.7$. We also note that in the case d with the lowest $\Delta_0 = 0.1$, the order parameter actually grows in time.

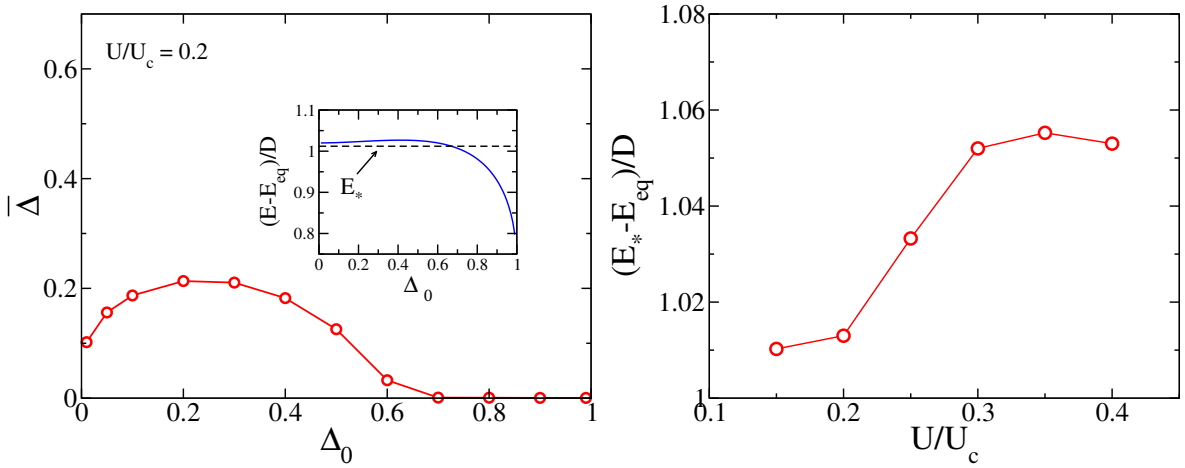

Fig. 4.6: Non-equilibrium order parameter and broken symmetry edges. (Left) Long-time average of the order parameter, $\bar{\Delta}$, as function of its initial value, Δ_0. In the inset we show the energy, in units of half-bandwidth, with respect to the ground state one obtained within the Gutzwiller approximation, as function of Δ_0, as well as the broken-symmetry edge, the dashed line, corresponding to $U = 0.2U_c$. (Right) Broken-symmetry edge measured with respect to the ground state energy for different values of U

where $\psi^\dagger_{\mathbf{k}} \equiv \left(d^\dagger_{\mathbf{k},\uparrow}, d_{-\mathbf{k},\downarrow}\right)$.

Starting from the initial conditions

$$\begin{aligned} |\Psi_0(t=0)\rangle &= |\Psi_\lambda\rangle \\ \mathcal{P}_i(t=0) &= 1. \end{aligned} \tag{4.41}$$

we numerically integrate the coupled Schrödinger equations (4.35-4.36) obtaining the time-evolved wave function within the Gutzwiller approximation. As discussed in App. A these two coupled Schrödinger equations are commonly interpreted as the dynamical equations for coherent quasi-particles, in this specific case the Landau-Bogoliubov quasi-particles, and for local degrees of freedom associated to the Hubbard sidebands. Although the two dynamics are coupled only in a mean-field like fashion, this represents the great advantage of the Gutzwiller approximation with respect to standard time dependent Hartree-Fock approximation.

For convenience, all calculations are done at half-filling, where they are much simpler, focusing on the paramagnetic sector, i.e. discarding magnetism, and assuming a flat density of states with half-bandwidth D which we take as the energy unit. However, in order to avoid spurious interference effects from the Mott transition that occurs above a critical U_c, we concentrate on values of U safely below U_c, in fact below the dynamical analogue of the Mott transition that is found when $U \gtrsim U_c/2$ [48, 49] .

In fig. 4.5 we plot the time evolution of the order parameter for $U = 0.2U_c$ and different initial values of Δ_0, see Eq. (4.29), as well as different energies, see inset of Fig. 4.6, where we also show the time-averaged values of $\Delta(t)$ with respect to their initial values. We observe that at the lower energies, which actually correspond to the larger Δ_0, the order parameter, initially finite, relaxes rapidly to zero. On the contrary, above a threshold energy, $\Delta(t)$ stays finite and even grows with respect to its initial value, see Fig. 4.6. This surprising result indicates that the final order parameter has no relation with the inital one. Namely, it is only determined by the energy of the initial excited state which select the superconducting eigenstates above the threshold energy in which the initial state is decomposed. If we identify that threshold energy as our broken-symmetry edge, its dependence upon U is shown in Fig. 4.6.

4.5 Conclusions

The above results show that a dynamical phase transition can be directly related to the existence of an energy threshold in the many-body spectrum which separates broken symmetry states from invariant ones. This gives a criterion for establishing whether a system, whose equilibrium phase diagram is like that of Fig. 4.1, may undergo a dynamical phase transition once supplied initially with enough excess energy.

The arguments in Sec 4.2 suggest that such energy edge is related to an equilibrium phase diagram like that of Fig. 4.1. However, its existence must be proved on a case by case basis. This can be done in models whose spectrum can be exactly determined, as the case of the fully connected Ising model discussed in Sec. 4.3. In this case we showed that

the symmetry is dynamically restored due to the fact that the allowed eigenstates for the final Hamiltonian are all symmetry invariant.

An important observation is that, due to the fully connected limit the dynamical phase transition is related to the zero-temperature quantum phase transition, while it is actually unrelated to the finite temperature transition. This fact motivated us to search for a broken-symmetry edge in a broader class of models. In particular, we addressed this point in Sec. 4.4 where we showed that such occurrence is not necessarily accompanied to a phase diagram like that of Fig. 4.1. There, we showed that the existence of an energy edge can be inferred without determining the entire spectrum. In fact, in the fermionic Hubbard model this can be easily realized comparing the low-energy spectrum of the Hamiltonian $\mathcal{H}$ with that of $-\mathcal{H}$, which is actually the high-energy spectrum of $\mathcal{H}$. Therefore, in this specific problem the broken symmetry states occupy the high-energy part of the spectrum. In order to access these states we prepare highly excited initial states with finite order parameter and follow the dynamical evolution of the latter. As expected, the existence of the energy threshold is signaled by the survival at long times of the superconducting order parameter which can even grow with respect its initial value. To make a connection between the above result and the experiments in real materials, we must remark that model Hamiltonians $\mathcal{H}$, like the Hubbard model above, are meant to describe low energy properties of complex physical systems. Therefore, it is not unlikely that the value of the threshold energies extracted by comparing the low energy spectra of $\mathcal{H}$ and $-\mathcal{H}$ could be above the limit of applicability of the model itself.

Chapter 5

Non-equilibrium transport in strongly correlated heterostructures

5.1 Introduction

In the previous Chapter we discussed two different examples of unitary quantum dynamics in *closed* systems. The approximation of a closed system is related to the description of non equilibrium phenomena taking place on very short time scales, *i.e.* before the coupling with the external environment becomes effective. In this respect, it represents a good approximation for transient phenomena resulting from *e.g.* an ultrafast excitation of the system. On the other hand, it is clearly inappropriate for non-equilibrium phenomena in which the coupling with an external environment is a crucial ingredient. For instance, this is the case of the electronic transport through a finite size system. In fact, in order to sustain a finite stationary current, carriers have to be continuously supplied. Therefore the system must be considered *open* and the coupling with external reservoirs explicitly taken into account.

In Chaps. 2 and 3 we reviewed the experimental and theoretical facts that make the problem of the non-equilibrium transport across correlated systems a central issue in the non-equilibrium investigation of such systems. The two basic questions that we highlighted concern the formation of non-equilibrium stationary states resulting from the balancing effects of the driving field and a dissipative mechanism [67–69] and the non-linear behavior of the resulting stationary currents as a function of the applied fields [67, 73, 74, 76, 77]. This latter point is intimately connected to the problem of the electric breakdown in Mott insulators [26, 75, 86–89].

Although these problems have been investigated mainly in homogeneous situations, the presence of a driving electric-field in a correlated material naturally leads to consider heterostructured systems. This is because the non-linear transport properties are often probed in thin films or nanostructured devices for which the role of finite size effects and the coupling with external sources is crucial. Some works tackled this problem focusing on the properties of the stationary state [74, 86, 87], while the real-time dynamics in

inhomogeneous systems has been addressed by means of the time-dependent Gutzwiller approximation [99] and non-equilibrium DMFT [89, 100]. In the former case the focus was on the interaction quench problem in a layered system [99]. On the other hand the DMFT approach has been used to investigate the dynamics of photo-injected carriers and transport properties only deep in the Mott insulating state [89, 100]. Therefore, it is worth considering the investigation of the non-linear transport properties in the various regimes of a prototypical correlated material device.

In this Chapter we focus on this general problem studying the dynamics of an heterostructure composed of a finite size correlated system and two external semi-infinite metallic sources (leads). The external leads impose a finite bias across the system and, at the same time, provide a dissipative channel for the excess energy injected into the system.

This system shows interesting properties due to the presence of not-interacting/correlated metal interfaces. In fact, strong correlation can lead to remarkable effects at a surface or at an interface [101, 102]. In this respect the suppression or enhancement of the metallic character of a finite-size correlated system interfaced respectively with a metal or vacuum [102, 103] are relevant phenomena that deserve an investigation in non-equilibrium conditions.

In the following we firstly shall present the model and the method of solution within the time-dependent Gutzwiller approximation. Therefore we shall present the results considering separately the case of the metallic ($U < U_c$) or insulating ($U > U_c$) phase, being U_c the critical value of the Mott transition. In the metallic case we investigate the interface properties following the sudden coupling between the system and the leads. Next we discuss the formation of current-carrying stationary states in presence of a finite voltage bias arising from the balancing between the energy injection and the dissipation rate. Both of these processes depends directly on the value of the coupling between the slab and the leads. While for small couplings a stationary state can always be reached, at strong coupling the system gets trapped in a metastable state caused by an effective decoupling of the slab from the leads. We study the current-voltage characteristic of the system and demonstrate both the existence of a universal behavior with respect to interaction at small bias and the presence of a negative differential resistivity for larger applied bias.

We follow a similar analysis in the Mott insulating regime. We study first the dynamical formation of a metallic surface state, showing that this is appear as an exponential growth in time of the quasi-particle weight inside the slab bulk. Such quasi-particle weight becomes exponentially small in the bulk over a distance of the order of the Mott transition correlation length [102]. Finally, we show that for large enough voltage bias a conductive stationary state can be created from a Mott insulating slab with an highly non-linear current-bias characteristics. In particular, we show that the currents are exponentially activated with the applied bias and associate this behavior to a Landau-Zener dielectric breakdown mechanism.

5.2 Model and Method

We consider a strongly correlated slab composed by a series of N two-dimensional layers with in-plane and inter-plane hopping amplitudes and a purely local interaction term. We indicate the layer index with $z = 1, \ldots, N$ while we assume discrete translational symmetry on the xy plane of each layer. This enables us to introduce a two-dimensional momentum $\mathbf{k}$ so that the slab Hamiltonian reads

$$\begin{aligned} H_{\text{Slab}} &= \sum_{z=1}^{N} \sum_{\mathbf{k},\sigma} \epsilon_{\mathbf{k}} d^{\dagger}_{\mathbf{k},z,\sigma} d_{\mathbf{k},z,\sigma} \\ &+ \sum_{z=1}^{N-1} \sum_{\mathbf{k},\sigma} \Big(t_{z,z+1}\, d^{\dagger}_{\mathbf{k},z+1,\sigma} d_{\mathbf{k},z,\sigma} + H.c. \Big) \\ &+ \sum_{z=1}^{N} \sum_{\mathbf{r}} \left(\frac{U}{2}\, (n_{\mathbf{r},z} - 1)^2 + E_z\, n_{\mathbf{r},z} \right), \end{aligned} \tag{5.1}$$

where $\epsilon_{\mathbf{k}} = -2t \left(\cos k_x + \cos k_y \right)$ is the electronic dispersion for nearest-neighbor tight-binding Hamiltonian on a square lattice, $\mathbf{r}$ label the sites on each two-dimensional layer, $t_{z,z+1}$ is the inter-layer hopping parameter and E_z is a layer-dependent on-site energy. In the rest of the Chapter we assume $t_{z,z+1} = t$ and use $t = 1$ as energy unit.

A finite bias ΔV across the system is applied by coupling the slab to an external environment composed by two, left (L) and right (R), semi-infinite metallic leads described by not interacting Hamiltonians with symmetrically shifted energy bands

$$H_{\text{Lead}} = \sum_{\alpha=L,R} \sum_{\mathbf{k},k_\perp,\sigma} \left(\varepsilon^{\alpha}_{\mathbf{k}} + t^{\alpha}_{k_\perp} - \mu_\alpha \right) c^{\dagger}_{\mathbf{k}k_\perp\alpha\sigma} c_{\mathbf{k}k_\perp\alpha\sigma}, \tag{5.2}$$

where $k_\perp$ labels the $z-$component of the electron momentum. In Eq. (5.2) $\varepsilon^{\alpha}_{\mathbf{k}} = -2t_\alpha \big(\cos k_x + \cos k_y \big)$, $t^{\alpha}_{k_\perp} = -2t_\alpha \cos k_\perp$, where we shall assume $t_L = t_R = t$, and $\mu_{L/R} = \pm e\Delta V/2$, with e the electron charge (see Fig. 5.1). We couple the system to the metallic leads through a finite tunneling amplitude between the left(right) lead and the first(last) layer, i.e.

$$H_{\text{Hyb}} = \sum_{\alpha=L,R} \sum_{\mathbf{k},k_\perp,\sigma} \Big(v^{\alpha}_{k_\perp}\, c^{\dagger}_{\mathbf{k}k_\perp\alpha\sigma} d_{\mathbf{k}z_\alpha\sigma} + H.c. \Big), \tag{5.3}$$

where $z_L = 1$, $z_R = N$ and

$$v^{\alpha}_{k_\perp} = \sqrt{\frac{2}{N_\perp}}\, \sin k_\perp\, v_\alpha, \tag{5.4}$$

which corresponds to open boundary conditions for the leads along the $z-$direction.

The final Hamiltonian is thus the sum of Eqs. (5.1), (5.2) and (5.3)

$$H = H_{\text{Slab}} + H_{\text{Leads}} + H_{\text{Hyb}}. \tag{5.5}$$

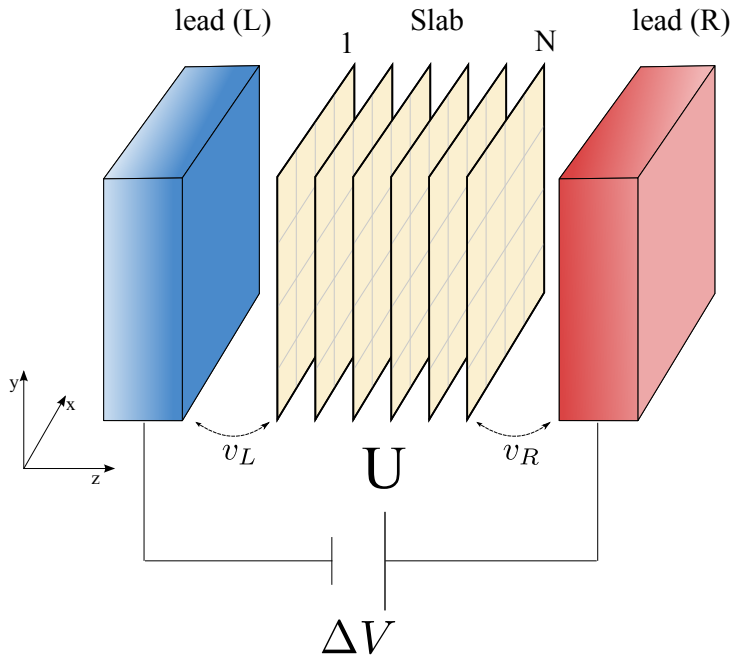

Fig. 5.1: Model. Sketch of the correlated slab sandwiched between semi-infinite metallic leads. v_L and v_R represent respectively left and right slab-leads hybridization coupling.

We drive the system out-of-equilibrium by suddenly switching the tunneling between the slab and the leads, that is $v_L(t) = v_R(t) = v_{\rm hyb}\,\theta(t)$, and by turning on a finite bias $\Delta V(t) = \Delta V\, r(t)$ according to a time-dependent protocol $r(t)$ that, if not explicitly stated, we also take as a step function. This double quench protocol is chosen for practical reasons with the aim of reducing the simulation time, after having explicitly verified that the initial state does not play a major role on the dynamics under finite bias. We exploit the local energies E_z in Eq. (5.1) to model the potential drop between left and right leads. Even though the profile of the inner potential should be self-consistently determined by the long range coulomb interaction, see e.g. Refs. [104] and [105], we assume that a flat profile $E_z = 0$ represents a reasonable choice for the system in its metallic phase, simulating the screening of the electric field inside the metal. On the other hand, in the insulating phase we shall assume a linear potential drop $E_z = e\Delta V(N+1-2z)/2(N+1)$ matching the left and right leads chemical potential for $z = 0$ and $z = N+1$. In the following we will assume the units $e = 1$ and $\hbar = 1$.

We study the dynamics within the time-dependent Gutzwiller (TDG) approximation extended to the case of inhomogeneous systems [99]. Similarly to the previous chapter we shall skip a detailed derivation highlighting the main steps that lead to the Gutzwiller dynamical equations for the present case of an inhomogeneous system coupled to semi-infinite leads. A more detailed derivation is reported in Appendix A.3.

As customary we split the Hamiltonian (5.5), $H = \mathcal{H}_0 + \mathcal{H}_{loc}$, into a not-interacting

term $\mathcal{H}_0$ and a purely local interaction part $\mathcal{H}_{loc}$

$$\begin{aligned}\mathcal{H}_0 = H_{\rm leads} + H_{\rm hyb} + \sum_{z=1}^{N}\sum_{\mathbf{k},\sigma}\epsilon_{\mathbf{k}}\, d^{\dagger}_{\mathbf{k},z,\sigma} d_{\mathbf{k},z,\sigma} \\ + \sum_{z=1}^{N-1}\sum_{\mathbf{k},\sigma}\Big(t_{z,z+1}\, d^{\dagger}_{\mathbf{k},z+1,\sigma} d_{\mathbf{k},z,\sigma} + H.c.\Big),\end{aligned} \tag{5.6}$$

$$\mathcal{H}_{loc} = \sum_{z=1}^{N}\sum_{\mathbf{r}} \frac{U}{2}\big(n_{\mathbf{r},z}-1\big)^2 + E_z n_{\mathbf{r},z} \equiv \sum_{\mathbf{R}} \mathcal{H}_{loc,\mathbf{R}}, \tag{5.7}$$

where $\mathbf{R} = (\mathbf{r}, z)$, and define the time-dependent variational wave-function already introduced in Eq. 4.31

$$|\Psi(t)\rangle = \prod_{\mathbf{R}} \mathcal{P}_{\mathbf{R}}(t)|\Psi_0(t)\rangle. \tag{5.8}$$

Upon imposing the constraints

$$\begin{aligned}\langle\Psi_0(t)|\, \mathcal{P}^{\dagger}_{\mathbf{R}}(t)\mathcal{P}_{\mathbf{R}}(t)\, |\Psi_0(t)\rangle = 1, \\ \langle\Psi_0(t)|\, \mathcal{P}^{\dagger}_{\mathbf{R}}(t)\mathcal{P}_{\mathbf{R}}(t)\, d^{\dagger}_{\mathbf{R}\sigma} d_{\mathbf{R}\sigma'}\, |\Psi_0(t)\rangle = \langle\Psi_0(t)|\, d^{\dagger}_{\mathbf{R}\sigma} d_{\mathbf{R}\sigma'}\, |\Psi_0(t)\rangle,\end{aligned} \tag{5.9}$$

and representing the $\mathcal{P}_{\mathbf{R}}(t)$ operators in terms of site-dependent matrices $\hat{\Phi}_{\mathbf{R}}(t)$, the enforcement of the saddle-point condition leads to the coupled dynamical equations

$$i\,\frac{\partial|\Psi_0(t)\rangle}{\partial t} = \mathcal{H}_*[\hat{\Phi}(t)]|\Psi_0(t)\rangle, \tag{5.10}$$

$$i\frac{\partial\hat{\Phi}_{\mathbf{R}}(t)}{\partial t} = \mathcal{H}_{loc,\mathbf{R}}\hat{\Phi}_{\mathbf{R}}(t) + \langle\Psi_0(t)|\frac{\partial\mathcal{H}_*[\hat{\Phi}(t)]}{\partial\hat{\Phi}^{\dagger}_{\mathbf{R}}(t)}|\Psi_0(t)\rangle, \tag{5.11}$$

where $\mathcal{H}_*[\hat{\Phi}(t)]$ is an effective not-interacting Hamiltonian that depends parametrically on the variational matrices $\hat{\Phi}_{\mathbf{R}}(t)$.

We use as local basis at site $\mathbf{R}$ the empty state $|0\rangle$, the doubly-occupied one, $|2\rangle$, and the singly-occupied ones, $|\sigma\rangle$ with $\sigma =\uparrow,\downarrow$ referring to the electron spin. We discard magnetism and s-wave superconductivity, so that the matrix $\hat{\Phi}_{\mathbf{R}}(t)$ can be chosen diagonal with matrix elements $\Phi_{\mathbf{R},00}(t) \equiv \Phi_{\mathbf{R},0}(t)$, $\Phi_{\mathbf{R},22}(t) \equiv \Phi_{\mathbf{R},2}(t)$, and $\Phi_{\mathbf{R},\uparrow\uparrow}(t) = \Phi_{\mathbf{R},\downarrow\downarrow}(t) \equiv \Phi_{\mathbf{R},1}(t)/\sqrt{2}$. Due to translational invariance within each xy plane, the variational matrices depend explicitly only on the layer index z, *i.e.* $\hat{\Phi}_{\mathbf{R}}(t) = \hat{\Phi}_z(t)$, and the constraints (5.9) are satisfied by imposing

$$|\Phi_{z,0}(t)|^2 + |\Phi_{z,2}(t)|^2 + |\Phi_{z,1}(t)|^2 = 1, \tag{5.12}$$

and

$$\delta_z(t) \equiv |\Phi_{z,0}(t)|^2 - |\Phi_{z,2}(t)|^2 = 1 - \sum_{\mathbf{k}\sigma}\langle\Psi_0(t)|\, d^{\dagger}_{\mathbf{k}z\sigma} d_{\mathbf{k}z\sigma}\, |\Psi_0(t)\rangle, \tag{5.13}$$

where $\delta_z(t)$ is the instantaneous doping of layer z. Through this choice we obtain the following effective Hamiltonian $\mathcal{H}_*[\hat{\Phi}(t)]$

$$\begin{aligned}\mathcal{H}_*[\hat{\Phi}(t)] = H_{\text{Leads}} &+ \sum_{z=1}^{N}\sum_{\mathbf{k},\sigma} |R_z(t)|^2\, \epsilon_{\mathbf{k}}\, d^\dagger_{\mathbf{k},z,\sigma} d_{\mathbf{k},z,\sigma} \\ &+ \sum_{z=1}^{N-1}\sum_{\mathbf{k},\sigma} \Big(R^*_{z+1}(t)\, R_z(t)\, d^\dagger_{\mathbf{k},z+1,\sigma} d_{\mathbf{k},z,\sigma} + H.c. \Big) \\ &+ \sum_{\alpha=L,R}\sum_{\mathbf{k},k_\perp,\sigma} \Big(v_{k_\perp}\, R_{z_\alpha}(t)\, c^\dagger_{\mathbf{k}k_\perp\alpha\sigma} d_{\mathbf{k}z_\alpha\sigma} + H.c. \Big),\end{aligned} \tag{5.14}$$

where the layer-dependent hopping renormalization factor reads

$$R_z(t) = \sqrt{\frac{2}{1-\delta_z(t)^2}} \left(\Phi_{z,0}(t)\Phi^*_{z,1}(t) + \Phi^*_{z,2}(t)\Phi_{z,1}(t) \right). \tag{5.15}$$

Straightforward differentiation of Eq. (5.14) with respect to $\hat{\Phi}^\dagger_z(t)$ yields the equations of motion for the variational matrices (5.11), which together with the effective Schrödinger equation (5.10) completely determine the variational dynamics within the TDG approximation. Though the derivation of the set of coupled dynamical equations is very simple, the final result is cumbersome so that we present it in the Appendix A.3 together with details on its numerical integration.

We characterize the non equilibrium behavior of the system by studying the electronic transport through the slab. In particular, in the following we shall define the electronic current flowing from the left/right lead to the first/last layer of the slab as the *contact current* with expression

$$j_\alpha(t) = -i \left[\sum_{\mathbf{k}\sigma}\sum_{k_\perp} v_{k_\perp} \langle \Psi(t)|\, d^\dagger_{\mathbf{k}z\sigma} c_{\mathbf{k}k_\perp\alpha\sigma}\, |\Psi(t)\rangle - c.c. \right], \tag{5.16}$$

and the *layer current* as the current flowing from the z-th to the $z+1$-th layer, i.e.

$$j_z(t) = -i \left[\sum_{\mathbf{k}\sigma} \langle \Psi(t)| d^\dagger_{\mathbf{k}z\sigma} d_{\mathbf{k}z+1\sigma} |\Psi(t)\rangle - c.c. \right]. \tag{5.17}$$

Within the TDG approximation these two observables read, respectively,

$$j_\alpha(t) = -i \Big[R^*_{z_\alpha}(t) \sum_{\mathbf{k}\sigma}\sum_{k_\perp} v_{k_\perp} \langle d^\dagger_{\mathbf{k}z\sigma} c_{\mathbf{k}k_\perp\alpha\sigma} \rangle - c.c. \Big] \tag{5.18}$$

and

$$j_z(t) = -i \Big[R^*_z(t) R_{z+1}(t) \sum_{\mathbf{k}\sigma} \langle d^\dagger_{\mathbf{k}z\sigma} d_{\mathbf{k}z+1\sigma} \rangle - c.c. \Big], \tag{5.19}$$

where $\langle \ldots \rangle \equiv \langle \Psi_0(t)| \ldots |\Psi_0(t)\rangle$. Notice that, due to the left/right symmetry, $j_L = -j_R$ and we need only to consider currents for $z \leq N/2$. Together with the real time observables dynamics, we will consider the corresponding time averages defined by

$$\langle O(t) \rangle \equiv \frac{1}{t} \int_0^t d\tau O(\tau), \tag{5.20}$$

where $O(t)$ represents the real time dynamics of a generic observable.

In the following sections we present the non-equilibrium dynamics of this model starting from the strongly correlated metallic phase $U < U_c$ where $U_c \simeq 16$ is the critical value for the Mott-transition. Eventually we discuss the results in the Mott-insulating phase.

5.3 Non-equilibrium transport in the strongly correlated metal

5.3.1 Zero-bias dynamics

To start with we shall consider the dynamics at zero-bias $\Delta V = 0$. In this case we assume that the non-equilibrium perturbation is the sudden switch of the tunnel amplitude $v_{\rm hyb}$ between the correlated slab and the leads. In the equilibrium regime, the metallic character at the un-contacted surfaces is strongly suppressed with respect to the bulk as effect of the reduced kinetic energy. This suppression, commonly described in terms of a surface *dead layer*, extends over a distance which is quite remarkably controlled by a critical correlation length ξ associated to the Mott transition. Indeed ξ is found to grow approaching the metal-insulator transition and diverges at the transition point [102]. In presence of a contact with external metallic leads the surface state is characterized by a larger quasi-particle weight with respect to that of the bulk irrespective of its metallic or insulating character, realizing what is called a *living layer* [103]. As we shall see in the following, by switching on $v_{\rm hyb}$ it should be possible to turn the dead layer into the living one on a characteristic time scale τ: The dynamical counterpart of the correlation length ξ.

In Fig. 5.2 we show the time-evolution of the layer-dependent quasi-particle weight $Z_z(t) \equiv |R_z(t)|^2$ for a $N = 20$ slab and different values of the interaction U. The dynamics shows a characteristic light-cone effect, *i.e.* a constant velocity propagation of the perturbation from the junctions at the external layers $z = 1$ and $z = N$ to the center of the slab. After few reflections the light-cone disappears leaving the system in a stationary state. The velocity of the propagation is found to be proportional to the bulk quasi-particle weight hence it decreases as the Mott transition is approached for $U \to U_c$.

The boundary layers are strongly perturbed by the sudden switch of the tunneling amplitude. In particular, we observe in Fig. 5.3(a) that the surface *dead layers* rapidly transform into *living layers* with stationary quasi-particle weights greater than the bulk ones and equal to the equilibrium values for the same set-up [103]. This has to be expected since the energy injected is not extensive. On the contrary, the bulk layers are weakly

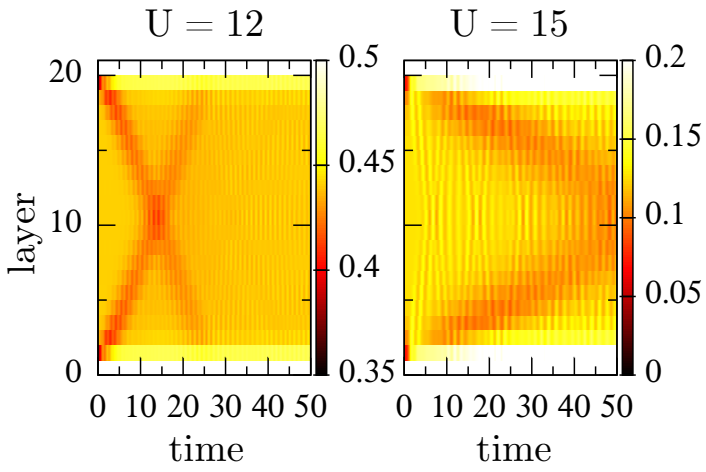

Fig. 5.2: Quasi-particle weight dynamics in the zero-bias regime. Layer-resolved dynamics of the local quasi-particle weights $|R_z(t)|^2$ for a slab of $N = 20$ layers and two values of the interaction U. The slab-lead hybridization is equal to the inter-layer hopping amplitude $v_{\rm hyb} = 1.0$.

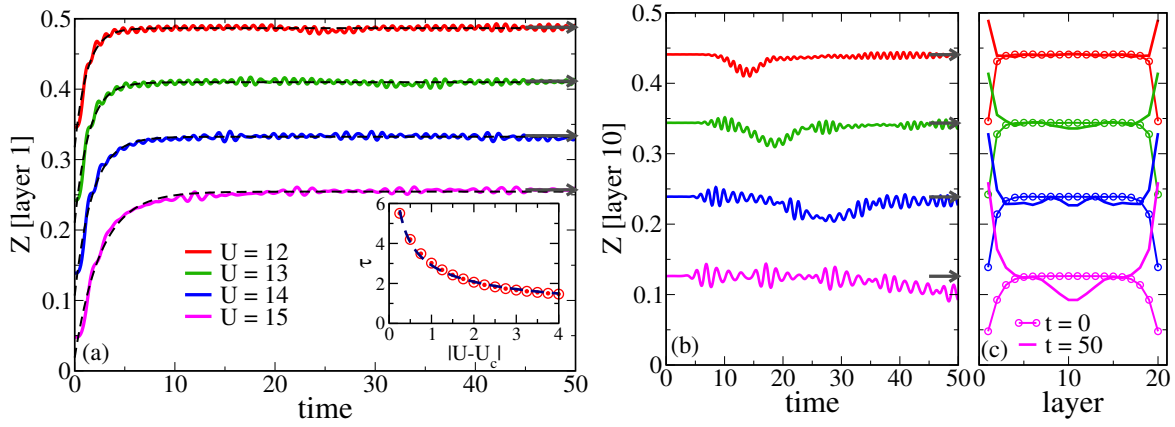

Fig. 5.3: Surface and bulk quasi-particle weight dynamics in the zero-bias regime. (a) Dynamics of the local quasi-particle weight for the first layer. Dashed lines are the fitting curves obtained with Eq. (5.21). Arrows represent the hybridized slab equilibrium values. Inset: dead layer awakening time as a function of U. Dashed lines represents the fitting curve $\tau = \alpha/|U - U_c|^{\nu_*}$ with $\nu_* \approx 0.4895$ (b) Dynamics of the local quasi-particle weight for the bulk ($z = 10$) layer. Arrows represent the hybridized slab equilibrium values. (c) Quasi-particle weight profiles at times $t = 0$ (dotted lines) and $t = 50$ (lines).

affected by the coupling with the metal leads, see Fig. 5.3(b). Their dynamics is only affected by small oscillations and temporary deviations from the stationary values due to the perturbation propagation described by the light-cone reflections.

We characterize the evolution from the *dead* to the *living* layer by fitting the dynamics of the boundary layer quasi-particle weight with an exponential relaxation towards a stationary value:

$$Z(t) = Z_{\text{dead}} + \Big(Z_{\text{living}} - Z_{\text{dead}}\Big)\Big(1 - e^{-t/\tau}\Big). \tag{5.21}$$

As illustrated in Fig. 5.3(b) the dynamics shows a slowing-down upon approaching the Mott transition. In particular the dead-layer wake-up time τ diverges as $\tau \sim |U - U_c|^{-\nu_*}$ when we approach the critical value U_c with a critical exponent that we estimate as $\nu_* = 0.4895$, very close to the mean-field value $\nu_* = 1/2$. Such a mean-field dependence, similar to that of the correlation length $\xi \sim |U - U_c|^{-1/2}$ [103] implies, through $\tau \sim \xi^{\zeta}$, a dynamical critical exponent $\zeta = 1$.

5.3.2 Small-bias regime

We shall now focus on the dynamics in the presence of an applied bias. In the Fig. 5.4 we report the results for the real-time dynamics of the currents at the contacts and layers, defined by Eqs. (5.19)–(5.18), after a sudden switch of the bias ΔV and a flat inner potential.

We observe that the contact and the layer currents display very similar dynamics, characterized by a monotonic increase at early times and a saturation to stationary values at longer times. The stationary dynamics displays small undamped oscillations around the mean value due to oscillations of the layer-dependent electronic densities (see Fig. 5.4(b)). The persistence of oscillations, *i.e.*the absence of a true relaxation to a steady-state, is a characteristic of the essentially mean-field nature of the method. However, this problem can be overcome either by time-averaging the signal or, as shown in the inset of Fig. 5.4, using a finite-time switching protocol $r(t)$ for the voltage bias. In both cases we end up with the same currents and density profiles, which are almost flat as a function of the layer. The flat profile of the density is the expected for a metal as result of the electric field screening. This validates the choice for a flat inner potential profile in the metallic regime of the slab.

We highlight that the non-equilibrium dynamics is strongly dependent on the coupling between the system (correlated slab) and the external environment (leads), represented in this case by the slab-lead tunneling amplitude v_{hyb}. This is evident from the stationary value of the current that increases as a function of v_{hyb}, as expected since this latter sets the rate of electrons/holes injection from the leads into the slab. Furthermore, the coupling to an external environment is essential to redistribute the energy injected into the system after a sudden perturbation so to lead to a final steady state characterized by a stationary value of the internal energy. In order to study the competition between energy dissipation and energy injection rate we plot, in Fig. 5.5, the time-dependence of

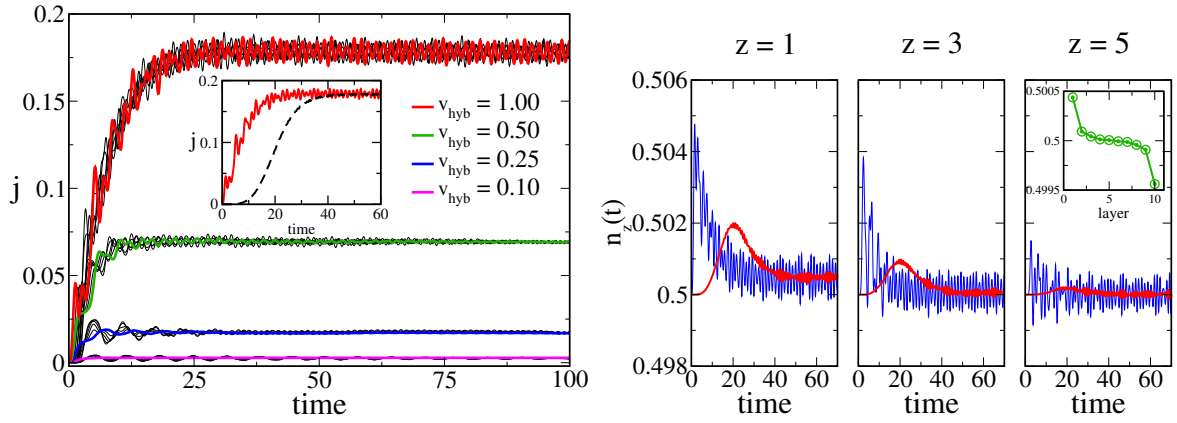

Fig. 5.4: Current and density dynamics in the small bias regime. Top: Real-time dynamics of the currents computed at the slab-lead contact (thick lines) and between two neighboring layers (light grey lines) after a bias quench with $\Delta V = 0.5$ and $U = 12$. for a $N = 10$ slab and different values of the slab-leads coupling $v_{\rm hyb}$. Inset: Current dynamics for a ramp-like switching protocol $r(t) = [1 - 3/2\cos(\pi t/\tau_*) + 1/2\cos(\pi t/\tau_*)^3]/4$ compared to the sudden quench limit ($\tau_* = 30$). Bottom: Dynamics of the local electronic densities $n_z(t)$ for the $1^{\rm st}$, $3^{\rm rd}$ and $5^{\rm th}$ layer and $v_{\rm hyb} = 1.0$. Inset: stationary density profile showing an almost flat density distribution with slightly doped regions near the left and right contacts.

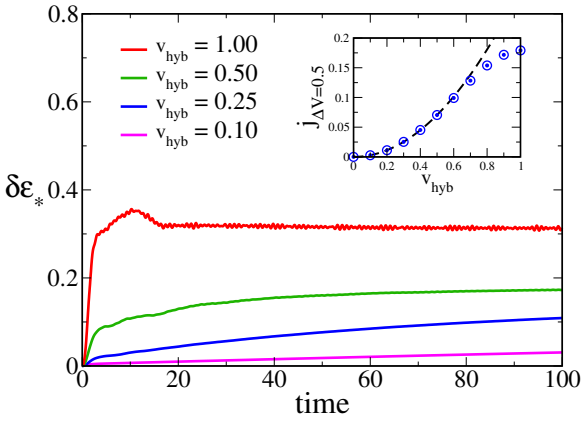

Fig. 5.5: Slab internal energy evolution. Relative variation of the slab internal energy as defined in Eq. 5.22 for the same set of parameters of Fig. 5.4. Inset: Stationary current for $\Delta V = 0.5$ as a function of the hybridization with the leads with a fitting curve $j(v_{\rm hyb}) = j_0\, v_{\rm hyb}^2$ (dashed line).

the relative variation of the slab internal energy with respect to its equilibrium value:

$$\delta\epsilon_*(t) \equiv \frac{E_*(t) - E_*(t=0)}{|E_*(t=0)|}, \tag{5.22}$$

where

$$\begin{aligned} E_*(t) \equiv & \langle\Psi(t)|H_{\rm Slab}|\Psi(t)\rangle \approx \langle\Psi_0(t)|\mathcal{H}_*\left[\hat{\Phi}(t)\right]|\Psi_0(t)\rangle \\ & + \sum_z {\rm Tr}\left(\hat{\Phi}_z(t)^\dagger \mathcal{H}_{loc,z}\hat{\Phi}_z(t)\right). \end{aligned}$$

The last expression holds within the TDG approximation. We observe the existence of two regimes as a function of the coupling to the leads $v_{\rm hyb}$. When the system is weakly coupled to the external environment the energy shows an almost linear increase in time without ever reaching any stationary value. This indicates that the dissipation mechanism is not effective on the scale of the simulation time. For larger values of $v_{\rm hyb}$, the dissipation mechanism becomes more effective. The internal energy shows a faster growth at initial times, due to the larger value of the current setting up through the system. Further increasing the coupling (see the case $v_{\rm hyb} = 1.0$ in the figure) the initial fast rise of the energy is followed by a downturn towards a stationary value, which in turn is reached very rapidly. As shown in the inset of Fig. 5.5 the crossover between the non-dissipative and dissipative regimes coincides with the point in which the current deviates from linear-response theory – which predicts a quadratically increasing current $j \propto v_{\rm hyb}^2$– and bends towards smaller value.

5.3.3 Large-bias regime

The interplay between the energy injection and the dissipation highlighted in the dynamics of the slab internal energy (Fig. 5.5) is a direct consequence of the fact that in the present model these two mechanisms are controlled by the coupling with the same external environment. Therefore, we may envisage a situation in which the internal energy of the slab grows so fast that the leads are unable to dissipate the injected energy preventing a stationary current to set in. This phenomenon occurs at large values of the voltage bias ($\Delta V \gtrsim 1$) and of the tunneling amplitude $v_{\rm hyb}$, *i.e.*when the slab is rapidly kicked away from equilibrium. In order to illustrate this point we report in Fig. 5.6 (left panels) the current dynamics for the same parameters as in the previous Fig. 5.4 but for larger value of the voltage bias $\Delta V = 2.0$. We observe that, while for weak tunneling ($v_{\rm hyb} = 0.1$) the current flows to a steady state, upon increasing $v_{\rm hyb}$ the stationary state can not be reached and strong chaotic oscillations characterize the long-time evolution.

Indeed, the inability of reaching a steady-state is intertwined with the fast increase of the slab internal energy, as revealed by the results in the right panel of Fig. 5.6. In particular, for $v_{\rm hyb} = 1.0$ the relative variation of the internal energy rapidly reaches $\delta\epsilon_*(t) \approx 1$, after which it starts to oscillate chaotically just like the currents does. The same behavior shows up in the dynamics of the quasi-particle weight averaged over all

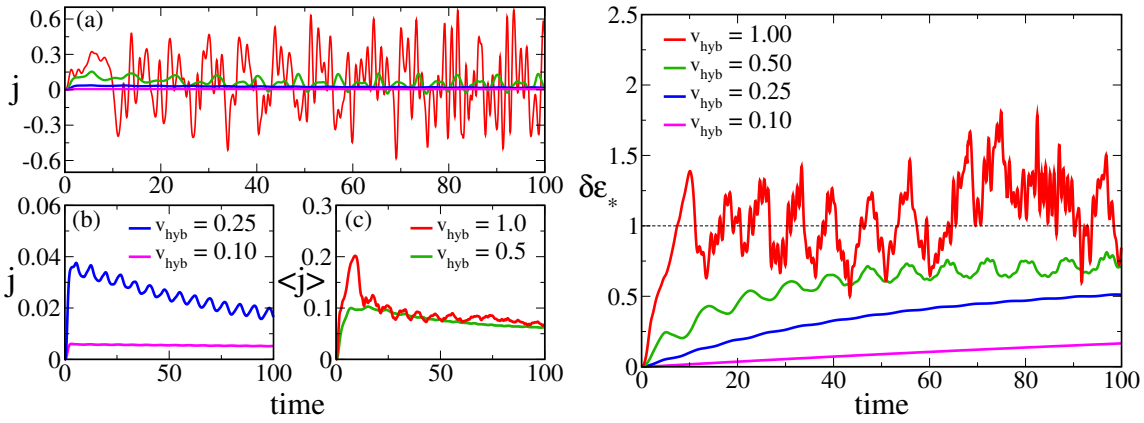

Fig. 5.6: Current and energy variation dynamics in the large bias regime. Left: (a) Real-time dynamics for the contact currents for the same parameters and values of hybridization coupling of Fig. 5.4 and $\Delta V = 2.0$. (b) Blow-up of the currents dynamics for $v_{\rm hyb} = 0.1$ and $v_{\rm hyb} = 0.25$. (c) Dynamics of the current time average $\langle j(t) \rangle$ as defined in the main text for $v_{\rm hyb} = 0.5$ and $v_{\rm hyb} = 1.0$. Right: Dynamics of the relative energy variation.

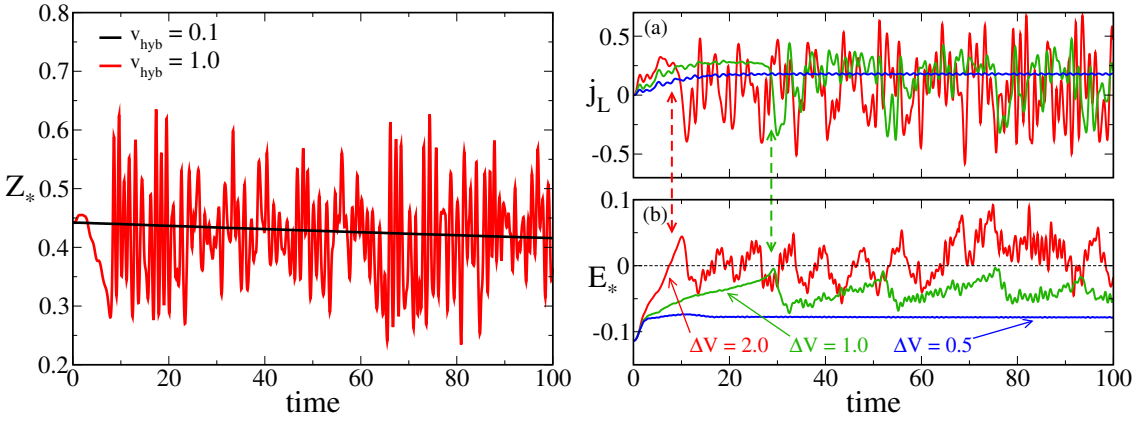

Fig. 5.7: Quasi-particle weight dynamics in large bias regime and current-energy comparison. Left: Dynamics of the mean quasi-particle weight for the same parameters in Fig. 5.6 and $v_{\rm hyb} = 0.1$ (black line) and $v_{\rm hyb} = 1.0$ (red line). Right: Current (a) and internal energy dynamics (b) for $U = 12$, $v_{\rm hyb} = 1.0$ and three values of the applied bias. The occurrence of the breakdown of the stationary dynamics due to the dynamical transition is highlighted by the vertical arrows.

layers:

$$Z_*(t) \equiv \frac{1}{N}\sum_{z=1}^{N} Z_z(t) = \frac{1}{N}\sum_{z=1}^{N} |R_z(t)|^2 \,, \tag{5.23}$$

which displays fast and large oscillations whereas it is smooth in the case of small $v_{\rm hyb}$ (see Fig. 5.7, left panel).

This behavior is similar to that observed across the dynamical phase-transition in the half-filled Hubbard model after an interaction quench [48, 49] occurring when the injected energy exceeds a threshold. This correspondence is further supported by noting that the onset of chaotic behavior occurs precisely when the internal energy $E_*(t)$ of the slab reaches zero (see Fig. 5.7, right panel). The value $E_* = 0$ is indeed the energy of a Mott insulating wave-function within the Gutzwiller approximation. This anomalous behavior thus suggests that as soon as the energy crosses zero $E_*(t) \geq 0$ the system gets trapped into an insulating state characterized by a strongly suppressed tunneling into the metal. This prevents the excess energy to flow back into the leads and therefore the relaxation to a metal with a steady current.

The absence of such a steady current blocks the indefinite increase of the slab internal energy, which indeed is found to suddenly decrease after the current collapse. In this condition current-carrying states can be reconstructed, until this eventually brings again the internal energy to its threshold value $E_* \approx 0$. This behavior determines the strong oscillations in the current dynamics visible in Figs. 5.6-5.7. In particular, in Fig. 5.7 (right panel) we highlight the different times at which the current-carrying state is temporary destroyed using vertical arrows connecting the currents and energy dynamics.

We associate this behavior to a shortcoming of the TDG approximation, which does not include all the dissipative processes and therefore artificially enhances the stability of such a metastable state. If we want to compare this behavior with a real system, we can argue that the TDG description only describes a transient state produced by the large initial heating of the slab that is temporarily pushed into a high-temperature incoherent phase of the Hubbard model, which takes a long time to equilibrate back with the metal leads but evidently not the infinite time that the TDG approximation suggests. This behavior is similar to what has been observed by DMFT in the case of an homogeneous system driven by a static electric field in the absence of external dissipative channels. [67].

In the case of an interaction quench it was found that, even though the absence of a true exponential relaxation is faulty, the time-averaged values of observables as obtained within the TDG approximation might still be representative of the true dynamics [49, 93] . This allows us to define a sensible current by time averaging the real-time evolution, which indeed approaches a finite value at long enough times (see Fig. 5.6(c), left panel).

5.3.4 Current-bias characteristics

The overall picture emerging from the investigation of the metallic case is summarized by the evolution of the current as a function of the bias (current-bias characteristic) for different values of the interaction strength.

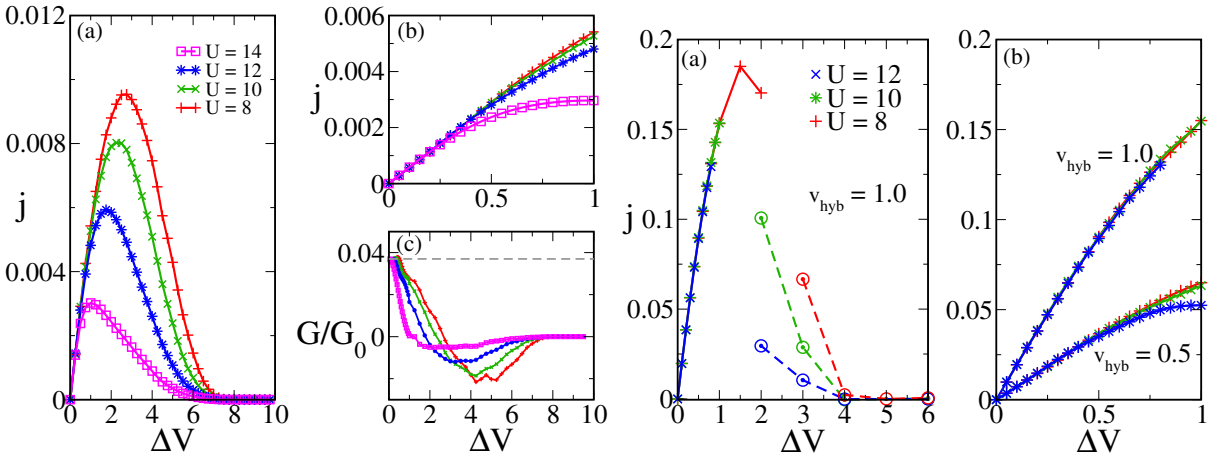

Fig. 5.8: Current-bias characteristics in the metallic phase. Left: (a) current-bias characteristics for a $N = 10$ slab for different values of U and $v_{\rm hyb} = 0.1$. (b) blow-up of the linear part of the current-bias characteristics. (c) differential conductance measured respect to the quantum conductance $G_0 = 1/2\pi$ in the present units. Grey line represents the universal zero-bias value. Right: (a) current-bias characteristics for a $N = 10$ slab, different values of U and $v_{\rm hyb} = 1.0$. Plus, cross and star symbols represents stationary currents values, while circles represent converged currents time averages values. Right: (b) : blow-up of the linear part of the current-bias characteristics for $v_{\rm hyb} = 0.5$ and $v_{\rm hyb} = 1.0$, showing universal zero-bias conductivity $G/G_0 \approx 0.452$ and 1.203 respectively.

In the limit of weak coupling to the external environment, we have seen that the currents display a stationary dynamics in a wide range of bias values. In Fig. 5.8 (left panels) we report these stationary values as a function of the bias for $v_{\rm hyb} = 0.1$ and a wide range of interaction strengths.

All the curves show a crossover between a linear regime at small bias and a monotonic decrease for larger values. This behavior is similar to what was already observed in different contexts [67, 73, 76, 77]. We connect the drop of the current for large biases to the reduction of energy overlap between the leads and the slab electronic states at large bias. Indeed, in a single particle picture the current should collapse to zero when $\Delta V = 2W$, being W the bandwidth associated to the longitudinal dispersion [106], *i.e.* $W = 4t_\perp$, so that in this case the current suppression occurs for $\Delta V \gtrsim 8$. In the linear regime we find that the zero-bias differential conductance $G(0) = \partial j/\partial \Delta V|_{\Delta V=0}$ is universal with respect to the interaction strength [74, 107] as expected when the electronic transport is determined only by the low-energy quasi-particle excitations.

Within the TDG approximation this fact can be easily rationalized by noting that quasi-particles are controlled by the non-interacting Hamiltonian $\mathcal{H}_*$ in Eq. (5.14), characterized by a hopping amplitude renormalized by the factors $|R| \leq 1$. This leads to an enhancement of the quasi-particle density of states by a factor $\nu \sim 1/|R|^2$ that at low bias compensates the reduction of tunneling rate into the leads. Conversely, as the bias increases the current-bias characteristics starts deviating from the universal low-bias behavior and becomes strongly dependent on the interaction strength U [74]. In particular, the crossover between the positive and the negative differential conductance regimes gets

shifted towards smaller values of the bias as U is increased as effect of the shrinking of the coherent quasi-particle density of states.

As discussed in the previous section, increasing the coupling to the external environment leads to a chaotic regime at large bias, in a regime where we cannot identify anymore a stationary current. However, as mentioned above, we can still extract a meaningful estimate of the current through its time-average Eq. (5.20), restricting to the range of bias for which the latter is well converged. This is explicitly illustrated in Fig. 5.8 (right panel) for the current-bias characteristics at $v_{\rm hyb}=1.0$. The open circles represent currents computed using converged time averaged while the other symbols represent currents characterized by a stationary dynamics. These results show that the curves have qualitatively the same features of the small $v_{\rm hyb}$ case with a universal linear conductance and a crossover to a negative conductance regime.

5.4 Dielectric breakdown of the Mott insulating phase

We now move the discussion to the effect of an applied voltage bias to a slab which is in a Mott insulating regime because $U > U_c$. Unlike the metallic case, we now assume that the field penetrates inside the slab, leading to a linear potential profile of the form $E_z = \Delta V(N+1-2z)/2(N+1)$ matching the chemical potential of the left and right leads for $z=0$ and $z=N+1$ respectively.

5.4.1 Evanescent bulk quasi-particle

Within the Gutzwiller approximation the Mott insulator is characterized by a vanishing number of doubly occupied and empty sites as well as by a zero renormalization factor $R=0$, leading to a trivial state with zero energy. However, it has been shown that in the presence of the metallic leads *evanescent* quasi-particles [103, 108] appear inside the insulating slab. This is revealed by a finite quasi-particle weight which is maximum at the leads and decays exponentially in the bulk of the slab with a characteristic length $\xi \sim (U-U_c)^{-1/2}$ which defines the critical correlation length of the Mott transition [103].

In Fig. 5.9 (left panels) we show the dynamics of the formation of *evanescent* quasi-particles after the sudden switch on of the coupling to the leads $v_{\rm hyb}$. We observe a rapid increase of the quasi-particle weight as soon as the coupling is switched on. The rapid increase can be reasonably well parameterized as an exponential with a characteristic growth time τ. The results for τ^{-1} reported in the inset of the left panel of Fig. 5.9 clearly show that the increase of the quasi-particle weight becomes faster as the Mott transition is approached. Interestingly, the exponential growth is not limited to the boundary layers close to the leads, but it is present throughout the slab, with a characteristic time $\tau(z)$ which is nearly uniform in space.

Such an exponential growth is suggestive of a dynamics driven by the combined action of the high-energy excitations (Hubbard bands) and of the quasi-particles, which within the Gutzwiller approach can be associated to the variational parameters $\Phi_{z,n}(t)$ and to the non-interacting Slater determinant $|\,\Psi_0(t)\rangle$, respectively. Indeed, we can support

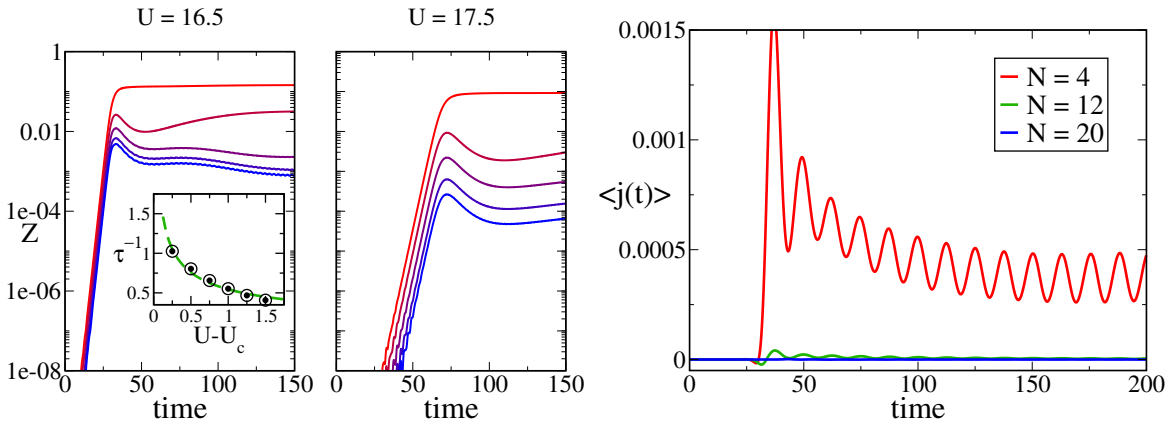

Fig. 5.9: Quasi-particle weight dynamics at zero-bias in the Mott phase. Left: Real-time dynamics for the quasi-particle weights from layer 1 to 5 (from top to bottom) of a $N = 10$ Mott insulating slab suddenly coupled to the metallic leads ($v_{\rm hyb} = 1.0$). $U = 16.5$ and $U = 17.5$. Inset: inverse of the characteristic time for the exponential quasi-particle formation $\tau^{-1} \sim (U - U_c)^{-\nu_*}$, $\nu_* \approx 0.4753$. Right: Time-averaged currents for three slabs with applied bias $\Delta V = 0.5$. $U = 16.5 > U_c$, $v_{\rm hyb} = 1.0$ and $N = 4, 12, 20$ (from top to bottom).

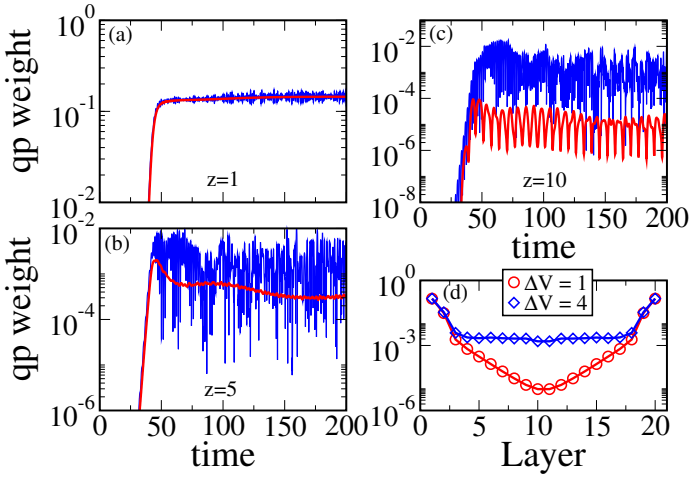

Fig. 5.10: Quasi-particle weight dynamics at finite bias in the Mott phase. Layer dependent quasi-particle weight dynamics for layers 1 (a), 5(b) and 10(c) of a $N = 20$ slab, $U = 16.5$, $v_{\rm hyb} = 1.0$ and two values of the applied bias $\Delta V = 1.0$(red lines) and $\Delta V = 4.0$ (blue lines). (d): time-averaged stationary quasi-particle weight profile.

this statement by a simplified analytical calculation reported in Appendix A.3.3. As outlined in Appendix A.3.3, we can reproduce the long-time approach to the steady state corresponding to evanescent quasi-particles at equilibrium, considering a simplified dynamics in which we neglect the dynamics of the Slater determinant $|\,\Psi_0(t)\rangle$ and take into account only that of $\Phi_{z,n}(t)$. The latter can be analytically written in terms of a Klein-Gordon-like equation for the hopping renormalization factors $R(z,t)$

$$\frac{1}{c^2}\,\ddot{R}(z,t) - \nabla^2\,R(z,t) + m^2\,c^2\,R(z,t) = 0, \tag{5.24}$$

with parameters (see Appendix A.3.3):

$$c^2 = \frac{u}{24}, \qquad m^2c^2 = 6(u-1) = \xi^{-2}, \tag{5.25}$$

with $u \equiv U/U_c$. As anticipated above the simplified dynamics described by Eq. 5.24 correctly captures the long-time behavior of the system, but it can not reproduce the short time exponential growth. In the latter regime the time evolution is indeed governed by the interplay between Hubbard bands and quasi-particles, responsible for the evanescent quasi-particle formation into the Mott insulating slab, which is neglected in the approximation leading to Eq. 5.24.

The presence of the evanescent bulk quasi-particle provides a conducting channel across the slab, possibly leading to finite currents upon the application of a finite bias. In particular, we expect that if the slab length is smaller than the decay length ξ every finite bias ΔV is sufficient to induce a finite current through the slab. On the other hand we expect the current to be suppressed when the slab is longer than ξ This is confirmed by the results reported in Fig. 5.9 (right panel) where we show the average current for a bias $\Delta V = 0.5$, in the linear regime in the metallic case, and different slab sizes N. A finite current is rapidly injected for small $N = 4$, whereas it does not for larger systems (*e.g.* $N = 12$ or $N = 20$).

5.4.2 Dielectric breakdown currents

Increasing the value of the applied bias we observe an enhancement of the quasi-particle weight throughout the slab. This effect is illustrated in Fig. 5.10 where panels (a-c) show the dynamics of the quasi-particle weights in a driven Mott insulating slab with different values of the bias for three different layers ($z = 1, 5, 10$). While the dynamics is characterized by strong oscillations reminiscent of the incoherent dynamics discussed in Sec. 5.3 for the metallic slab under a large applied bias, the time-averaged quantities in the long-time limit converge to stationary values. The spatial distribution as a function of the layer index shows a strong enhancement in the bulk upon increasing the bias (Fig. 5.10d).

Such enhancement results in a finite current flowing. Indeed, as shown in Fig. 5.11 (left panel), the time-averaged current has a damped oscillatory behavior that converges towards a steady value, although the real-time dynamics follows a seemingly chaotic pattern (see the inset). As in the metallic case, we checked that when a finite current

sets in the resulting local charge imbalance is so small that the correction to the inner potential profile due to long-range Coulomb repulsion is negligible.

We extract the stationary values by fitting the current time-averages with:

$$\langle j(t) \rangle = j_{\text{steady}} + \frac{\alpha}{t}. \tag{5.26}$$

As evident by looking at the results reported in Fig. 5.11 (left panel), the stationary value of the current has a non-linear behavior as a function of the applied bias. This effect can be better appreciated in the next Fig. 5.11 (right panel), where we plot the current-voltage characteristics for increasing values of the slab size N.

Interestingly, the current displays an exponential activated behavior with a characteristic threshold bias which can be described by

$$j_{\text{steady}}(\Delta V) = \gamma \, \Delta V \, \mathrm{e}^{-\Delta V_{\text{th}}/\Delta V}. \tag{5.27}$$

Indeed, data for the current agree very well with the fit (5.27) for $\Delta V \gtrsim 2$, while the fit becomes inaccurate for smaller values of the voltage bias. We motivate the discrepancy in this regime of very small currents with the presence of spurious effects, such as for example a small residual current carried out by the evanescent quasi-particles, or a slight inaccuracy in the estimate of such tiny currents. These spurious effects becomes irrelevant when the current becomes sizeable, *i.e.* at larger values of the bias.

From the fits of the current-bias characteristics we obtain a linearly increasing threshold bias ΔV_{th} as a function of the slab size N (see inset of the Fig. 5.11, right panel). This behavior indicates a crossover from a bias to an electric field induced breakdown mechanism, as the slab size N is increased [109]. Thus, in the large-N limit the threshold electric field $E_{\text{th}} = \Delta V_{\text{th}}/N$ saturates to a constant value E_{th} and we rewrite Eq. (5.27) as:

$$\frac{j_{\text{steady}}(\Delta V)}{\Delta V} = \gamma \, \mathrm{e}^{-E_{\text{th}}/E}, \tag{5.28}$$

with $E_{th} \approx 0.85$, the saturation value extracted from the slope of the threshold bias. This expression is suggestive of a Landau-Zener type of dielectric breakdown[75, 81], in agreement with the results obtained within DMFT studies of either homogeneous [88] and inhomogeneous systems [86, 89]. Moreover, as already pointed out in Sec. 2.2.3, such dielectric breakdown mechanism has been recently proposed to explain the outcome of conductance experiments in thin films of strongly correlated materials [25].

We further support the Gutzwiller scenario for the dielectric breakdown with the simple calculation for the stationary regime outlined in the Appendix A.3.2, which follows the analysis reported in Ref. [103] for the equilibrium case. In particular, we consider a single metal-Mott insulator interface in the presence of an electro-chemical potential $\mu(z)$ and compute the resulting quasi-particle weight inside the insulating side. As detailed in A.3.2, we find that for weak $\mu(z)$, the hopping renormalization factor $R(z)$ satisfies the equation

$$\nabla^2 R(z) = \left(m^2 c^2 - \frac{2\mu(z)^2}{c^2} \right) R(z), \tag{5.29}$$

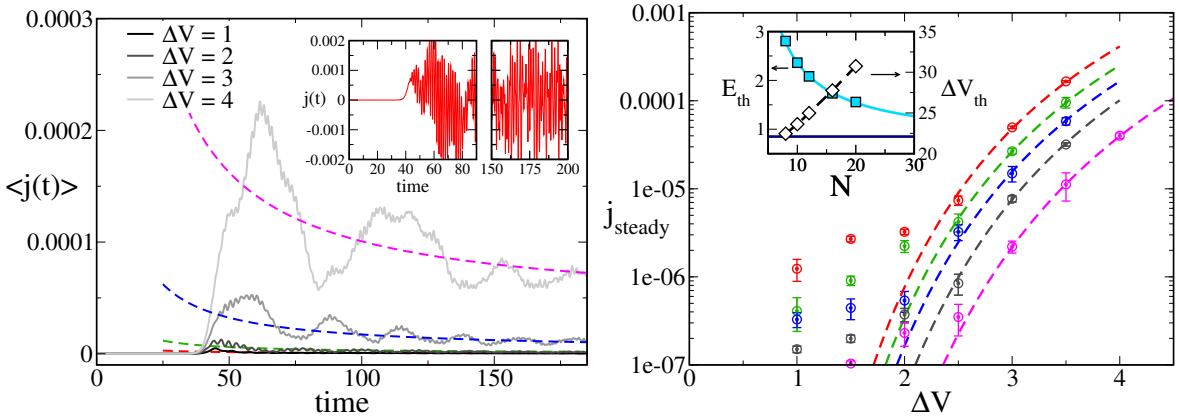

Fig. 5.11: Current dynamics and current-bias characteristics in the Mott phase. Left: Time-averaged currents for the same parameters in Fig. 5.10 and $\Delta V = 4.0, 3.0, 2.0$ and 1.0 (from top to bottom). Dashed lines are fitting curves from Eq. (5.26). Inset: Real time dynamics of the current for $\Delta V = 4.0$. Right: Current bias characteristics for $U = 16.5$ and different values of the slab length $N = 8, 10, 12, 16$ and 20 (from top to bottom). Dashed lines represent fitting curves with Eq. (5.27). Insets: threshold bias $\Delta V_{\rm th}$ and electric field $E_{\rm th} = \Delta V_{\rm th}/N$ as a function of the slab size. The horizontal line is the extrapolation for the large-N size independent electric field.

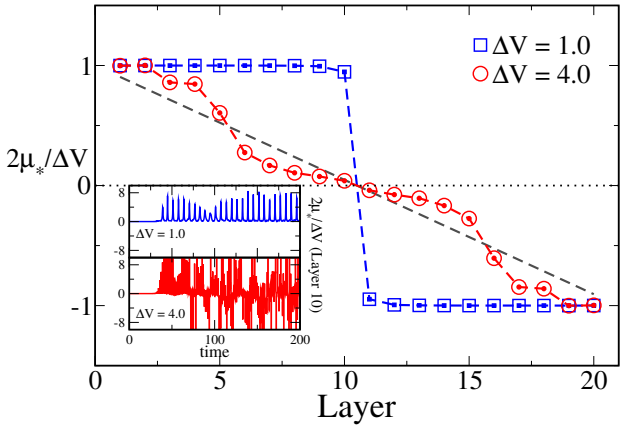

Fig. 5.12: Quasi-particle weight effective chemical potential. Layer-dependent quasi-particle effective chemical potential profile. Parameters are the same of Fig. 5.11 for $\Delta V = 1$ and $\Delta V = 4$. The grey dashed line represents the applied bias linear profile. Inset: Real-time dynamics of the quasi-particle chemical potential on the $10^{\rm th}$ layer. All data are plotted with respect to the leads' chemical potential absolute value $\Delta V/2$.

which is nothing but the stationary Klein-Gordon equation (5.24) in the presence of a field, or alternatively, the Schrœdinger equation of a particle impinging on a potential barrier. This equation identifies an avoided region through which electrons can tunnel under the effect of the electro-chemical potential $\mu(z)$, in a way similar to the Zener tunneling mechanism originally discussed in Ref. [27] (see Fig. 2.4 in Chap. 2). For a constant electric field $\mu(z) = E\,z$ and within the WKB approximation, we obtain the stationary transmission probability beyond the turning point z_* of the barrier (see Appendix A.3.2):

$$|R(z > z_*)|^2 \sim \exp\left(-\frac{E_{\rm th}}{E}\right), \tag{5.30}$$

where

$$E_{\rm th} = \frac{\pi}{2}\sqrt{\frac{u}{48}}\,\xi^{-2}, \tag{5.31}$$

with the definition of the correlation length $\xi^{-1} = \sqrt{6(u-1)}$ of Ref. [103]. This calculation identifies the transmission probability (Eq. 5.30) with the dielectric breakdown currents (Eq. 5.28) and predicts via the definition of the correlation length (Eq. 5.25) a threshold electric field increasing with the interaction strength [88].

Finally, we note that the threshold field obtained from the numerical results (see Fig. 5.11) and analytical estimates (Eq. 5.31) is consistent with the rough estimate $E_{\rm th} \sim \Delta/\xi$ valid of a Mott insulator with a gap Δ and a correlation length ξ. Indeed, for $\Delta \sim U$ and $\xi \sim (u-1)^{-1/2}$ we find, in the large-U limit, $E_{\rm th} \sim U^{3/2}$ matching the analytical estimate in Eq. 5.31. On the other hand, setting the energy and length units to $t \sim 0.1$ eV and $a \sim 1$ Å, the numerical results show that $E_{\rm th} \sim 1$ V/nm which is valid for typical Mott gap of the order of 1eV and ξ of few lattice spacings. As we discussed in the introductory chapters, such threshold values overestimate of about one/two order of magnitude the experimentally observed fields for Landau-Zener like breakdown [25] and even more for other mechanisms such as the avalanche breakdown [38].

5.4.3 Quasi-particle energy distribution

Inspired by the evidence that in the above description the transport activation is driven by an enhancement of the bulk quasi-particle weight [see Fig. 5.10(d)] in this section we focus on the spatial distribution of the quasi-particle energy throughout the slab. In order to estimate the time evolution of the quasi-particle energy levels we compute the time-evolution of the layer-dependent chemical potential in the effective non-interacting model Eq. 5.14, introduced by the coupling to external voltage bias. This quantity can be easily extracted by means of the following unitary transformation of the uncorrelated wave-function:

$$|\varphi_0(t)\rangle \equiv \mathcal{U}(t)\,|\Psi_0(t)\rangle\,,\ \mathcal{U}(t) = \prod_{\mathbf{r},z} \exp\left[i\lambda_z(t)\,\hat{n}_{\mathbf{r},z}\right] \tag{5.32}$$

where $\lambda_z(t)$ is the time-dependent phase of the hopping renormalization parameters $R_z(t) \equiv \rho_z(t)e^{i\lambda_z(t)}$, with real $\rho_z(t) \geq 0$. Substituting Eq. (5.32) into Eq. (5.10) we obtain a transformed Hamiltonian that now contains only real hopping amplitudes at the

cost of introducing a time-dependent local chemical potential terms $\mu_*(z,t)$, namely:

$$i\partial_t|\varphi_0(t)\rangle = h_*(t)\ |\varphi_0(t)\rangle \tag{5.33}$$

where the effective Hamiltonian reads:

$$\begin{aligned} h_*(t) = H_{\text{Leads}} &+ \sum_{z=1}^{N}\sum_{\mathbf{k},\sigma} \rho_z(t)^2\,\epsilon_{\mathbf{k}}\, d^\dagger_{\mathbf{k},z,\sigma} d_{\mathbf{k},z,\sigma} \\ &+ \sum_{z=1}^{N-1}\sum_{\mathbf{k},\sigma} \Big(\rho_{z+1}(t)\,\rho_z(t)\ d^\dagger_{\mathbf{k},z+1,\sigma} d_{\mathbf{k},z,\sigma} + H.c.\Big) \\ &+ \sum_{\alpha=L,R}\ \sum_{\mathbf{k},k_\perp,\sigma} \Big(v_{k_\perp}\rho_{z_\alpha}(t) c^\dagger_{\mathbf{k}k_\perp\alpha\sigma} d_{\mathbf{k}z_\alpha\sigma} + H.c.\Big) \\ &+ \sum_{z=1}^{N}\sum_{\mathbf{k},\sigma} \mu_*(z,t)\, d^\dagger_{\mathbf{k},z,\sigma} d_{\mathbf{k},z,\sigma}, \end{aligned} \tag{5.34}$$

and with $\mu_*(z,t) = \frac{\partial}{\partial t}\lambda_z(t)$ that plays the role of an effective chemical potential for the quasi-particles under the influence of the bias.

From the time-average of this quantity in the long-time regime we obtain the energy profile as a function of the position in the slab of the stationary quasi-particle effective potential, reported in Fig. 5.12, locating the energies of the quasi-particles injected from the leads into the slab. As expected, for any value of the applied voltage bias the quasi-particles near the boundaries are injected at energies equal to the chemical potentials of the two leads, *i.e.* $\mu_* = \pm\Delta V/2$. On the other hand, the behavior inside the bulk of the slab depends strongly on the value of the applied bias.

At a small bias, represented in Fig. 5.12 by $\Delta V = 1$, a value corresponding to an exponentially suppressed current, the chemical potential remains essentially flat as the bulk is approached from any of the two leads, despite the presence of a linear potential drop E_z. This gives rise to a step-like chemical potential profile with a jump $\Delta\mu_* \approx \Delta V$ at the center of the slab. The presence of this jump suppresses the overlap between the quasi-particle states on the two sides, preventing the tunneling from the left metallic lead to the right one and ultimately leading to an exponential reduction of the current.

On the opposite limit of a large enough bias (*e.g.* $\Delta V = 4$) a finite current flows through the slab, corresponding to a smoother profile of effective chemical potentials. Indeed, in the bulk $\mu_*(z)$ takes a weak linear drop behavior as expected for a metal, and slightly reminiscent of the applied linear potential drop E_z. In this regime the large overlap between quasi-particle states near the center of the slab allows quasi-particle to easily tunnel from the left to the right side, giving rise to a finite current as outlined in the previous Fig. 5.11.

The disappearance of the effective chemical potential discontinuity in the middle of the slab for large bias is determined by the presence of strong oscillations of this quantity between positive and negative values, as shown in the inset of Fig. 5.12. This suggests that, even though the quasi-particle chemical potential averages to an almost zero value

at very long times, the quasi-particles dynamically visit electronic states far away from the local Fermi energies. We interpret this behavior as the signal of a strong feedback of the dynamics of the local degrees of freedom Eq. (5.11) onto the quasi-particle evolution, due to the proximity of a resonance between quasi-particles and the incoherent Mott-Hubbard side bands. Interestingly, even though in this description there is no high-energy incoherent spectral weight, this scenario is reminiscent of the formation of coherent quasi-particle structures inside the Hubbard bands as observed in previous studies using steady-state formulation of non-equilibrium DMFT [86].

5.5 Conclusions

We used the out-of-equilibrium extension of the inhomogeneous Gutzwiller approximation to study the dynamics of a correlated slab contacted to metallic leads in the presence of a voltage bias. On one side this allowed us to investigate the non-equilibrium counterpart of known interface effects arising in strongly correlated heterostructures, such as the *dead* and *living* layer phenomena. On the other, we also studied the non-linear electronic transport of quasi-particles injected into the correlated slab under the influence of an applied bias.

In the first part we considered a slab in a metallic state in the absence of the bias, when the correlation strength is smaller than the critical value for a Mott transition. Initially we focused on the zero-bias regime and studied the spreading of the doubly occupied sites injected into the slab after a sudden switch of a tunneling amplitude with the metal leads. Specifically we found a ballistic propagation of the perturbation inside the slab, leaving the system in a stationary state equal to the equilibrium one, with an excess of double occupancies concentrated near the contacts and a consequent enhancement of the quasi-particle weight at the boundaries of the slab. We characterized this "awakening" dynamics of the *living* layer from the initial *dead* one in terms of a characteristic time-scale which diverges at the Mott transition. This divergence allow us to identify this timescale as the dynamical counterpart of the equilibrium correlation length ξ [102].

In the presence of a finite bias we addressed the formation of non-equilibrium states, characterized by a finite current flowing through the correlated slab. We demonstrated that this process is strongly dependent on the coupling with the external environment represented by the biased metal leads, which at the same time act as the source of the non-equilibrium perturbation and as the only dissipative channel. For weak coupling between the leads and the slab we found stationary currents flowing in a wide range of bias. Conversely for large couplings we identified a strong-bias regime in which the system is trapped into a metastable state characterized by an effective slab-leads decoupling. This is due to an exceedingly fast energy increase and to the lack of strong dissipative processes in the Gutzwiller method, which prevents the injected energy to flow back into the leads and the current to reach a stationary value. Studying the current-bias characteristics in the range of parameter for which the system is able to reach a non equilibrium stationary state, we observed a crossover from a low-bias linear regime, which we find universal with respect to the interaction U, to a regime with negative differential conductance typical

of finite bandwidth systems. Considering suitable long-time averages of the current we have been able to observe the same phenomenology in the region of parameters for which, due to the aforementioned anomalous heating, the current dynamics does not lead to an observable stationary value.

In the second part we turned our attention to the dynamical effect of a bias on a Mott insulating slab, when the interaction strength exceeds the Mott threshold. Following the analysis carried out in the metallic case, we considered the formation of evanescent bulk quasi-particles after a sudden switch of the slab-leads tunneling amplitude in a zero-bias setup. In this case, we found that the *living* layer formation is accompanied by an exponential growth of the quasi-particle weight, suggestive of a strong feedback between the dynamics of the quasi-particles and the local degrees of freedom.

In the presence of a finite bias, we studied the conditions under which these evanescent quasi-particles can lead to the opening of a conducting channel through the insulating slab. We showed that at very low bias this is the case only for a very small slab, for which the correlation length ξ is of the same order of the slab size. For larger samples we found that the currents are exponentially activated with a threshold bias $\Delta V_{\rm th}$ which increases with the slab size. This behavior is suggestive of a Landau-Zener type of dielectric breakdown. We supported this scenario with the calculation, in the stationary regime, of the tunneling amplitude for a quasi-particle through an insulating slab.

Chapter 6

Electric-field driven resistive transition in Mott insulators

6.1 Introduction

In the previous Chapter, we discussed the non-equilibrium transport properties of a correlated material described within the framework of the single band Hubbard model. This model is the simplest one entailing the basic properties of a correlated material and, as a matter of fact, it was introduced in the early sixties [110–112] to describe the mechanism leading to an insulating state in a half-filled band, *i.e.* the competition between the kinetic energy, which tends to delocalize electrons throughout the lattice, and the Coulomb interaction which significantly constraints the electronic motion [113, 114]. Besides the metal-insulator transition, other typical properties of most correlated material, such as the low-temperature antiferromagnetic phase, are correctly captured by the model [115].

While the equilibrium properties described by the Hubbard model are quite ubiquitous among correlated materials, it is hard to extend this statement to general non-equilibrium behaviors. In this respect the problem of a correlated system driven by an external electric field is a paradigmatic example. As we discussed in Chap. 5, in the presence of an external electric-field, the Hubbard model describes what we could call a *rigid* Mott insulator: its insulating electronic properties are not modified by the application of the external field and conducting states appear, similarly to ordinary band insulators, with the promotion of carriers from the lower to the upper Hubbard bands. In real materials similar behaviors can be observed in the conducting properties of systems which are deep in the insulating state [25] (see Fig. 2.4) or in field-effect transistors built with wide-gap Mott insulator, *e.g.* Ni or Cu monoxides [32, 33].

On the contrary, several materials behaves more like *soft* Mott insulators, in the sense that their electronic properties undergoes a significant adaptation in response to external driving fields. For instance, recent experiments on narrow-gap insulators (see Sec. 2.2.3), V_2O_3, $NiS_{2-x}Se_x$ and $GaTa_4Se_8$ [26, 38], show that the insulating state can be sharply turned into a metal by means of fields orders of magnitude lower than the gap. The

conditions under which such kind of resistive switch is possible are still unclear and their thoroughly comprehension may play a relevant role also for other kind of experiments in which the transition is induced either by means of voltage bias [34, 40] or by femtoseconds laser pulses [15, 24]. The experimental outcomes were rationalized in a scenario in which the external-bias is able to stabilize a metastable metallic phase (see Sec. 3.2.2), relating the switch to the first-order nature of the Mott transition. Although the first-order character of the Mott-transition is a common feature of correlated materials which is captured by the Hubbard model [115], the results reported in the previous chapter and in related works [75, 81, 88] clearly show that such kind of behavior can be hardly described within this model framework.

A possible explanation may lie in the fact that the Hubbard model represents an oversimplified description of real correlated materials, thus failing in capturing a complex phenomenon such that of the dielectric breakdown. This should not be simply regarded as an escape route, but in fact it has a justification based on physical arguments. In fact, it is plausible that for systems close to the Mott transition, or in which the insulating gap is different from the standard Mott gap [116], additional degrees of freedom may play a relevant role in the reorganization of the electronic properties induced by the applied field [117]. At the same time, it is also reasonable that the single band description becomes appropriated for systems which are deep in the insulating phase where the physics is completely dominated by a large insulating gap. In this respect, the Hubbard model clearly does not account for the multi-orbital nature of most correlated materials whose electronic properties directly originate from partially filled d or f shells. For instance, as shown in Ref. [65] this circumstance is crucial to describe the stabilization of a gap-collapsed metal in a pump-excited Mott insulator.

In this Chapter we shall follow this point of view to address the issue of the resistive transitions in Mott insulators considering a general model which extends the standard single band Hubbard model. In particular, we will consider an additional orbital degree of freedom with a small crystal-field lifting of degeneracy between the two orbitals. We study the evolution of the electronic properties of the system as a function of an applied external electric field and show that this model does realize a non-Zener breakdown. This is signaled by a sharp electric field driven insulator-to-metal transition. We relate this occurrence to the fact that, at equilibrium, the metal-insulator transition separates two solutions which cannot be continuously connected one to each other and, therefore, coexist in a large region across the Mott transition. Comparing the results of this two-band model with that achievable in the single band Hubbard one, we highlight the distinctive static and dynamical features that sharply discriminate between such resistive transition and the standard tunneling breakdown.

6.2 The Model

We start from a very simple model comprising two bands of equal width split by a crystal-field Δ. We consider an average population of two electrons per site, so that the system is globally half-filled, and introduce a local rotationally invariant Coulomb interaction U.

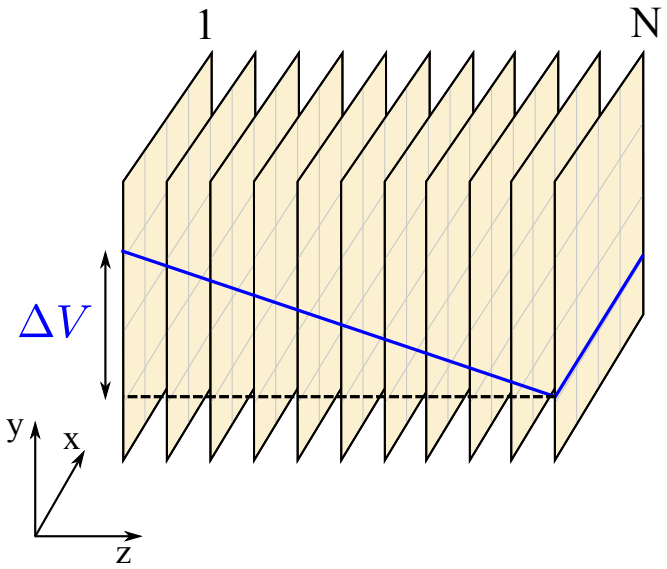

Fig. 6.1: The slab geometry with a finite voltage drop ΔV: We consider a three-dimensional layered structure with a linear voltage drop symmetric with respect to the center of the slab.

The Hamiltonian on a three-dimensional cubic lattice reads

$$\mathcal{H} = \sum_{\mathbf{k}\sigma} \sum_{\alpha,\beta=1}^{2} t_{\mathbf{k}\alpha\beta}\, c^{\dagger}_{\mathbf{k}\alpha\sigma}\, c_{\mathbf{k}\beta\sigma} - \frac{\Delta}{2} \sum_{i} \left(n_{i,1} - n_{i,2}\right) + \frac{U}{2} \sum_{i} \left(n_i - 2\right)^2, \tag{6.1}$$

where $n_{i,\alpha} = \sum_{\sigma} c^{\dagger}_{i\alpha\sigma} c_{i\alpha\sigma}$ and $n_i = \sum_{\alpha} n_{i,\alpha}$, while $t_{\mathbf{k}11} = t_{\mathbf{k}22} = -2t\,(\cos k_x + \cos k_y + \cos k_z)$ is the intra-band dispersion. We also add a non-local hybridization $t_{\mathbf{k}12} = t_{\mathbf{k}21} = v\,(\cos k_x - \cos k_y)\cos k_z$ which guarantees that the local single-particle density matrix is diagonal in the orbital index.

The model can be regarded as a backbone description of a large variety of correlated materials. In fact, it entails the basic features common to several correlated compounds, namely the multi-orbital structure, arising from partially filled d and f shells, and the lifting of the orbital degeneracy determined by the anisotropy of the surrounding crystal structure.

We consider a constant electric field directed along the z-axis, $\vec{E} = E\vec{z}/z$, which we express in the Coulomb gauge in terms of a linearly varying potential

$$V(z) = V_0 - Ez. \tag{6.2}$$

To this extent we introduce a three-dimensional layered structure (Fig. 6.1) and fix the reference potential value V_0 imposing a symmetric voltage drop $\Delta V/2$ respect to its center

$$V(z) = -\frac{\Delta V}{2} + \Delta V \frac{z-1}{N-1}. \tag{6.3}$$

The Hamiltonian for the slab structure is obtained performing a discrete Fourier trans-

form along the $z-$direction of the fermionic operators defined in momentum space

$$c^{\dagger}_{\mathbf{k}_{\parallel} z\alpha\sigma} = \sqrt{\frac{2}{N+1}} \sum_{k_z} \sin(k_z) c^{\dagger}_{\mathbf{k}\alpha\sigma}, \tag{6.4}$$

where the explicit form of the basis functions takes into account the open conditions which we impose on the boundaries of the system. Using a vector representation for the orbitals fermionic operators $\hat{c}^{\dagger}_{\mathbf{k}_{\parallel} z\sigma} \equiv \left(c^{\dagger}_{\mathbf{k}_{\parallel} z1\sigma},\ c^{\dagger}_{\mathbf{k}_{\parallel} z2\sigma} \right)$ and setting to unity the elementary charge $e = 1$ we obtain

$$\begin{aligned} \mathcal{H} = & \sum_{\mathbf{k}_{\parallel}\sigma} \sum_{z=1}^{N} \hat{c}^{\dagger}_{\mathbf{k}_{\parallel} z\sigma} \cdot \boldsymbol{h}_{\mathbf{k}_{\parallel}} \cdot \hat{c}_{\mathbf{k}_{\parallel} z\sigma} + \sum_{\mathbf{k}_{\parallel}\sigma} \sum_{z=1}^{N-1} \hat{c}^{\dagger}_{\mathbf{k}_{\parallel} z\sigma} \cdot \boldsymbol{t}_{\mathbf{k}_{\parallel}} \cdot \hat{c}_{\mathbf{k}_{\parallel} z+1\sigma} + H.c. \\ & + \frac{\Delta}{2} \sum_{z=1}^{N} \sum_{i\in z} (n_{i,z,1} - n_{i,z,2}) + \frac{U}{2} \sum_{z=1}^{N} \sum_{i\in z} (n_{iz} - 2)^2 - \sum_{z} \sum_{i\in z} V(z) n_{i,z}, \end{aligned} \tag{6.5}$$

where $V(z)$ is the scalar potential defined by Eq. 6.3 and the matrices $\boldsymbol{h}_{\mathbf{k}_{\parallel}}$ and $\boldsymbol{t}_{\mathbf{k}_{\parallel}}$ contain respectively the intra- and inter- layer hopping amplitudes

$$\boldsymbol{h}_{\mathbf{k}_{\parallel}} = \begin{pmatrix} \epsilon_{\mathbf{k}_{\parallel}} & 0 \\ 0 & \epsilon_{\mathbf{k}_{\parallel}} \end{pmatrix}, \quad \boldsymbol{t}_{\mathbf{k}_{\parallel}} = \begin{pmatrix} -t & v_{\mathbf{k}_{\parallel}} \\ v_{\mathbf{k}_{\parallel}} & -t \end{pmatrix} \quad \text{with} \quad \begin{cases} \epsilon_{\mathbf{k}_{\parallel}} = & -2t\,(\cos k_x + \cos k_y) \\ v_{\mathbf{k}_{\parallel}} = & v\,(\cos k_x - \cos k_y) \end{cases}. \tag{6.6}$$

In what follows we take $t = 0.5$ and $v = 0.25$ in our energy units, and $\Delta = 0.4$ so that, at $U = 0$, the model describes a metal with two overlapping bands.

We solve the model using the extension of the DMFT formalism to inhomogeneous systems [118]. This approach is based on the assumption that the self-energy encoding the effects of all the many-body correlation is purely local in space and explicit dependent on the layer index z

$$\boldsymbol{\Sigma}_{iz,jz'}(i\omega_n) = \delta_{ij}\delta_{zz'}\boldsymbol{\Sigma}_z(i\omega_n). \tag{6.7}$$

Following the standard DMFT approach [115], the layer-dependent self-energies are then extracted from a set of layer-dependent single-site effective problems which are self-consistently determined imposing the condition that the lattice local Green's function $\boldsymbol{G}^{-1}_{zz}(i\omega_n)$ computed using such local self-energy is equal to the Green's function of the effective single-site problem. Indicating with $\boldsymbol{\mathcal{G}}^{-1}_{0,z}(i\omega_n)$ the bare propagators which define the effective single-site problems this condition leads to the following equations which provide an implicit relation between $\boldsymbol{G}^{-1}_{zz}(i\omega_n)$ and $\boldsymbol{\mathcal{G}}^{-1}_{0,z}(i\omega_n)$

$$\boldsymbol{G}_{zz}(i\omega_n) = \sum_{\mathbf{k}_{\parallel}} \boldsymbol{G}_{\mathbf{k}_{\parallel} zz}(i\omega_n), \qquad \boldsymbol{G}^{-1}_{zz}(i\omega_n) = \boldsymbol{\mathcal{G}}^{-1}_{0,z}(i\omega_n) - \boldsymbol{\Sigma}_z(i\omega_n) \tag{6.8}$$

$$\hat{\boldsymbol{G}}^{-1}_{\mathbf{k}_{\parallel}}(i\omega_n) = i\omega_n \mathbb{I} - \hat{\boldsymbol{T}}_{\mathbf{k}_{\parallel}} - \hat{\boldsymbol{\mathcal{H}}}_{loc} - \hat{\boldsymbol{\Sigma}}(i\omega_n), \tag{6.9}$$

where we indicate with $\hat{\boldsymbol{G}}(i\omega_n)$ the $2N \times 2N$ matrix constructed with all the 2×2 $\boldsymbol{G}_{zz'}(i\omega_n)$ matrices. The matrix $\hat{\boldsymbol{T}}_{\mathbf{k}_{\parallel}}$ contains all the $\mathbf{k}_{\parallel}$-dependent hopping amplitudes from the

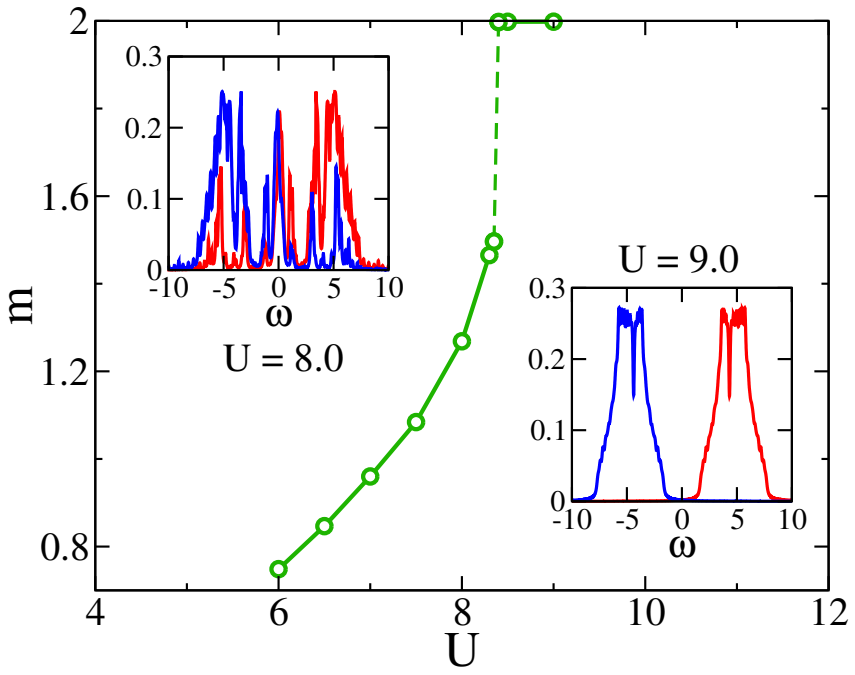

Fig. 6.2: Metal-insulator transition for the model 6.1 in a cubic lattice. The green-dotted line shows the orbital polarization (see main text) as a function of the interaction U. In the insets we show the local spectral functions $A^{1,2}_{Loc}(\omega) = -\frac{1}{\pi}G^{1,2}_{Loc}(\omega)$ for the metallic ($U = 8.0$) and insulating ($U = 9.0$) cases. Blue/red lines represent orbitals 1 and 2 respectively.

layer z and orbital α to the layer z' and orbital α'. $\hat{\boldsymbol{\mathcal{H}}}_{loc}$ and $\hat{\boldsymbol{\Sigma}}(i\omega_n)$ are block diagonal matrices containing all the local energies (crystal-field and scalar potential) and local self-energies respectively. See Appendix B.2 for further details. In practice Eqs. 6.8-6.9 are self-consistently solved mapping the effective single-site problems onto independent interacting Anderson impurities which we solve using the Exact Diagonalization scheme based on a discrete bath representation.

6.3 Metal-to-insulator transition

At zero-bias the system shows a metal-to-insulator transition for $U = U_c$ which is driven by the correlation enhancement of the crystal field splitting. This effect can be easily described within the mean-field ansatz $\langle n_{1,2} \rangle = 1 \pm m/2$ which leads to the effective splitting between the two orbitals

$$\Delta_{eff} = \Delta + U\frac{m}{2}, \tag{6.10}$$

being $m = n_1 - n_2$ the orbital polarization. As the interaction is increased the upper band depopulates and the system turns from a partially polarized ($m < 2$) metal for $U < U_c$

into an almost fully polarized ($m \lesssim 2$) [1] insulator $U > U_c$.

In the simple Hartree-Fock picture we would expect a continuous Lifshitz transition taking place when Δ_{eff} exceeds the bandwidth. In Fig. 6.2 we show that the effect of dynamical correlations, neglected by Hartree-Fock and captured instead by DMFT, dramatically alters this picture. There we plot the orbital polarization computed as a function of U for a single-site homogeneous version of the model 6.1 on a cubic lattice. The results clearly show that the dynamical correlations turn the continuous Lifshitz transition into a first-order transition for $U = U_c \simeq 8.35$ signaled by the finite jump of the orbital polarization.

Although this fully polarized insulator has been often classified as a trivial band insulator [119, 120], the above results show that the model gives a natural representation of the paramagnetic metal-insulator transition for a generic correlated material. Indeed, it describes an half-filled metal which is sharply turned into an insulator due to the effect of the electron-electron interactions. In addition, the model correctly captures already at zero-temperature the first-order nature of the metal-insulator transition, a peculiarity of correlated materials. In this sense we can safely call this metal-insulator transition a Mott transition, bearing in mind that the mechanism driving the transition is different from the usual charge localization as described by the single-band Hubbard model.

As a matter of fact, the spectral features of the solutions on both sides of the transition, showed in the insets of Fig. 6.2 entail the fingerprints of strong correlations. On the metallic side $U = 8.0$, the two spectral functions completely overlap leading to a wide peak at the Fermi level and two high-energy features reminiscent of preformed Hubbard bands. These latter eventually separate when the central peak is destroyed leading to a gapped insulating state for $U > U_c$ with a gap of the order $\Delta + U \sim U$, being $\Delta \ll U$.

6.4 Field driven insulator-to-metal transition and metal-insulator coexistence

We now turn our attention to the effect of the electric-field on the Mott transition described in the previous section. To this extent we consider the slab geometry in Fig. 6.1 and starting from $U > U_c$, *i.e.* in the insulating phase for $\Delta V = 0$, we solve the model at different values $\Delta V \neq 0$. The $\Delta V = 0$ value of the metal-insulator critical interaction is $U_c \simeq 7.85$, being renormalized with respect to the previous case by finite size effects.

In Fig. 6.3 we present the evolution of the the local density of states for a representative bulk layer of a $N = 40$ slab (see Fig. 6.1) as a function of the applied electric-field $E = \Delta V/N$. At small bias (red region) the ground state is the finite gap insulator described in the previous section. Upon increasing ΔV a sharp modification of the spectral properties appears. The local density of states clearly acquires finite spectral weight at the Fermi level suggesting a field-induced insulator transition occurring for $E = E_{th} \gtrsim 0.01$.

[1] The system can never be exactly fully polarized $m = 2$ due to the effect of the non-local hybridization term

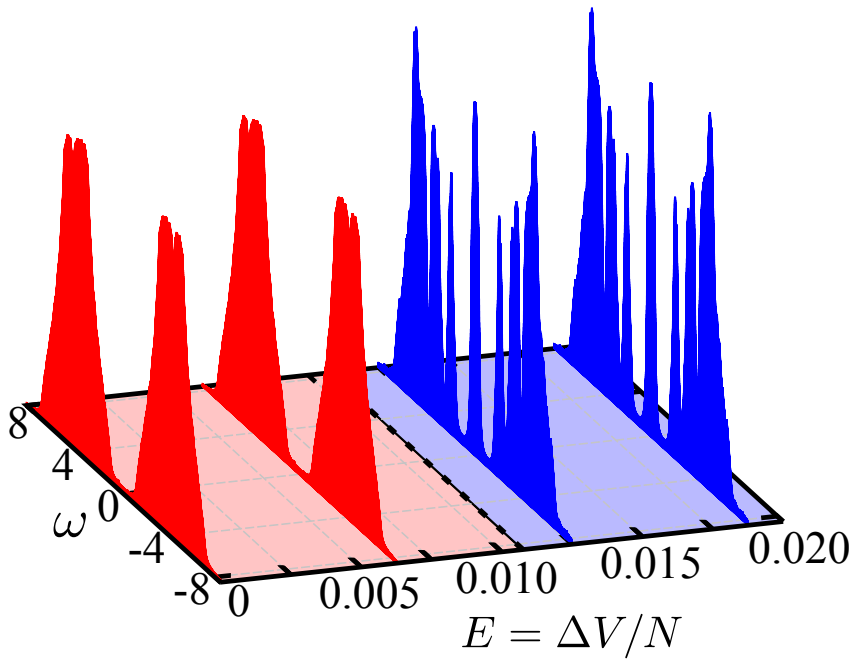

Fig. 6.3: The electric-field induced insulator to metal transition. Local density of states for a bulk layer of a $N = 40$ slab as a function of the applied electric field (see Fig. 6.1); $U = 7.9$. The spectral density is summed over the two orbitals. Red and blue regions indicates insulating and metallic solutions respectively.

The discontinuous character of both the electric-field driven and of the zero-bias transitions strongly suggests an hidden insulator-metal coexistence. Indeed, as shown by Fig. 6.4 (a) the bias-driven metallic solution can be extended up to zero bias where it coexists with the insulating ground state. At $E = 0$ the insulating solution has lower energy. However, the energy of the metallic solution rapidly decreases on increasing E, while that of the insulator stays practically constant. Therefore with further increasing the electric field the two solutions have to cross and the system thus turns abruptly into a metal. As shown by the panel (b) of Fig. 6.4 , the energy gain for the metallic solution is related to a finite gradient in the density profile resulting in a kinetic energy gain which grows faster than the potential energy loss (panel (c) of Fig. 6.4). On the contrary the incompressible insulator maintains a flat density distribution and its energy stays constant.

To better characterize the two solutions we access the coexistence region at zero-bias following both solutions on the two sides of the Mott transition. In Fig. 6.5 we show the hysteresis loop of the orbital polarization across the Mott transition. In this plot we demonstrates that the metallic solution breaks off for $U > U_{c2}$ with a finite jump in the orbital polarization (dashed line in Fig. 6.5). We can understand this behavior computing the effective crystal field splitting, which we extract from the zero frequency extrapolation of the real part of the self-energy

$$\Delta_{eff} = \Delta + \mathrm{Re}\Sigma_{22}(0) - \mathrm{Re}\Sigma_{11}(0). \tag{6.11}$$

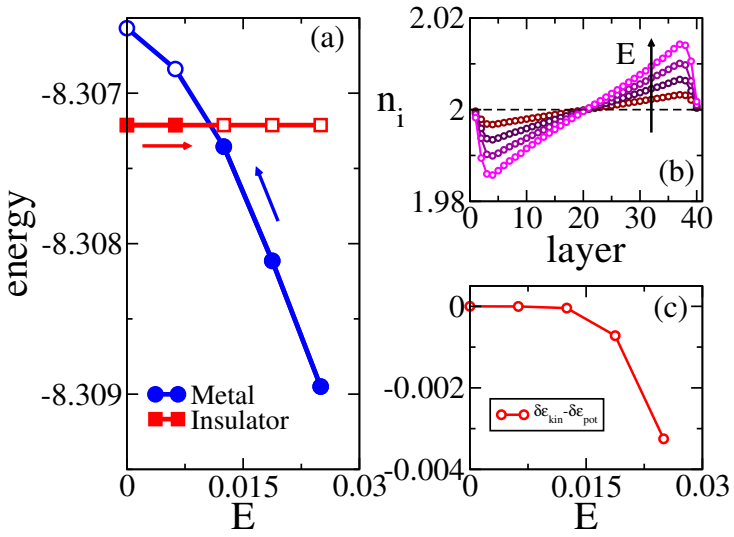

Fig. 6.4: Metal-insulator coexistence as a function of the electric-field. (a) Energy of the metallic (blue circles) and insulating (red squares) solution as a function of the applied electric-field. Filled/open symbols represent stable and metastable solutions respectively. Blue/red arrows indicate solutions obtained respectively decreasing and increasing the field. (b) Density profile for the metallic solutions for electric-fields from 0.025 to 0.00625. The vertical arrow indicate the direction of increasing field. (c) Difference between the kinetic energy gain and the potential energy loss $\delta\epsilon_{\rm kin} - \delta\epsilon_{\rm pot}$, where $\delta\epsilon_{\rm kin/pot}(E) = \left[\epsilon_{\rm kin/pot}(E) - \epsilon_{\rm kin/pot}(0)\right]/|\epsilon(0)|$ being $\epsilon(0)$ the total internal energy at zero field.

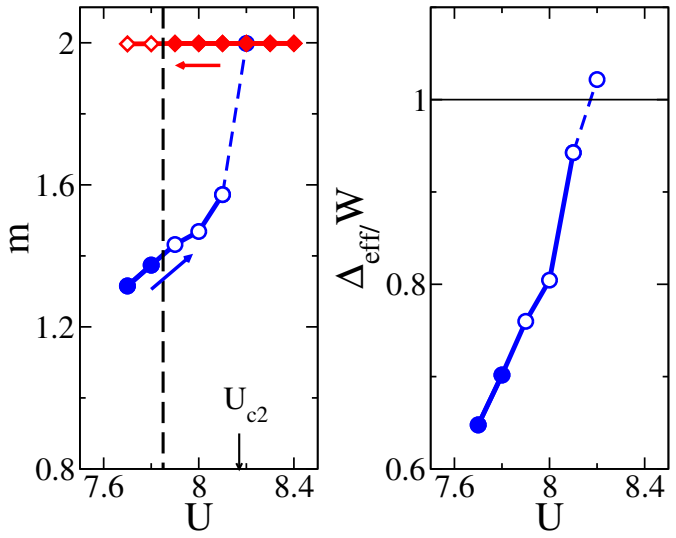

Fig. 6.5: Metal-insulator coexistence as a function of U at zero bias. Left: Hysteresis loop of the orbital polarization averaged over all the layers. Filled/open symbols represent stable and metastable solutions respectively. The vertical dashed line indicates the critical value of U for the first order Mott-transition. Blue/red arrows indicate solutions obtained respectively increasing and decreasing the interaction. Blue dashed line indicate a finite jump of the orbital polarization occurring for $U = U_{c2}$ indicated by the black arrow. Right: Effective crystal field splitting defined in Eq. 6.11 averaged over all the layers. The dots/lines codes are guide to the eyes to compare the results with the left panel.

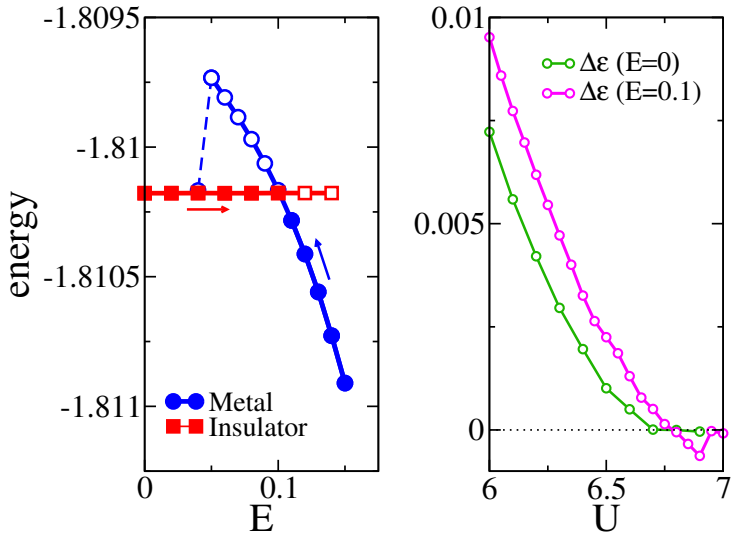

Fig. 6.6: Metal-insulator coexistence as a function of the electric-field and interaction for the single-band Hubbard model. Left: Energy of the metallic (blue circles) and insulating (red squares) solution as a function of the applied electric-field for $U = 6.8$. Filled/open symbols represent stable and metastable solutions respectively. Blue/red arrows indicate solutions obtained respectively decreasing and increasing the field. Right: Energy difference between the insulating and metallic solutions $\Delta\epsilon = E_{ins} - E_{met}$ at zero and finite electric-field, obtained decreasing and increasing the interaction U respectively. The continuous transition at $E = 0$ becomes first-order at finite field.

As displayed in Fig. 6.5 (b) the finite jump in the orbital polarization is determined by the effective crystal field exceeding the bandwidth. The continuous growth of the effective crystal field compared to the finite jump of the polarization is a clear demonstration of the non-trivial role of the dynamical correlations which modify the Lifshitz picture given by the Hartree-Fock approximation. In fact, due to electronic correlations, the metallic solution can not be adiabatically continued to the insulating one.

This shows that the field induced metal shown in Fig. 6.3 is the result of a non-perturbative modification of the Mott insulator electronic properties. Therefore, the field-driven insulator-to-metal transition observed in this model represents an example of a novel breakdown which goes beyond the Zener tunnel mechanism.

6.5 Resistive switch VS Zener breakdown

In order to appreciate the differences between this resistive transition and the standard tunneling mechanism, we compare the above results with those obtained for the single-band half-filled Hubbard model in the same slab geometry and with the same voltage drop. Also in the case of the single-band Hubbard model we can retrieve a first-order insulator-to-metal transition driven by the electric field. Indeed, if we start at zero bias from the Mott insulating phase at $U > U_c \simeq 6.70$ and increase ΔV, we find that the applied bias first pushes the system into a metal-insulator coexistence region and eventually drives

the first order transition above a given threshold ΔV_{th}. In other words, the accidental continuous Mott transition in the single-band model at zero-temperature [115] turns first order in the presence of a bias, as it also happens at any finite temperature. These facts are shown in Fig. 6.6 where a coexistence region can be observed either in the electric field and correlation driven transition at finite bias.

We now compare these results to the two-bands case. In Fig. 6.7(a) we plot E_{th} as a function of U for the two-bands (TB) and one-band (OB) cases, where both quantities are measured in units of the the critical U_c in the absence of the external bias. In both models the threshold field is obviously an increasing function of the interaction strength; however we observe a completely different both quantitative and qualitative behavior. In our TB case the threshold bias is substantially smaller and it increases with a small positive curvature. On the contrary, the OB model displays much larger absolute values of E_{th} and a sub-linear behavior, which signals a fast increase of the threshold field as the gap grows larger. This sub-linear increase resembles closely the behavior of the critical chemical potential μ_c required to dope the Mott insulator in bulk systems [121], which is well described by the critical behavior $\mu_c \sim (U - U_c)^{1/2}$ that we can reproduce by means of the Gutzwiller variational ansatz (see Appendix A.4). Panel (b) of Fig. 6.7 shows that this is not a mere coincidence. In fact, plotting the deviation of the local density $\delta_i = n_i - \langle n \rangle$ with respect to half-filling as a function of the layer index i and for $\Delta V > \Delta V_{th}$, we observe that in the OB case the transition is driven by a substantial doping of the Mott insulator, of holes on one side of the slab and electrons on the other, with an average doping of the order of 5% the total density. This evidently requires a bias that must typically exceed the Mott gap except very close to U_c. On the contrary, in the TB model δ_i is always very small ($\sim 0.2\%$ of the total density) and a tiny density gradient is already sufficient to drive the resistive transition.

We believe that the distinct differences between OB and TB models entail different scales that control the bias-driven insulator-metal transition. Specifically, we argue that in the TB model the critical field is determined by the energy difference between the coexisting solutions, whereas in the standard OB model the threshold bias is governed by the size of insulating gap. This is not only just a quantitative difference, but it reflects two different bias-induced metallic states. In order to highlight this point we show in Fig. 6.8 the intensity plots of the layer dependent spectral functions for the same parameters of the field-induced metals in Fig. 6.7. In the OB case (bottom panels) we note that the metallic solution is characterized by a rigid tilting of the gapped insulating spectral functions. This leads to a substantial redistribution of the spectral weight. In particular, the boundaries are characterized by a sizable spectral weight at the Fermi level. On the contrary in a large bulk region of the slab the gapped spectral functions are characterized by a tiny evanescent weight at the Fermi level. This is better appreciated in the right panel showing two spectral functions for two representative layers respectively in the bulk and close to the boundaries. Such a behavior is consistent with the charge redistribution of Fig. 6.7 and not different from what we would expect in a conventional band insulator in the presence of a uniform electric field that causes a constant gradient of valence and conduction bands, here lower and upper Hubbard bands. We therefore conclude that the

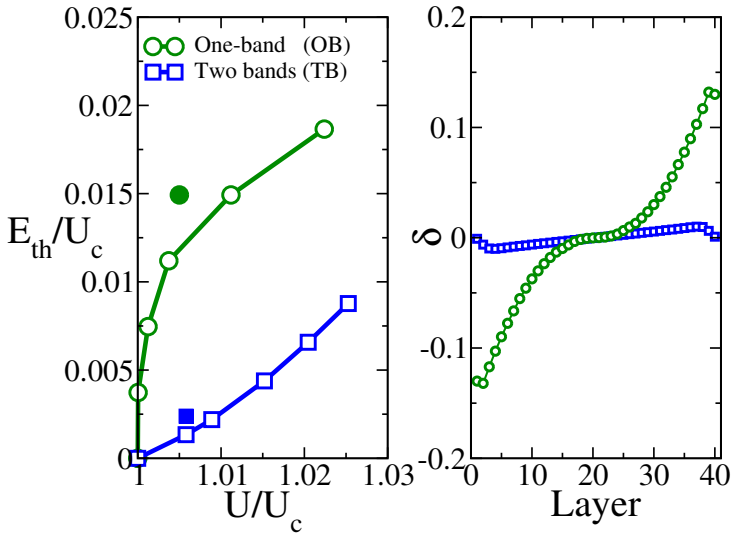

Fig. 6.7: Comparison between the two-bands (TB) and one-band (OB) models: Threshold fields and density profiles. Left: Threshold fields for the TB (blue squares) and OB (green circles) models as a function of the interactions U. Both interaction and threshold fields are measured with respect to the critical interaction for the zero-bias Mott transition. Filled square and circle indicate the biased-interaction values considered in the right panel. Right: Doping profiles for two representative bias-induced metals. Blues squares/Green circles indicate TB/OB model.

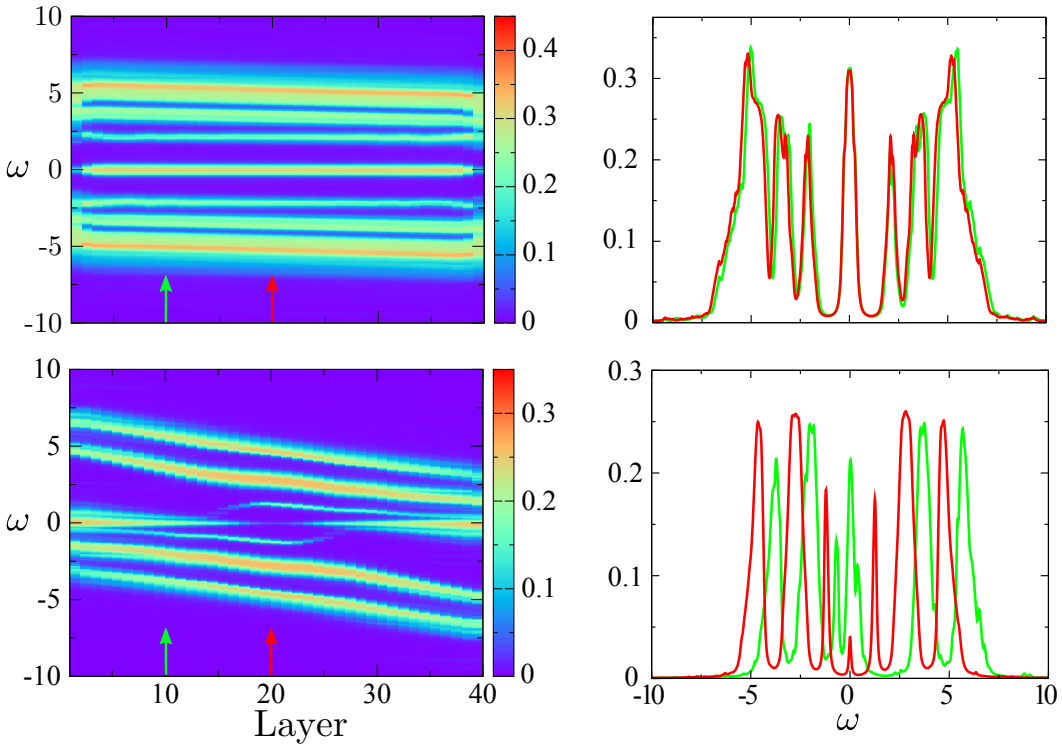

Fig. 6.8: Comparison between the two-bands (TB) and one-band (OB) models: Spectral properties. Left panels: Layer resolved local density of states for the TB (top) and OB (bottom) models. Right panels: Two representative spectral function for two layers indicated by the arrows in the left panels for the TB (top) and OB (bottom) models.

bias-induced metal is consistent with Zener's picture: the electric breakdown is driven by charge tunneling across the Mott gap from the region with negative doping to the region with positive one.

The behavior of the TB model is instead completely different. The insulator-to-metal transition leads to essentially uniform electronic properties, highlighted by the nearly flat dispersion of the spectral function in the top panel of Fig. 6.8 and by the well pronounced quasi-particle features at the Fermi level resulting from the gap collapse. Therefore the metalization does not require promoting carriers across the gap, hence that the dielectric breakdown has nothing to do with the Zener breakdown.

6.6 Discussion and conclusions

In the previous sections we studied the effects of an applied electric-field on the electronic properties described by the model 6.1. The model represents a simple extension of the standard single band Hubbard model with the inclusion of an additional orbital degree of freedom and a crystal field lifting the degeneracy. We have seen that this simple extension has dramatic consequences on the physics described by the model which, as a matter of fact, becomes prone to an electric-field driven resistive transition intrinsically different from the one described by standard Zener tunneling. As shown by Figs. 6.4-6.5 the resistive transition is strongly connected to the presence of a metal-insulator coexistence region. Therefore, one may wonder what are the differences between the TB and OB models: In fact, both TB and OB models display metal-insulator coexistence across the Mott transition, respectively at zero and finite temperature/finite bias.

We relate such difference to the fact that in the TB case the metallic solution is intrinsically different from the insulating one, while in the OB model the metastable metal is still quite close to the insulator. Indeed, the metastable metal in the OB model displays a preformed gap and a tiny and narrow intra-gap quasi-particle peak involving only a low fraction of carriers. A few percent doping is already sufficient to shift the chemical potential from mid-gap to one Hubbard sideband. However, we showed in Figs. 6.7-6.8 that this implies a strong redistribution of carriers throughout the slab with well defined metallic regions appearing only at the boundaries. Thus the breakdown scenario is that of a Zener-like tunneling of carriers from the hole- to the electron-doped region, with a threshold field of the order of the gap except right at the Mott transition. Despite the fact that the above calculations are carried out at zero temperature where the metal-insulator coexistence appears only at finite bias, we expect that a similar scenario holds at finite temperature too. In fact, also in this case a finite doping of the metastable metal would result in a shift of the chemical potential from mid-gap to one Hubbard band, with the result that a substantial charge redistribution similar to the one showed in Fig. 6.7 is expected.

On the contrary, the metastable metal in the TB model is completely disconnected from the insulating solution and is characterized by the complete overlap between the two orbital spectral functions (see Fig. 6.2). In this case the doping of the metal involves mainly an inter-orbital redistribution of the spectral weight and does not require the shift

of the quasi-particle peak from mid-gap to the preformed high-energy bands. Therefore, the applied bias determines an almost homogeneous density gradient with an average doping of less than 0.2 % the total density is already sufficient to drive the transition (see Fig. 6.4).

The aim of the above investigation was to understand the basic mechanisms leading to a substantial modification of the electronic properties in Mott insulators driven by an external electric-field. This led us to individuate in a simple model the distinctive features of a new kind of resistive transition which is profoundly different from what observed in the standard Hubbard-like idealization of a Mott insulator. Although the above results are obtained in a very specific model they might have a greater validity since the model entails common features of a variety of correlated materials. These results have a direct implication in the description of the breakdown mechanism in Mott insulators and call for true non-equilibrium investigations in order to fully clarify the resulting scenario.

Chapter 7

Summary and perspectives

In this thesis we studied few examples of non-equilibrium physics in correlated systems. As briefly reviewed in Chap. 2, this comprises a large spectrum of intriguing phenomena ranging from non-trivial dynamics in cold atomic systems to photo- or field- induced transitions in real correlated materials. Here we focused on paradigmatic examples concerning the dynamical phase transitions after an ultrafast excitation and the transport properties of correlated materials far beyond the linear regime.

In the first case we investigated the possibility to drive a phase transition following a sudden excitation of the system (quantum quench). This is an important issue both from the experimental and theoretical points of view. Indeed, several examples of phase transition induced by an ultrafast excitation are known [14, 15]. On the other hand, the dynamics across a phase transition is associated to the possibility of reaching stable ordered phases without following conventional thermal pathways, an issue that poses several fundamental theoretical questions. In this context, we highlighted in Chap. 4 a link between the dynamical phase transitions in an isolated system and specific features in the many-body spectrum. In particular, this is based on the hypothesis that, in a many-body model undergoing a quantum phase transition that survives up to a critical temperature, symmetric and non-symmetric eigenstates do not overlap in energy, being separated by a *broken symmetry edge* E_*. In such a situation, starting from an initial state with finite order parameter the dynamical restoration of symmetry is ruled by the fact that the injected energy pushes the system above such threshold.

We explicitly checked this hypothesis in the case of the quench dynamics in the fully connected Ising model following a sudden change of the transverse field. We further exploited the idea of the broken symmetry edge to access symmetry broken states which exist in the high energy part of a many body spectrum and hence are invisible in thermodynamics. In particular we showed the existence of non-equilibrium superconducting states in the high-energy spectrum of the repulsive Hubbard model.

These two examples show a basic mechanism which rule the restoration (or the formation) of an ordered state following a sudden excitation in simple models. A deeper understanding of the mechanisms leading to dynamical phase transitions in more complex systems and more realistic excitation protocols is required to achieve a thoroughly

description of photo-induced transition in real systems. In this respect we emphasize the important role of the investigations of the dynamics across phase transitions characterized by the competition of different phases [65].

The second phenomenon we considered is the non-linear transport induced by strong electric fields in correlated systems. The comprehension of the transport properties of correlated systems beyond the linear regime is of extreme importance for the possible applications of these materials in electronic devices.

In Chap. 5 we analyzed the non-equilibrium transport properties of a finite-size correlated system coupled to two external sources. We described the correlated system within the framework of the single band Hubbard model and used the time-dependent Gutzwiller approximation to study its dynamics. In the absence of bias we investigated the dynamics arising by the sudden formation of a metal/correlated system interface. When a finite bias is induced across the sample we addressed the formation of non-equilibrium stationary states characterized by a finite current. We described the non-linear current-bias characteristics both in metallic and insulating phases.

In the metallic case we pointed out a universal linear behavior with respect to the interaction strength. Thus, we analyzed the appearance of non-linear effects in large electric-fields showing that the electron-electron interaction strongly renormalizes the bias range for which a linear regime is observed. Eventually in the Mott insulating regime the linear behavior disappears. In this case the stationary currents signal the breakdown of the Mott insulating phase and display an exponential activated behavior which is consistent with the Landau-Zener tunneling mechanism [27]. This scenario is supported by analytical calculations in the stationary regime.

The breakdown mechanism of a Mott insulator is actually a pivotal phenomenon for realistic technological applications of correlated materials [28]. Motivated by the experimental results pointing out the existence of different behaviors, in Chap. 6 we investigated a dielectric breakdown mechanism which is different from the Landau-Zener one. To this extent we introduced a simple model for a generic correlated material comprising two orbital degrees of freedom. This extension of the standard single band description is naturally motivated by the multi-orbital nature of most correlated materials. Studying the electronic properties of the model in a static electric field by means of DMFT we demonstrated the occurrence of a sharp field induced insulator-to-metal transition. We associated this occurrence to a large region across the Mott transition in which both the metallic and insulating solutions coexist. In particular, starting from the insulating side of the transition we showed that the electric field is able to stabilize a gap-collapsed metal thanks to a tiny density gradient induced across the sample. Comparing the results with that of the single band model we showed that this occurrence represents a novel mechanism of electric breakdown which has nothing to do with the standard Zener one.

These results may open a new scenario for the description of the various breakdown or resistive transitions observed in Mott insulators [30]. In this respect a generalization to the true non equilibrium case of the above results is needed to fully clarify the mechanisms leading to the resistive transition in Mott insulator. Having in mind the resistive switch experiments in narrow-gap Mott insulators and their interpretation [26, 38] , we may

envisage a situation in which the insulator-to-metal transition is triggered by an electric-field pulse. In fact, since in our results the transition is driven by a density gradient across the sample, we may expect that an electric field pulse would induce a fast distortion of the electronic cloud which pushes the system into the metastable metallic state. In such a situation, it is likely that a finite current is established, with the density relaxing back to an almost flat distribution. In this case, the strength and duration of the pulse may be crucial quantities for determining both the appearance and the stability of such induced state. As outlined in Ref. [38] in an extended system this process may be related to an avalanche formation of conducting channels triggered by the transition of small portions of the entire sample. In this regard the insulator-to-metal transition described in Chap. 6 would represent the possible seed for the formation of such conducting channels.

We conclude stressing the fact that further proceeding along the research directions discussed in this thesis necessarily requires a methodological improvement in treating correlated systems in non-equilibrium conditions. In particular, the possibility to treat complex models with several degrees of freedom is a fundamental step towards the description of non-trivial non-equilibrium phenomena in strongly correlated materials.

Part III

Appendix

Appendix A

The Gutzwiller Approximation

Since its introduction in the sixties [122, 123] the Gutzwiller Variational Method has proven to be a fundamental non perturbative method for the description of strong correlation effects. In particular, it represented one of the first methods able to describe a correlation driven metal-insulator transition in a system expected to be metallic due to partially filled conduction band.

The idea that the electron-electron correlations could give rise to an insulating state in a system with an half filled band was put forward by Mott [113, 114]. He firstly realized that the metal-insulator transition can be the result of the competition between the kinetic energy, which tends to delocalize electrons throughout the lattice, and the correlation which significantly constrains the electronic motion. The Hubbard model represents the simplest lattice model comprising such competition. For convenience we repeat here the Hamiltonian which we already used in Chaps. 4, 5 and 6

$$H = -t \sum_{\langle ij \rangle \sigma} \left(c^{\dagger}_{i\sigma} c_{j\sigma} + H.c. \right) - \mu \sum_{i\sigma} c^{\dagger}_{i\sigma} c_{i\sigma} + U \sum_{i} n_{i\uparrow} n_{i\downarrow}, \tag{A.1}$$

where $c^{\dagger}_{i\sigma}(c_{i\sigma})$ are creation(annihilation) operators for an electron of spin σ on the site i and $n_{i\sigma} = c^{\dagger}_{i\sigma} c_{i\sigma}$ is the number operator; t is the hopping amplitude, μ is the chemical potential and U is the on-site repulsion.

The competition between the kinetic and interaction terms is the origin of the non trivial properties of the model. In particular, it is easy to realize that in the half filled case the model describes a metal-insulator transition as a function of the parameter U/t. Indeed, in the not-interacting limit $U/t = 0$ the model describes a free metal with half filled band, while in the limit $U/t \gg 1$ due to the large energy cost in creating double occupancies the charges get localized on each site. Eventually, in the atomic limit $U/t \to \infty$ no double occupancy is allowed and all the configurations with one electron per site become degenerate. In this limit the system is an insulator due to the complete suppression of the electron mobility.

Away from these limits, an exact solution of the model (A.1) is not feasible apart from the one dimensional case [124]. Through the years a huge effort has been devoted to the development of a general theoretical framework for the description of the physical

properties derived from strong correlations. A major breakthrough in this direction is represented by the development of the Dynamical Mean Field Theory (DMFT) [115], which provided a tool for exactly treat systems with competing energy scales at the cost of freezing all the spatial fluctuations.

Nevertheless, many years before the development of DMFT Brinkman and Rice [125] showed the possibility to describe a metal-insulator transition at finite value of U/t by means of a variational wave-function previously introduced by M. Gutzwiller [122, 123] for studying correlation effects in narrow bands. In particular, starting from a not-interacting metallic wave-function $|\Psi_0\rangle$ in which the correlation effect is taken into account by means of a projector controlling the number of doubly occupied sites

$$|\Psi_G\rangle = \prod_i (1 - g n_{i\uparrow} n_{i\downarrow}) |\Psi_0\rangle, \tag{A.2}$$

the disappearance of the metallic phase is signaled by a diverging effective mass and a vanishing spectral weight for the quasi-particles at the Fermi-level. The method gives a poor description of the insulating state which is represented by a collection of single electrons frozen on each lattice sites. Although such a poor description, the method provides in its simple formulation a clear picture of the correlation effects, in good agreement with the later characterization given by DMFT [126, 127].

The success of the Gutzwiller method motivated its further extensions and applications, so that nowadays it represents a flexible tool complementary to the DMFT approach. In particular, it represents a valuable option in the cases in which DMFT becomes extremely demanding from a numerical point of view. This aspect is not only useful for the description of more complex models which extend the model (A.1) with the inclusion of an increasing number of degrees of freedom (*i.e.* orbital degeneracy [128, 129]) or more realistic electronic structure descriptions obtained from *ab initio* methods such as Density Functional Theory (DFT) [130, 131], but is crucial as soon as the focus is set onto the physical properties in non-equilibrium situations. Indeed, in this case the non-equilibrium extension of DMFT [132] has not yet reached the development level of its equilibrium counterpart and still suffers from some practical limitations mainly related to the lack of efficient solvers, so that a simple and flexible approach becomes extremely desirable. In this context, the Gutzwiller method represents a valuable option. Indeed its time-dependent extension, although suffering from some intrinsic drawbacks arising from its essential mean-field nature, has a very simple implementation and shows, as in the equilibrium case, a remarkable agreement with more rigorous results obtained within DMFT. This is not only limited to the simplest applications such as the problem of quantum quenches in the Hubbard model [48, 49]. In fact, the method has been shown to give results in agreement with DMFT also in more complex situations, as the the dynamics in the presence of an antiferromagnetic order parameter [51, 59]. Moreover, it has been successfully applied also to the investigate the dynamics in the superconducting case [133] (see Chap. 4) and multi-orbitals models [65], which are almost unexplored fields within the non-equilibrium DMFT approach.

In the next section we shall briefly review the Gutzwiller variational method referring the reader to existing literature for further details [97]. We will consider a general

extension to the multi-orbital case of the single-band Hubbard Hamiltonian

$$\mathcal{H} = \sum_{i,j} \sum_{\alpha,\beta} \left(t_{i,j}^{\alpha,\beta} c_{i,\alpha}^{\dagger} c_{j,\beta} + H.c. \right) + \sum_{i} H_i, \tag{A.3}$$

where $c_{i,\alpha}^{\dagger}$ is a creation operator for an electron in the site i in the state labeled by the index α, which we assume to include orbital and spin degrees of freedom. H_i is a generic local interaction term.

A.1 The Gutzwiller Variational Method

The Gutzwiller wave-function and approximation

We consider a generalization of the original variational ansatz (A.2) introducing a series of projectors $\mathcal{P}_i$ acting on the local Hilbert space at site i and a one-body wave function $|\Psi_0\rangle$

$$|\Psi_G\rangle = \prod_i \mathcal{P}_i |\Psi_0\rangle. \tag{A.4}$$

The goal of the variational approach is therefore to find, within the class of wave-functions identified by (A.4), the best approximation to true ground state minimizing the variational energy

$$E_G = \frac{\langle \Psi_G | \mathcal{H} | \Psi_G \rangle}{\langle \Psi_G | \Psi_G \rangle}. \tag{A.5}$$

The computation of the variational energy is not feasible, and in general it can be carried out exactly only resorting to an explicit numerical computation in a finite-size lattices. However, it turns out that the analytical computation becomes possible in lattices in the limit of infinite coordination number $z \to \infty$, once the following constraints on the variational ansatz are introduced

$$\langle \Psi_0 | \mathcal{P}_i^{\dagger} \mathcal{P}_i | \Psi_0 \rangle = 1 \tag{A.6}$$

$$\langle \Psi_0 | \mathcal{P}_i^{\dagger} \mathcal{P}_i \, \mathcal{C}_i | \Psi_0 \rangle = \langle \Psi_0 | \mathcal{C}_i | \Psi_0 \rangle, \tag{A.7}$$

being $\mathcal{C}_i$ the local single particle density matrix. Constraints (A.6-A.7) implies a great simplification in the calculations in the limit $z \to \infty$ [1] thanks to two facts. Firstly, we note that selecting two fermionic operators from $\mathcal{P}_i^{\dagger} \mathcal{P}_i$ and contract with two any other fermionic operators, the average of the remaining part over the Slater determinant identically vanishes. Explicitly

$$\begin{aligned} \langle \Psi_0 | \mathcal{P}_i^{\dagger} \mathcal{P}_i \, \mathcal{C}_i | \Psi_0 \rangle &= \langle \Psi_0 | \mathcal{P}_i^{\dagger} \mathcal{P}_i | \Psi_0 \rangle \langle \Psi_0 | \mathcal{C}_i | \Psi_0 \rangle + \langle \Psi_0 |_i \overbrace{(\mathcal{P}_i^{\dagger} \underbrace{\mathcal{P}_i}) \mathcal{C}_i}^{} | \Psi_0 \rangle_c \\ &= \langle \Psi_0 | \mathcal{C}_i | \Psi_0 \rangle, \end{aligned} \tag{A.8}$$

[1] In order to have a meaningful limit the hopping must be rescaled as $t \to \frac{t}{\sqrt{z}}$.

which implies that the last term on the r.s.h. in the first line of Eq. A.8 containing all the contractions involving the extraction of two fermionic lines from $\mathcal{P}_i^\dagger \mathcal{P}_i$ vanishes. Moreover, due to the fact that the hopping operator $\langle c_i^\dagger c_j \rangle$ vanishes for $z \to \infty$ as $z^{-l/2}$ [134], being l the Manhattan distance between the sites i and j, each contraction involving the extraction of $2n > 2$ fermionic operators from the operator $\mathcal{P}_i^\dagger \mathcal{P}_i$ and their contraction with the corresponding operators at site j scales as z^{-l} and therefore vanishes in the limit of infinite coordination.

The above facts imply that the wave-function is normalized and allow to obtain an explicit expressions of the expectation values of any given local operator $\mathcal{O}_i$

$$\langle \Psi_G | \mathcal{O}_i | \Psi_G \rangle = \langle \Psi_0 | \mathcal{P}_i^\dagger \mathcal{O}_i \mathcal{P}_i \, | \Psi_0 \rangle. \tag{A.9}$$

Similarly, the expectation value of the hopping operator reads

$$\langle \Psi_G | c_{i\alpha}^\dagger c_{j\beta} | \Psi_G \rangle = \langle \Psi_0 | \mathcal{P}_i^\dagger c_{i\alpha}^\dagger \mathcal{P}_i \, \mathcal{P}_j^\dagger c_{j\beta} \mathcal{P}_j \, | \Psi_0 \rangle, \tag{A.10}$$

which after contracting the operators at sites i and j with a single fermionic line becomes

$$\langle \Psi_0 | \mathcal{P}_i^\dagger c_{i\alpha}^\dagger \mathcal{P}_i \, \mathcal{P}_j^\dagger c_{j\beta} \mathcal{P}_j \, | \Psi_0 \rangle = \sum_{\gamma,\delta} R_{i,\alpha\gamma}^* R_{j,\beta\delta} \langle \Psi_0 | c_{i\gamma}^\dagger c_{j\delta} | \Psi_0 \rangle. \tag{A.11}$$

The matrices $\hat{R}_i$ contain the averages over the Slater determinant of the remaining operator after the contraction is carried-out and are defined through

$$\langle \Psi_0 | \mathcal{P}_i^\dagger c_{i\alpha}^\dagger \mathcal{P}_i \, c_{j\beta} | \Psi_0 \rangle = \sum_{\gamma} R_{i\alpha\gamma}^* \langle \Psi_0 | c_{i\gamma}^\dagger c_{j\beta} | \Psi_0 \rangle. \tag{A.12}$$

Using the matrices $\hat{R}_i$ we define new one-body Hamiltonian $\mathcal{H}_\star$ from the not-interacting part of the original Hamiltonian with renormalized hopping amplitudes

$$\mathcal{H}_\star = \sum_{ij} \sum_{\alpha\beta} t_{\star\, i,j}^{\alpha,\beta} c_{i,\alpha}^\dagger c_{j,\beta} \qquad \text{with} \qquad \hat{t}_{\star\, i,j} = \hat{R}_i^\dagger \hat{t}_{i,j} \hat{R}_j. \tag{A.13}$$

Thus, the search for the best variational estimation of the ground state energy reduces to the minimization of the following functional

$$E_G \left[\mathcal{P}, |\Psi_0\rangle \right] = \langle \Psi_0 | \mathcal{H}_\star | \Psi_0 \rangle + \sum_i \langle \Psi_0 | \mathcal{P}_i^\dagger H_i \, \mathcal{P}_i \, | \Psi_0 \rangle \tag{A.14}$$

with respect of the Slater determinant and local projectors, subjected to the constraints (A.6-A.7). The expression (A.14) is exact only in the $z \to \infty$ limit and its use in lattices with finite coordination number is called the *Gutzwiller approximation*.

At fixed matrices Gutzwiller operators $\mathcal{P}_i(t)$, the Slater determinant minimizing the energy (A.14) is clearly the ground state of the Hamiltonian $\mathcal{H}_\star[\hat{\Phi}]$. While the latter has a rigorous meaning only for its ground state energy it is common to interpret its single-particle excitation as the coherent Landau quasi-particles with a renormalized spectral weight [135]. For instance, in the single band case the spectral weight is given by

$$Z = |R|^2 \tag{A.15}$$

and vanishes as $1 + U/8\langle \epsilon_0 \rangle$, being $\langle \epsilon_0 \rangle < 0$ the average value of the hopping computed on the Fermi sea. Therefore the Birkman-Rice metal-insulator transition is retrieved for $U = U_c = -8\langle \epsilon_0 \rangle$.

Time-dependent Gutzwiller (TDG) approximation

We now extend the Gutzwiller approximation to the time-dependent case. Let us assume that at $t = 0$ the system is described by the many-body wave-function $|\Psi(0)\rangle$ and focus on its time evolution under the effect of a time-dependent Hamiltonian $\mathcal{H}(t)$. The exact quantum dynamics of the state $|\Psi(t)\rangle$ is set by the time dependent Schrödinger equation

$$i\partial_t|\Psi(t)\rangle = \mathcal{H}(t)|\Psi(t)\rangle. \tag{A.16}$$

On the same spirit of the ground state Gutzwiller approximation, we look for the best approximation to the exact time evolved state $|\Psi(t)\rangle$ within a class of time-dependent wave-functions of the type (A.4). To this extent, we shall assume that both the Gutzwiller projectors and the Slater determinant depend explicitly on time, namely

$$|\Psi(t)\rangle \simeq |\Psi_G(t)\rangle = \prod_i \mathcal{P}_i(t)|\Psi_0(t)\rangle, \tag{A.17}$$

and impose that $|\Psi_G\rangle$ is as close as possible to the solution of the Schrödinger equation. This is done introducing the action functional

$$\mathcal{S}\Big[|\Psi_G\rangle\Big] = \int_0^t d\tau \langle\Psi_G(\tau)|i\partial_\tau - \mathcal{H}(\tau)|\Psi_G(\tau)\rangle = \int_0^t d\tau \mathcal{L}(\tau) \tag{A.18}$$

and requiring its stationarity with respect to the variational wave-function

$$\frac{\delta\mathcal{S}\Big[|\Psi_G\rangle\Big]}{\delta\langle\Psi_G|} = 0. \tag{A.19}$$

The computation of the action (A.18) on the time-dependent variational wave-function (A.17) is a non-trivial task as difficult as the calculation of the equilibrium energy functional. As in the equilibrium case, it turns out that this can be performed in the limit $z \to \infty$ if the constraints equivalent to (A.6-A.7) are satisfied at any time t

$$\langle\Psi_0(t)|\mathcal{P}_i^\dagger(t)\mathcal{P}_i(t)|\Psi_0(t)\rangle = 1 \tag{A.20}$$

$$\langle\Psi_0(t)|\mathcal{P}_i^\dagger(t)\mathcal{P}_i(t)\mathcal{C}_i(t)|\Psi_0(t)\rangle = \langle\Psi_0(t)|\mathcal{C}_i(t)|\Psi_0(t)\rangle. \tag{A.21}$$

Under these conditions the Lagrangian $\mathcal{L}(t)$ which define the action (A.18) reads [97]

$$\mathcal{L}(t) = i\sum_i \langle\Psi_0(t)|\mathcal{P}_i^\dagger(t)\dot{\mathcal{P}}_i(t)|\Psi_0(t)\rangle + i\langle\Psi_0(t)|\dot{\Psi}_0(t)\rangle - E(t), \tag{A.22}$$

where $E(t)$ is the expectation value of the Hamiltonian which has the same expression as in Eq. (A.14)

$$E(t) = \langle\Psi_0(t)|\mathcal{H}_\star(t)|\Psi_0(t)\rangle + \sum_i \langle\Psi_0(t)|\mathcal{P}_i^\dagger(t)H_i\,\mathcal{P}_i(t)|\Psi_0(t)\rangle. \tag{A.23}$$

The renormalized hopping Hamiltonian $\mathcal{H}_\star(t)$ is defined as in the equilibrium case by Eq. (A.13) and it acquires a time-dependence through the matrices $\hat{R}_i(t)$.

Explicit representation of the Gutzwiller projectors

In order to further proceed with the search of the saddle point of the action defined by the Lagrangian (Eq. A.22) we shall introduce a specific representation of the Gutzwiller projectors. As outlined in Ref. [98] it is convenient to introduce the so called natural basis operators $d^\dagger_{ia}$ and d_{ia}, namely a set of creation and annihilation operators for which the one-particle density matrix computed on the Slater determinant is diagonal

$$\langle \Psi_0(t)|d^\dagger_{ia}d_{ib}|\Psi_0(t)\rangle = \delta_{ab}n^0_{ia}(t). \tag{A.24}$$

We assume that the natural basis operators are related to the original fermionic operator by a unitary transformation and we introduce Fock states on this basis

$$|i;n\rangle = \prod_a \left(d^\dagger_{ia}\right)^{n_a} \tag{A.25}$$

such that the matrix of the local occupation probability is diagonal by definition

$$\begin{aligned} P^0_{i(n,m)}(t) &= \langle \Psi_0(t)|i;m\rangle\langle i;n|\Psi_0(t)\rangle = \delta_{n,m}\prod_a \left(n^0_{ia}\right)^{n_a}\left(1-n^0_{ia}\right)^{(1-n_a)} = \\ &= \delta_{nm}P^0_{in}(t). \end{aligned} \tag{A.26}$$

With these definitions, it turns out to be particularly useful to parameterize of the Gutzwiller projectors in a mixed original/natural basis representation [98]

$$\mathcal{P}_i(t) = \sum_{\Gamma,n} \frac{\Phi_{i;\Gamma n}(t)}{\sqrt{P^0_{in}(t)}}|i;\Gamma\rangle\langle i;n|. \tag{A.27}$$

where the variational parameters $\Phi_{i;\Gamma n}(t)$ define a local variational matrix $\hat{\Phi}_i(t)$ and where $|i;\Gamma\rangle$ are basis set in the terms of the original operators $c^\dagger_{ia}$. This representation actually corresponds to the rotationally invariant slave boson mean-field introduced at equilibrium in Ref. [136].

Such parameterization introduces a great simplification in the expression of the expectation values in the Lagrangian (A.22) which can then be readily used for practical calculations. Indeed, introducing the following matrix representation for the creation/annihilation operators and for a generic local observable $\mathcal{O}_i$

$$\begin{aligned} \left(\hat{d}_{ia}\right)_{nm} &= \langle i;n|d_{ia}|i;m\rangle \\ \left(\hat{c}_{ia}\right)_{\Gamma\Gamma'} &= \langle i;\Gamma|c_{ia}|i;\Gamma'\rangle \\ \left(\hat{O}_i\right)_{\Gamma\Gamma'} &= \langle i;\Gamma|\mathcal{O}_i|i;\Gamma'\rangle \end{aligned} \tag{A.28}$$

simple algebra shows that the constraints (A.20-A.21) acquires the form

$$\mathrm{Tr}\left(\hat{\Phi}^\dagger_i(t)\hat{\Phi}_i(t)\right) = 1 \tag{A.29}$$

$$\mathrm{Tr}\left(\hat{\Phi}^\dagger_i(t)\hat{\Phi}_i(t)\hat{d}^\dagger_{ia}\hat{d}_{ia}\right) = \langle \Psi_0(t)|d^\dagger_{ia}d_{ia}|\Psi_0(t)\rangle = n^0_{ia}(t). \tag{A.30}$$

Similarly, the average of any local operator can be expressed solely in terms of the matrices $\hat{\Phi}_i(t)$ without any reference to the Slater determinant

$$\langle\Psi_0(t)|\mathcal{P}_i^\dagger\mathcal{O}_i\mathcal{P}_i\,|\Psi_0(t)\rangle = \mathrm{Tr}\left(\hat{\Phi}_i^\dagger(t)\hat{O}_i\hat{\Phi}_i(t)\right). \tag{A.31}$$

Moreover, expressing the expectation value of the inter-site hopping operator in terms of the natural basis operators we obtain an explicit expression for the hopping renormalization matrices which is suitable for practical calculations. Indeed, we obtain

$$\langle\Psi_0(t)|\mathcal{P}_i^\dagger(t)c_{i\alpha}^\dagger\mathcal{P}_i\,(t)\mathcal{P}_j^\dagger(t)c_{j\beta}\mathcal{P}_j\,(t)|\Psi_0(t)\rangle = \sum_{c,d} R^*_{i,\alpha c}(t)R_{j,\beta d}(t)\langle\Psi_0|d_{ic}^\dagger d_{jd}|\Psi_0\rangle \tag{A.32}$$

with

$$\begin{aligned}\langle\Psi_0(t)|\mathcal{P}_i^\dagger(t)c_{i\alpha}^\dagger\mathcal{P}_i\,(t)d_{ib}|\Psi_0(t)\rangle &= \sum_c R^*_{i\alpha c}(t)\langle\Psi_0(t)|d_{ic}^\dagger d_{ib}|\Psi_0(t)\rangle = \\ &= R^*_{i\alpha b}(t)n^0_{ib}(t),\end{aligned} \tag{A.33}$$

where the last equality follows from (A.24). Inserting the definition (A.27) into the l.h.s. of (A.33) we obtain the explicit expression for the matrices $\hat{R}_i$

$$R^*_{i\alpha b}(t) = \frac{1}{\sqrt{n^0_{ib}(1-n^0_{ib})}}\mathrm{Tr}\left(\hat{\Phi}_i^\dagger(t)\hat{c}_{i\alpha}^\dagger\hat{\Phi}_i(t)\hat{d}_{ib}\right), \tag{A.34}$$

which through the constraint (A.30) can be regarded as a functional of $\hat{\Phi}_i(t)$ alone. Therefore the effective Hamiltonian $\mathcal{H}_\star$ in Eq. (A.23) reads

$$\mathcal{H}_\star\big[\hat{\Phi}(t)\big] = \sum_{ij}\sum_{ab} t_{\star i,j}^{a,b} d_{ia}^\dagger d_{jb} \quad \text{with} \quad t_{\star i,j}^{a,b} = \sum_{\alpha\beta} R^\dagger_{ia\alpha}\big[\hat{\Phi}(t)\big]t_{i,j}^{\alpha\beta}R_{j\beta b}\big[\hat{\Phi}(t)\big]. \tag{A.35}$$

Eventually, inserting the representation (A.27) into Eq. (A.22) we obtain the following expression for the Lagrangian [97]

$$\begin{aligned}\mathcal{L}(t) = i\sum_i \mathrm{Tr}\left(\hat{\Phi}_i^\dagger(t)\frac{\partial\hat{\Phi}_i(t)}{\partial t}\right) - \mathrm{Tr}\left(\hat{\Phi}_i^\dagger(t)\hat{H}_i\hat{\Phi}_i(t)\right) + \\ i\langle\Psi_0(t)|\dot{\Psi}_0(t)\rangle - \langle\Psi_0(t)|\mathcal{H}_\star\big[\hat{\Phi}(t)\big]|\Psi_0(t)\rangle.\end{aligned} \tag{A.36}$$

The best approximation to the real evolving state within the wave-function class defined by (A.17) is then found taking the saddle point of the action whose Lagrangian is defined by (A.36). In particular, we obtain

$$i|\dot{\Psi}_0(t)\rangle = \mathcal{H}_\star\big[\hat{\Phi}(t)\big]|\Psi_0(t)\rangle \tag{A.37}$$

$$\begin{aligned}i\dot{\hat{\Phi}}_i(t) &= \hat{H}_i\hat{\Phi}_i(t) + \langle\Psi_0(t)|\frac{\partial\mathcal{H}_\star}{\partial\hat{\Phi}_i^\dagger}|\Psi_0(t)\rangle \\ &\equiv \widetilde{H}\Big[\Psi_0(t),\hat{\Phi}(t)\Big]\hat{\Phi}_i(t)\end{aligned} \tag{A.38}$$

namely the Slater determinant evolves with a not-interacting Hamiltonian which depends parametrically on the matrices $\hat{\Phi}_i(t)$, which in turns satisfies a non-linear Schrödinger equation whose Hamiltonian depends on both the Slater determinant and all the variational matrices $\hat{\Phi}$. The dynamics (A.37-A.37) has to be solved requiring that the constraints (A.29-A.30) are satisfied at each time t. A great simplification comes from the fact that, as shown in Ref. [97], the dynamics (A.37-A.37) conserves the constraints during the time evolution. Therefore, once they are enforced at initial time $t = 0$ they are automatically satisfied at each time $t > 0$.

The dynamics of the Slater determinant (A.37) can be interpreted to describe the dynamics of the coherent quasi-particles, while the dynamics of the variational matrices (A.38) is associated with the dynamics of the local degrees of freedom and is commonly associated to the dynamics of the incoherent Hubbard bands. The two dynamical evolutions are coupled in a mean-field-like fashion, each degree of freedom providing a time-dependent field for the other one. This aspect represents a great advantage of the present method with respect to standard mean-field techniques, e.g., time-dependent Hartree-Fock.

The stationary limit of Eqs. (A.37-A.37) leads to two non-linear eigenvalue problems corresponding to the saddle point of the equilibrium Gutzwiller functional [97].

A.2 Gutzwiller Approximation with superconducting long-range order

A.2.1 Ground state calculations for the attractive Hubbard model

In this section we show the the details of the application of the Gutzwiller technique to the problem of the dynamics in the presence of a finite superconducting order parameter which is discussed in Sec. 4.4. We start showing the application for equilibrium calculation in the attractive Hubbard model which shows finite superconducting order parameter in its ground state

$$H = -t \sum_{\langle ij \rangle \sigma} \left(c^\dagger_{i\sigma} c_{j\sigma} + H.c. \right) - \mu \sum_{i\sigma} c^\dagger_{i\sigma} c_{i\sigma} - |U| \sum_i n_{i\uparrow} n_{i\downarrow}, \tag{A.39}$$

In order to allow the system to display a finite value of the superconducting order parameter we shall consider BCS-type wave-function for the uncorrelated wave-function in the variational ansatz A.17 For this particular choice the local density matrix computed on the uncorrelated wave-function may be not diagonal

$$\mathcal{C}_i = \begin{pmatrix} c^\dagger_{i\uparrow} c_{i\downarrow} & c^\dagger_{i\uparrow} c^\dagger_{i\downarrow} \\ c_{i\downarrow} c_{i\uparrow} & c_{i\downarrow} c^\dagger_{i\downarrow} \end{pmatrix}, \qquad \text{with} \qquad \langle \Psi_0 | c^\dagger_\uparrow c^\dagger_\downarrow | \Psi_0 \rangle \neq 0. \tag{A.40}$$

As explained in the previous section, we use the mixed-basis representation for the $\hat{\Phi}$ matrix introducing the fermionic creation(annihilation) operators $d^\dagger_{i\sigma}(d_{i\sigma})$ which diagonalize the single particle density matrix. Within this choice the superconducting order

parameter reads

$$\Delta = \langle \Psi | c^\dagger_{i\uparrow} c^\dagger_{i\downarrow} + c_{i\downarrow} c_{i\uparrow} | \Psi \rangle = 2\mathrm{Re}\left(\phi_{02}\phi^*_{22} + \phi_{00}\phi^*_{20}\right). \tag{A.41}$$

Therefore, in order to have $\Delta \neq 0$ we write the generic variational matrix $\hat{\Phi}$ as

$$\hat{\Phi} = \phi_{00}|0\rangle_c\langle 0|_d + \phi_{02}|0\rangle_c\langle 2|_d + \phi_{20}|2\rangle_c\langle 0|_d + \phi_{\uparrow\uparrow}|\uparrow\rangle_c\langle\uparrow|_d + \phi_{\downarrow\downarrow}|\downarrow\rangle_c\langle\downarrow|_d, \tag{A.42}$$

where we explicitly indicate with $|\cdot\rangle_c$ and $|\cdot\rangle_d$ the local basis states in the original and natural basis respectively. In this representation the constraints (A.29-A.30) read

$$\begin{aligned}
\mathrm{Tr}\left(\hat{\Phi}^\dagger_i \hat{\Phi}_i\right) &= 1 && && && \text{(A.43)}\\
\mathrm{Tr}\left(\hat{\Phi}^\dagger_i \hat{\Phi}_i d^\dagger_\sigma d_{\sigma'}\right) &= \langle \Psi_0 | d^\dagger_\sigma d_{\sigma'} | \Psi_0 \rangle = n^0_\sigma \delta_{\sigma,\sigma'} && && && \text{(A.44)}\\
\mathrm{Tr}\left(\hat{\Phi}^\dagger_i \hat{\Phi}_i d^\dagger_\sigma d^\dagger_{\sigma'}\right) &= \langle \Psi_0 | d^\dagger_\sigma d^\dagger_{\sigma'} | \Psi_0 \rangle = 0 && \forall && \sigma, \sigma' && \text{(A.45)}\\
\mathrm{Tr}\left(\hat{\Phi}^\dagger_i \hat{\Phi}_i d_\sigma d_{\sigma'}\right) &= \langle \Psi_0 | d_\sigma d_{\sigma'} | \Psi_0 \rangle = 0 && \forall && \sigma, \sigma'. && \text{(A.46)}
\end{aligned}$$

Following the prescriptions of the previous section we can now write the energy functional introducing suitable Lagrange parameters to enforce constraints A.43-A.46

$$\begin{aligned}
E_{var} =& \langle \Psi_0 | \mathcal{H}_* | \Psi_0 \rangle - |U| \sum_i \mathrm{Tr}\left(\hat{\Phi}^\dagger \hat{n}_{i\uparrow} \hat{n}_{i\downarrow} \hat{\Phi}\right) + \\
&+ \nu \sum_{i\sigma} \left(\langle \Psi_0 | c^\dagger_{i\sigma} c_{i\sigma} | \Psi_0 \rangle - n^0_\sigma \right) + \\
&+ \delta \sum_i \langle \Psi_0 | c^\dagger_{i\uparrow} c^\dagger_{i\downarrow} | \Psi_0 \rangle + H.c. + \\
&+ \lambda \sum_{i\sigma} \mathrm{Tr}\left(\hat{\Phi}^\dagger_i \hat{\Phi}_i \hat{d}^\dagger_{i\uparrow} \hat{d}^\dagger_{i\downarrow}\right) + H.c.
\end{aligned} \tag{A.47}$$

We build the effective Hamiltonian $\mathcal{H}_*$ computing the expectation values of the hopping operators. In the present case we get additional anomalous hopping renormalization matrices $\hat{Q}$, so that the original fermionic operators are replaced by

$$\begin{aligned}
c^\dagger_{i,\sigma} &\rightarrow \sum_{\sigma'} R_{i,\sigma,\sigma'} d^\dagger_{i\sigma'} + Q^*_{i,\sigma,\sigma'} d_{i,\sigma'} && \text{(A.48)}\\
c_{i,\sigma} &\rightarrow \sum_{\sigma'} R^*_{i,\sigma,\sigma'} d_{i\sigma'} + Q_{i,\sigma,\sigma'} d^\dagger_{i,\sigma'}. && \text{(A.49)}
\end{aligned}$$

Explicit expressions reads

$$\begin{aligned}
R_{i,\sigma,\sigma'} &= \frac{\delta_{\sigma,\sigma'}}{\sqrt{n^0_{i,\sigma'}(1 - n^0_{i,\sigma'})}} \mathrm{Tr}\left(\hat{\Phi}^\dagger(t) \hat{c}^\dagger_{i,\sigma} \hat{\Phi}(t) \hat{d}_{i,\sigma'}\right) && \text{(A.50)}\\
Q_{i,\sigma,\sigma'} &= \frac{\sigma \delta_{\sigma,-\sigma'}}{\sqrt{n^0_{i,\sigma'}(1 - n^0_{i,\sigma'})}} \mathrm{Tr}\left(\hat{\Phi}^\dagger(t) \hat{c}_{i,\sigma} \hat{\Phi}(t) \hat{d}_{i,\sigma'}\right). && \text{(A.51)}
\end{aligned}$$

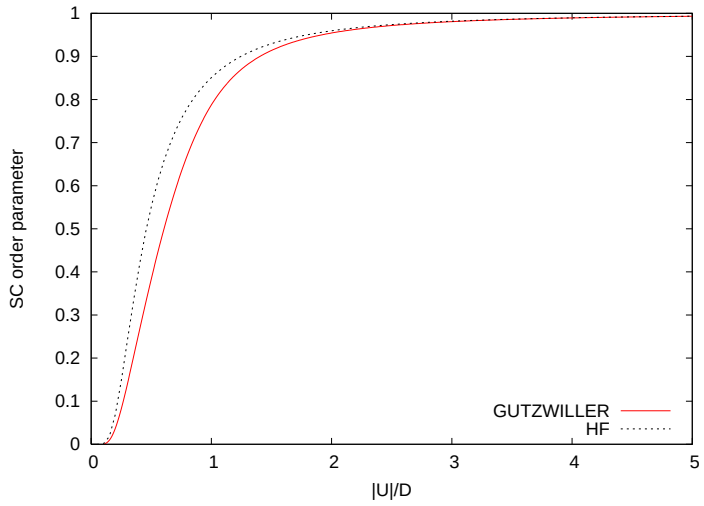

Fig. A.1: Superconducting order parameter in the attractive Hubbard model. The superconducting order parameter computed for the attractive Hubbard model minimizing the Gutzwiller energy functional within the Gutzwiller approximation. For comparison the Hartree-Fock (BCS) result is plotted (dashed line).

leading to the effective Hamiltonian

$$\begin{aligned}\mathcal{H}_* \;=\; & \sum_{i,j}\left[|R_\uparrow|^2-|Q_{\uparrow,\downarrow}|^2\right]d^\dagger_{i,\uparrow}d_{j,\uparrow}-\sum_{i,j}\left[|R_\downarrow|^2-|Q_{\downarrow,\uparrow}|^2\right]d_{i,\downarrow}d^\dagger_{j,\downarrow}+\\ & \sum_{i,j}\left[R_\uparrow Q_{\uparrow,\downarrow}-R_\downarrow Q_{\downarrow,\uparrow}\right]d^\dagger_{i,\uparrow}d^\dagger_{j,\downarrow}+\sum_{i,j}\left[R^*_\uparrow Q^*_{\uparrow,\downarrow}-R^*_\downarrow Q^*_{\downarrow,\uparrow}\right]d_{i,\downarrow}d_{j,\uparrow}.\end{aligned}$$

In this spin symmetric case

$$R_\uparrow = R_\downarrow = R \quad \text{and} \quad Q_{\uparrow\downarrow} = -Q_{\downarrow\uparrow} = Q. \tag{A.52}$$

Using suitable angular variables we can satisfy by construction the constraints A.43, A.45 and A.46, so that the effective Hamiltonian reads

$$\mathcal{H}_* = \sum_{\mathbf{k}}\psi^\dagger_{\mathbf{k}}\begin{pmatrix}\tau\epsilon_{\mathbf{k}}+\nu & D\epsilon_{\mathbf{k}}\\ D^*\epsilon_{\mathbf{k}} & -\tau\epsilon_{\mathbf{k}}-\nu\end{pmatrix}\psi_{\mathbf{k}}-\nu\sum_i\left(n^0_i-1\right) \tag{A.53}$$

with $\psi^\dagger_{\mathbf{k}}\equiv\left(d^\dagger_{\mathbf{k},\uparrow},d_{-\mathbf{k},\downarrow}\right)$ and $D=2QR$ and $\tau=|R|^2-|Q|^2$.

Further defining $D_{\mathbf{k}}\equiv D\epsilon_{\mathbf{k}}$ and $\tau_{\mathbf{k}}\equiv\tau\epsilon_{\mathbf{k}}+\nu$ we write

$$\mathcal{H}_* = \sum_{\mathbf{k}} D^{\mathrm{R}}_{\mathbf{k}}\sigma^1_{\mathbf{k}} - D^{\mathrm{I}}_{\mathbf{k}}\sigma^2_{\mathbf{k}} + \tau_{\mathbf{k}}\sigma^3_{\mathbf{k}} \tag{A.54}$$

with

$$\sigma^\alpha_{\mathbf{k}} = \psi^\dagger_{\mathbf{k}}\sigma^\alpha\psi_{\mathbf{k}}, \tag{A.55}$$

being σ^α Pauli matrices with $\alpha = 0, 1, 2, 3$ and

$$D^{\mathrm{R}}_{\mathbf{k}} = \mathrm{Re}(D_{\mathbf{k}}) \qquad D^{\mathrm{I}}_{\mathbf{k}} = \mathrm{Im}(D_{\mathbf{k}}). \tag{A.56}$$

The variational energy A.47 can be efficiently optimized using the recursive scheme proposed in Ref. [129]. In Fig. A.1 we show the results for the order parameter compared to the standard BCS result.

A.2.2 Non-equilibrium dynamics

The dynamics is simplified by the fact that the constraints are conserved during the time evolution and therefore they must be enforced only at initial time. Following the prescription of Eqs. A.37-A.38 we express the time evolution of the uncorrelated wave-function using the equation of motion for the expectation value of the of the operators $\sigma^\alpha_{\mathbf{k}}$ on the uncorrelated wave-function

$$i\langle\dot{\sigma}^\alpha_{\mathbf{k}}\rangle = \langle[\mathcal{H}_*, \sigma^\alpha_{\mathbf{k}}]\rangle, \tag{A.57}$$

obtaining

$$\langle\dot{\sigma^1_{\mathbf{k}}}\rangle = -2\tau_{\mathbf{k}}\langle\sigma^2_{\mathbf{k}}\rangle - 2D^{\mathrm{I}}_{\mathbf{k}}\langle\sigma^3_{\mathbf{k}}\rangle \tag{A.58}$$

$$\langle\dot{\sigma^2_{\mathbf{k}}}\rangle = 2\tau_{\mathbf{k}}\langle\sigma^1_{\mathbf{k}}\rangle - 2D^{\mathrm{R}}_{\mathbf{k}}\epsilon_{\mathbf{k}}\langle\sigma^3_{\mathbf{k}}\rangle \tag{A.59}$$

$$\langle\dot{\sigma^3_{\mathbf{k}}}\rangle = 2D^{\mathrm{R}}_{\mathbf{k}}\langle\sigma^2_{\mathbf{k}}\rangle - 2D^{\mathrm{I}}_{\mathbf{k}}\langle\sigma^1_{\mathbf{k}}\rangle. \tag{A.60}$$

Similarly, the direct derivation of the effective Hamiltonian $\mathcal{H}_*$ leads to the dynamical equations for the variational matrices $\hat{\Phi}$. Representing the $\hat{\Phi}$ entries in vector form, *i.e.*

$$\overrightarrow{\Phi} \equiv \begin{pmatrix} \phi_{00} \\ \phi_{02} \\ \phi_{20} \\ \phi_{22} \\ \phi_1 \end{pmatrix} \tag{A.61}$$

we can write the matricial Schrödinger equation in the form

$$i\dot{\overrightarrow{\Phi}} = \widehat{H}[\Phi]\overrightarrow{\Phi}. \tag{A.62}$$

Using the following definitions

$$\mathcal{Z} \equiv \langle\Psi_0|\frac{1}{2}\sum_{\mathbf{k},\sigma}\epsilon_{\mathbf{k}}d^\dagger_{\mathbf{k},\sigma}d_{\mathbf{k},\sigma}|\Psi_0\rangle = \frac{1}{2}\sum_{\mathbf{k}}\epsilon_{\mathbf{k}}\langle\sigma^3_{\mathbf{k}}\rangle \tag{A.63}$$

$$\Lambda \equiv \langle\Psi_0|\sum_{\mathbf{k}}\epsilon_{\mathbf{k}}d^\dagger_{\mathbf{k}\uparrow}d^\dagger_{-\mathbf{k}\downarrow}|\Psi_0\rangle = \frac{1}{2}\sum_{\mathbf{k}}\epsilon_{\mathbf{k}}\left[\langle\sigma^1_{\mathbf{k}}\rangle + i\langle\sigma^2_{\mathbf{k}}\rangle\right] \tag{A.64}$$

$$\Gamma_+ \equiv Q\Lambda + R^*\mathcal{Z} \tag{A.65}$$
$$\Gamma_- \equiv R\Lambda - Q^*\mathcal{Z} \tag{A.66}$$
$$\Upsilon \equiv 2\tau\mathcal{Z} + 2\mathrm{Re}(\Delta\Lambda) \tag{A.67}$$

the Hamiltonian $\widehat{H}$ reads

$$\widehat{H} = \begin{pmatrix} \frac{U}{2} & 0 & 0 & 0 & \frac{2\Gamma_+^*}{\sqrt{n^0(2-n^0)}} \\ 0 & \frac{U}{2} + 4\Upsilon\frac{n^0-1}{n^0(2-n^0)} & 0 & 0 & \frac{2\Gamma_-}{\sqrt{n^0(2-n^0)}} \\ 0 & 0 & \frac{U}{2} & 0 & \frac{2\Gamma_-^*}{\sqrt{n^0(2-n^0)}} \\ 0 & 0 & 0 & \frac{U}{2} + 4\frac{n^0-1}{n^0(2-n^0)}\Upsilon & \frac{2\Gamma_+}{\sqrt{n^0(2-n^0)}} \\ \frac{2\Gamma_+}{\sqrt{n^0(2-n^0)}} & \frac{2\Gamma_-^*}{\sqrt{n^0(2-n^0)}} & \frac{2\Gamma_-}{\sqrt{n^0(2-n^0)}} & \frac{2\Gamma_+^*}{\sqrt{n^0(2-n^0)}} & 2\frac{n^0-1}{n^0(2-n^0)}\Upsilon \end{pmatrix}. \tag{A.68}$$

In Sec. 4.4 we numerically integrate the system of differential equations A.58-A.60 and A.62 starting from the initial conditions Eq. 4.41. In particular, indicating with λ the value of the attractive interaction for which the ground state of the BCS Hamiltonian 4.30 has the order parameters Δ_0 the initial conditions for the uncorrelated wave-function read

$$\begin{aligned} \langle\sigma^1_{\mathbf{k}}\rangle(t=0) &= \frac{\epsilon_{\mathbf{k}}}{E(\mathbf{k})} \\ \langle\sigma^2_{\mathbf{k}}\rangle(t=0) &= 0 \\ \langle\sigma^3_{\mathbf{k}}\rangle(t=0) &= -\frac{\lambda\Delta_0}{E(\mathbf{k})} \end{aligned} \tag{A.69}$$

with $\epsilon_{\mathbf{k}}$ the electronic dispersion and $E(\mathbf{k}) = \sqrt{\epsilon^2 + \lambda^2\Delta_0^2}$. The initial condition for the variational matrix reads

$$\begin{aligned} \phi_{00} &= \frac{1}{\sqrt{2}}\left(1 - \frac{n^0}{2}\right) \\ \phi_{20} &= \frac{1}{2}\left(1 - \frac{n^0}{2}\right) \\ \phi_{02} &= -\frac{1}{2}\frac{n^0}{2} \\ \phi_{22} &= \frac{1}{\sqrt{2}}\frac{n^0}{2} \\ \phi_1 &= \sqrt{\left(1 - \frac{n^0}{2}\right)\frac{n^0}{2}}, \end{aligned} \tag{A.70}$$

with

$$n^0 = \frac{1}{2}\sum_{\mathbf{k}}\langle\sigma^3_{\mathbf{k}}\rangle + 1. \tag{A.71}$$

A.3 Gutzwiller Approximation for non-equilibrium transport

In this sections we report the details of the calculations for the non-equilibrium transport problem reported in Chap. 5.

A.3.1 Details on the variational dynamics

We start deriving the dynamical equations for the variational dynamics defined by equations 5.10-5.11. A straightforward differentiation of the effective one-body Hamiltonian Eq. (5.14) with respect to the variational matrices $\hat{\Phi}_i$ leads to the following equation of motions

$$i\frac{\partial}{\partial t}\begin{pmatrix}\Phi_{z,0}(t)\\ \Phi_{z,1}(t)\\ \Phi_{z,2}(t)\end{pmatrix}=\begin{pmatrix}h_{00}(z,t) & h_{01}(z,t) & 0\\ h_{01}^{*}(z,t) & 0 & h_{01}(z,t)\\ 0 & h_{01}^{*}(z,t) & h_{22}(z,t)\end{pmatrix}\begin{pmatrix}\Phi_{z,0}(t)\\ \Phi_{z,1}(t)\\ \Phi_{z,2}(t)\end{pmatrix}. \tag{A.72}$$

Defining the following quantum averages of fermionic operators over the uncorrelated wave-function $|\Psi_0(t)\rangle$

$$\begin{aligned}\varepsilon_z(t)&=\sum_{\mathbf{k}\sigma}\langle\Psi_0(t)|\, d^{\dagger}_{\mathbf{k}z\sigma}d_{\mathbf{k}z\sigma}\,|\Psi_0(t)\rangle\\ \Delta_z(t)&=\sum_{\mathbf{k}\sigma}\langle\Psi_0(t)|\, d^{\dagger}_{\mathbf{k}z+1\sigma}d_{\mathbf{k}z\sigma}\,|\Psi_0(t)\rangle\\ \Gamma_\alpha(t)&=\sum_{\mathbf{k}\sigma}\sum_{k_\perp}v_{k_\perp}\langle\Psi_0(t)|\, d^{\dagger}_{\mathbf{k}z_\alpha\sigma}c_{\mathbf{k}k_\perp\alpha\sigma}\,|\Psi_0(t)\rangle,\end{aligned} \tag{A.73}$$

the expression for the elements of the matrix A.72 read

$$\begin{aligned}h_{00}(z,t)=\frac{U}{2}-E_z+\frac{\delta_z}{1-\delta_z^2}\Big\{&2\,|R_z|^2\,\varepsilon_z-\Big[R^{*}_{z+1}\,R_z\,\Delta_z\,\big(1-\delta_{z,N}\big)+c.c.\Big]\\ &-\Big[R^{*}_{z-1}\,R_z\,\Delta^{*}_{z-1}\,\big(1-\delta_{z,1}\big)+c.c.\Big]\\ &+\Big[\delta_{z,1}\,R_1^{*}\,\Gamma_L+\delta_{z,N}\,R_N^{*}\,\Gamma_R+c.c.\Big]\Big\},\end{aligned} \tag{A.74}$$

$$\begin{aligned}h_{22}(z,t)=\frac{U}{2}+E_z-\frac{\delta_z}{1-\delta_z^2}\Big\{&2\,|R_z|^2\,\varepsilon_z-\Big[R^{*}_{z+1}\,R_z\,\Delta_z\,\big(1-\delta_{z,N}\big)+c.c.\big)\Big]\\ &-\Big[R^{*}_{z-1}\,R_z\,\Delta^{*}_{z-1}\,\big(1-\delta_{z,1}\big)+c.c.\Big]\\ &+\Big[\delta_{z,1}R_1^{*}\Gamma_L+\delta_{z,N}R_N^{*}\Gamma_R+c.c.\Big]\Big\}\end{aligned} \tag{A.75}$$

and

$$h_{01}(z,t) = \frac{\sqrt{2}}{\sqrt{1-\delta_z^2}}\Big[R_z^*\,\varepsilon_z - R_{z+1}^*\,\Delta_z\left(1-\delta_{z,N}\right) - R_{z-1}^*\,\Delta_{z-1}^*\left(1-\delta_{z,1}\right) + \delta_{z,1}\,\Gamma_L^* + \delta_{z,N}\,\Gamma_R^*\Big]. \tag{A.76}$$

The time evolution of the averages of fermionic operators over the uncorrelated wave-function Eqs. A.73 is set by the effective Schrödinger equation (5.10). To solve this dynamics we introduce the Keldysh Greens' functions on the uncorrelated wave-function for c and d operators

$$\mathcal{G}^K_{\mathbf{k}\sigma}(z,z';t,t') = -i\,\langle T_K\left(d_{\mathbf{k}z\sigma}(t)\,d^\dagger_{\mathbf{k}z'\sigma}(t')\right)\rangle \tag{A.77}$$

$$g^K_{\mathbf{k}k_\perp\alpha\sigma}(z;t,t') = -i\,\langle T_K\left(c_{\mathbf{k}k_\perp\alpha\sigma}(t)d^\dagger_{\mathbf{k}z'\sigma}(t')\right)\rangle \tag{A.78}$$

and express the quantities in Eqs. A.73 in terms of their lesser components computed at equal time

$$\begin{aligned}\langle d^\dagger_{\mathbf{k}z\sigma}d_{\mathbf{k}z'\sigma}\rangle(t) &= -\,i\,\mathcal{G}^<_{\mathbf{k}\sigma}(z',z;t,t)\\ \langle d^\dagger_{\mathbf{k}z\sigma}c_{\mathbf{k}k_\perp\alpha\sigma}\rangle(t) &= -\,i\,g^<_{\mathbf{k}k_\perp\alpha\sigma}(z;t,t).\end{aligned} \tag{A.79}$$

We compute the equations of motion for the lesser components at equal times, Eq. (A.79), using the Heisenberg evolution for operators c and d with Hamiltonian $\mathcal{H}_*$. In order to get a closed set of differential equations we have to further introduce the dynamics for the leads lesser Green function, which due to the hybridization with the slab lose its translational invariance in the z-direction

$$\left[G^{\alpha\alpha'}_{\mathbf{k}k_\perp k'_\perp\sigma}\right]^<(t,t) = i\langle c^\dagger_{\mathbf{k}k_\perp\alpha\sigma}c_{\mathbf{k}k'_\perp\alpha'\sigma}\rangle. \tag{A.80}$$

Dropping, for the sake of simplicity, the lesser symbol and the spin index we get for each $\mathbf{k}$ point the following equations of motion

$$\begin{aligned}i\partial_t\mathcal{G}_{\mathbf{k}}(z,z') = {}&\epsilon_{\mathbf{k}}\Big(|R_z|^2-|R_{z'}|^2\Big)\,\mathcal{G}_{\mathbf{k}}(z,z') + \sum_{i=\pm1} R^*_{z+i}\,R_z\,\mathcal{G}_{\mathbf{k}}(z+i,z') - R^*_z\,R_{z+i}\,\mathcal{G}_{\mathbf{k}}(z,z'+i)\\ &+\sum_{\alpha=L,R}\delta_{z,z_\alpha}\,R^*_{z_\alpha}\sum_{k_\perp} v^\alpha_{k_\perp}\,g^\alpha_{\mathbf{k}k_\perp}(z') + \sum_{\alpha=L,R}\delta_{z'z_\alpha}\,R_{z_\alpha}\sum_{k_\perp} v^\alpha_{k_\perp}\Big[g^\alpha_{\mathbf{k}k_\perp}(z)\Big]^*,\end{aligned} \tag{A.81}$$

$$\begin{aligned}i\partial_t g^\alpha_{\mathbf{k}k_\perp}(z) = {}&\left(\varepsilon^\alpha_{\mathbf{k}}+t^\alpha_{k_\perp}\right)g^\alpha_{\mathbf{k}k_\perp}(z) - R^*_{z+1}\,R_z\,g^\alpha_{\mathbf{k}k_\perp}(z+1) - R^*_{z-1}\,R_z\,g^\alpha_{\mathbf{k}k_\perp}(z-1)\\ &+ v^\alpha_{k_\perp}\,R_{z_\alpha}\,\mathcal{G}_{\mathbf{k}}(z_\alpha,z) - \sum_{\alpha'=L,R}\delta_{z_{\alpha'},z}\sum_{k_\perp} v^\alpha_{k_\perp}\,R_{z_{\alpha'}}\,G^{\alpha\alpha'}_{\mathbf{k}k_\perp k'_\perp},\end{aligned} \tag{A.82}$$

$$i\partial_t G^{\alpha\alpha'}_{\mathbf{k}k_\perp k'_\perp} = \left(t^\alpha_{k_\perp}-t^{\alpha'}_{k'_\perp}\right)G^{\alpha\alpha'}_{\mathbf{k}k_\perp k'_\perp} - v^{\alpha'}_{k'_\perp}\,R^*_{z_{\alpha'}}\,g^\alpha_{\mathbf{k}k_\perp}(z) - v^\alpha_{k_\perp}\,R_{z_{\alpha'}}\left[g^{\alpha'}_{\mathbf{k}k'_\perp}(z)\right]^*. \tag{A.83}$$

The set of differential equations, composed by Eqs. (A.81-A.83) and A.72, completely determines the dynamics within the TDG approximation and it is solved using a standard $4-th$ order implicit Runge-Kutta method [137]. We mention that this strategy for the solution of the Gutzwiller dynamics correspond to a discretization of the semi-infinite metallic leads. In principle, the latter can be integrated-out exactly at the cost of solving the dynamics for the lesser($<$) and greater($>$) component of the Keldysh Greens' function on the whole two times (t, t')-plane. However, such a route can be extremely costly from a computational point of view and restrict the simulations to small evolution times. We explicitly checked that the dynamics using the above leads discretization coincides with the dynamics obtained with the two time (t, t')-plane evolution, up to times for which finite size effects occur. The latter can be however pushed far away with respect to the maximum times reachable within the two time (t, t')-plane evolution.

A.3.2 Landau-Zener stationary tunneling within the Gutzwiller approximation

Here we explicitly show how the Landau-Zener stationary tunnelling across the Mott-Hubbard gap in the presence of a voltage drop translates into the language of the TDG approximation. Here, the gap and the voltage bias are actually absorbed into layer-dependent hopping renormalization factors $R_z(t)$ so that, an electron entering the Mott insulating slab from the metal lead translates into a free quasi-particle with hopping parameters that decay exponentially inside the insulator. In other words, quasi-particles within the Gutzwiller approximation do not experience a tunneling barrier in the insulating side but rather an exponentially growing mass.

From this viewpoint, the *living layer* that appears at the metal-Mott insulator interface can be legitimately regarded as the evanescent wave yielded by tunnelling across the Mott-Hubbard gap. Such a correspondence can be made more explicit following Ref. [103] and its Supplemental Material.

Specifically, we shall consider a single metal-Mott insulator interface at equilibrium, with the metal and the Mott insulator confined in the regions $z < 0$ and $z \geq 0$, respectively. The new ingredient that we add with respect to Ref. [103] is an electrochemical potential $\mu(z)$, which is constant and for convenience zero on the metal side, i.e. $\mu(z < 0) = 0$, while finite on the insulating side, $\mu(z \geq 0) \neq 0$, thus mimicking the bending of the Mott-Hubbard side bands at the junction.

If the correlation length ξ of the Mott insulator is much bigger that the inverse Fermi wavelength, in the Gutzwiller approach we can further neglect as a first approximation the z-dependence of the averages of hopping operators over the uncorrelated Slater determinant $|\,\Psi_0\rangle$ [103]. We can thus write the energy of the system as a functional of the variational matrices only,

$$\begin{aligned} E = &-\frac{2}{24\,L}\sum_z R(z)^2 - \frac{1}{24\,L}\sum_z R(z)\,R(z+1) \\ &+ \frac{1}{2\,L}\sum_z u(z)\left(\,|\,\Phi_0(z)\,|^2 + |\,\Phi_2(z)\,|^2\,\right) - \frac{1}{L}\sum_z \mu(z)\,\delta(z), \end{aligned} \tag{A.84}$$

where

$$R(z) \;=\; \sqrt{\frac{2}{1-\delta(z)^2}}\;\Big(\Phi_1(z)^*\,\Phi_0(z)\;+\Phi_2(z)^*\,\Phi_1(z)\;\Big),$$

is the hopping renormalization factor, and

$$\delta(z) = \mid \Phi_0(z)\mid^2 - \mid \Phi_2(z)\mid^2,$$

is the doping of layer z with respect to half-filling, i.e. $n(z) = 1-\delta(z)$. We have chosen units such that the Mott transition occurs at $u=1$, so that $u(z<0) = U_{\rm metal} \ll 1$ on the metal side, and $u(z\geq 0) = U \gtrsim 1$ on the insulating one.

The minimum of E in Eq. (A.84) can be always found with real parameters $\Phi_n(z)$, so that, since

$$\Phi_0(z)^2 + \Phi_1(z)^2 + \Phi_2(z)^2 = 1,$$

there are actually two independent variables per layer. We can always choose these variables as $R(z)\in[0,1]$ and $\delta(z)\in[-1,1]$, in which case

$$\mid \Phi_0(z)\mid^2 + \mid \Phi_2(z)\mid^2 \;=\; \frac{1}{2}\left(\Xi\big[R(z),\delta(z)\big] + \frac{\delta(z)^2}{\Xi\big[R(z),\delta(z)\big]}\right),$$

where

$$\begin{aligned}\Xi\big[R(z),\delta(z)\big] \;&=\; 1-\sqrt{1-R(z)^2}\;\sqrt{1-\delta(z)^2}\\ &\simeq 1-\sqrt{1-R(z)^2}+\frac{\delta(z)^2}{2}\sqrt{1-R(z)^2},\end{aligned}$$

the last expression being valid for small doping. Minimizing E in Eq. (A.84) with respect to $\delta(z)$ leads to

$$\delta(z) \;\simeq\; \frac{4\mu(z)}{U}\,\frac{1-\sqrt{1-R(z)^2}}{1+R(z)^2+\sqrt{1-R(z)^2}}, \tag{A.85}$$

for $z\geq 0$, and $\delta(z)=0$ for $z<0$.

Through Eq. (A.85) we find an equation for $R(z)$ in the insulating side $z\geq 0$ that, after taking the continuum limit, reads

$$\frac{\partial^2 R(z)}{\partial z^2} = -\frac{\partial}{\partial R(z)}\,V\Big[R(z),z\Big], \tag{A.86}$$

which looks like a classical equation of motion with z playing the role of time t, $R(z)$ that of the coordinate $q(t)$, and V that of a time-dependent potential

$$V\big(q,t\big) \;=\; -6u\left(1-\sqrt{1-q^2}\right)+3q^2+\frac{48\mu(t)^2}{u}\,\frac{1-\sqrt{1-q^2}}{1+q^2+\sqrt{1-q^2}}. \tag{A.87}$$

On the metallic side $R(z<0) \simeq R_{\rm metal} \simeq 1$, so that the role of the junction is translated into appropriate boundary conditions at $z=0$.

Far inside the insulator, $R(z) \ll 1$ and we can expand

$$V\Big[R(z),z\Big] \;\simeq\; \left(-3U+3+24\,\frac{\mu(z)^2}{u}\right)\,R(z)^2,$$

so that the linearized equation reads

$$\frac{\partial^2 R(z)}{\partial z^2} = \left[6u-6-\frac{48}{u}\,\mu(z)^2\right]\,R(z), \tag{A.88}$$

for $z>0$, while, in the metal side, $z<0$, where $R(z)$ is approximately constant,

$$\frac{\partial^2 R(z)}{\partial z^2} = 0. \tag{A.89}$$

Equations (A.88) and (A.89) can be regarded as the Shrœdinger equation of a zero-energy particle impinging on a potential barrier at $z \geq 0$. Within the WKB approximation, the transmitted wave-function at z reads

$$R(z) \propto \exp\left(-\int_0^{z_*} d\zeta\,\sqrt{6u-6-\frac{48}{u}\,\mu(\zeta)^2}\,\right), \tag{A.90}$$

where, assuming a monotonous $\mu(\zeta)$, the upper limit of integration is $z_*=z$ if $8\mu(z)^2 \leq u\,(u-1)$ otherwise is the turning point, i.e. z_* such that $8\mu(z_*)^2 = u\,(u-1)$.

Let us for instance take $\mu(z) = \mathrm{E}\,z$, which corresponds to a constant electric field. In this case

$$|\mathrm{E}|\,z_* = \sqrt{\frac{u(u-1)}{8}}, \tag{A.91}$$

so that the transmission probability

$$|R(z>z_*)|^2 \sim \exp\left(-\frac{E_{\rm th}}{E}\right), \tag{A.92}$$

where the threshold field

$$E_{\rm th} = \frac{\pi}{2}\,\sqrt{\frac{u}{48}}\,\xi^{-2}, \tag{A.93}$$

with the definition of the correlation length $\xi^{-1} = \sqrt{6(u-1)}$ of Ref. [103].

We observe that Eq. (A.92) has exactly the form predicted by the Zener tunnelling in a semiconductor upon identifying

$$E_g\,\sqrt{\frac{m_*\,E_g}{\hbar^2}} \sim u-1, \tag{A.94}$$

where E_g is the semiconductor gap, m_* the mass parameter and U_c the dimensional value of the interaction at the Mott transition.

A.3.3 Growth of the living layer

The same approximate approach just outlined can be also extended away from equilibrium. We shall here consider the simple case of constant and vanishing electro-chemical potential $\mu(z) = 0$. We need to find the saddle point of the action

$$S = \int dt\, i \sum_{n=0}^{2} \sum_{z} \Phi_n(z,t)^* \, \dot{\Phi}_n(z,t) \; - E(t), \tag{A.95}$$

where $E(t)$ is the same functional of Eq. (A.84) where now all parameters $\Phi_n(z,t)$ are also time dependent. At $\mu(z) = 0$ we can set

$$\Phi_0(z,t) \;=\; \Phi_2(z,t) = \frac{1}{\sqrt{2}}\, \mathrm{e}^{i\phi(z,t)} \, \sin\frac{\theta(z,t)}{2}, \tag{A.96}$$

$$\Phi_1(t) \;=\; \cos\frac{\theta(z,t)}{2}, \tag{A.97}$$

so that the equations of motion read

$$\sin\theta(z,t)\,\dot{\phi}(z,t) \;=\; -2\,\frac{\partial E}{\partial\theta(z,t)}, \tag{A.98}$$

$$\sin\theta(z,t)\,\dot{\theta}(z,t) \;=\; 2\,\frac{\partial E}{\partial\phi(z,t)}. \tag{A.99}$$

Upon introducing the parameters

$$\sigma_x(z,t) \;=\; \sin\theta(z,t)\,\cos\phi(z,t), \tag{A.100}$$

$$\sigma_y(z,t) \;=\; \sin\theta(z,t)\,\sin\phi(z,t), \tag{A.101}$$

$$\sigma_z(z,t) \;=\; \cos\theta(z,t), \tag{A.102}$$

where $\sigma_x(z,t) = R(z,t)$ is the time dependent hopping renormalization, the equations of motion can be written as

$$\dot{\sigma}_x(z,t) \;=\; -2\sigma_y(z,t)\,\frac{\partial E}{\partial\sigma_z(z,t)} = \frac{u}{2}\,\sigma_y(z,t), \tag{A.103}$$

$$\begin{aligned}\dot{\sigma}_y(z,t) \;&=\; 2\sigma_x(z,t)\,\frac{\partial E}{\partial\sigma_z(z,t)} - 2\sigma_z(z,t)\,\frac{\partial E}{\partial\sigma_x(z,t)} \\ &= -\frac{u}{2}\,\sigma_x(z,t) - 2\sigma_z(z,t)\,\frac{\partial E}{\partial\sigma_x(z,t)},\end{aligned} \tag{A.104}$$

$$\dot{\sigma}_z(z,t) \;=\; 2\sigma_y(z,t)\,\frac{\partial E}{\partial\sigma_x(z,t)}, \tag{A.105}$$

where

$$\begin{aligned}\frac{\partial E}{\partial\sigma_x(z,t)} \;&=\; -\frac{1}{6}\,\sigma_x(z,t) - \frac{1}{24}\,\Big(\sigma_x(z+1,t) + \sigma_x(z-1,t)\Big) \\ &\simeq -\frac{1}{4}\,\sigma_x(z,t) - \frac{1}{24}\,\frac{\partial^2\sigma_x(z,t)}{\partial z^2}.\end{aligned} \tag{A.106}$$

The Eqs. (A.103)–(A.105) show that the Gutzwiller equations of motion actually coincide to those of a Ising model in a transverse field treated within mean-field, as originally observed in Ref. [49].

Inside the Mott insulating slab we can safely assume $\sigma_z(z,t) \sim 1$ and obtain the equation for $R(z,t) = \sigma_x(z,t)$

$$\ddot{R}(z,t) = -\frac{U}{4}\left(u-1\right) R(z,t) + \frac{u}{24}\,\frac{\partial^2 R(z,t)}{\partial z^2}, \tag{A.107}$$

which is the time dependent version of Eq. (A.88) and is just a Klein-Gordon equation

$$\frac{1}{c^2}\,\ddot{R} - \nabla^2\,R + m^2\,c^2\,R = 0, \tag{A.108}$$

with light velocity c and mass m given by

$$c^2 = u/24, \tag{A.109}$$

$$m^2\,c^2 = 6\left(u-1\right) = \xi^{-2}. \tag{A.110}$$

In dimensionless units

$$\frac{z}{\xi} \to z, \qquad \frac{ct}{\xi} \to t.$$

Eq. (A.108) reads

$$\ddot{R} - \nabla^2\,R + R = 0. \tag{A.111}$$

Let us simulate the growth of the "living layer" by a single metal-Mott insulator interface and absorb the role of the metal into an appropriate boundary condition for the surface $z = 0$ of the Mott insulator side $z \geq 0$. Specifically, we shall assume that initially $R(z,0) = R_0(z)$, with $R_0(0) = R_0 > 0$ and $R_0(z \to \infty) = 0$, as well as that, at any time t, the value of $R(z,t)$ at the surface remains constant, i.e. $R(0,t) = R_0$, $\forall t$. We denote as $R_*(z)$ the stationary solution of Eq. (A.111) with the boundary condition $R_*(0) = R_0$, that is

$$R_*(z) = R_0\,\mathrm{e}^{-z}. \tag{A.112}$$

One can readily obtain a solution of Eq. (A.111) satisfying all boundary condition, which, after defining

$$\phi(x) = R_0(x) - R_*(x), \tag{A.113}$$

reads

$$\begin{aligned} R(z,t) &= R_*(z) + \frac{\phi(z+t) + \theta(z-t)\,\phi(z-t) - \theta(t-z)\,\phi(t-z)}{2} \\ &\quad -\frac{t}{2}\int_{-t}^{t} dx\,\frac{J_1\Big(\sqrt{t^2-x^2}\Big)}{\sqrt{t^2-x^2}}\Big[\theta(x+z)\,\phi(x+z) - \theta(x-z)\,\phi(x-z)\Big], \end{aligned} \tag{A.114}$$

where $J_1(x)$ is the first order Bessel function. We observe that for very long times $R(z, t \to \infty) \to R_*(z)$, namely the solution evolves into a steady state that corresponds to the

equilibrium evanescent wave with the appropriate boundary condition. Moreover, Eq. (A.114) also shows a kind of light-cone effect compatible with the full evolution that takes into account also the dynamics of the Slater determinant, which we have neglected to get Eq. (A.111). In fact, the missing Slater determinant dynamics is the reason why the initial exponential growth is not captured by Eq. A.114, which thence has to be rather regarded as an asymptotic description valid only at long time and distances.

Another possible boundary condition is to impose that $\partial_z R(z,t)$ remains constant at $z=0$, rather than its value. In this case, if

$$A = -\frac{\partial R(z,0)}{\partial z}_{z=0} = -\frac{\partial R_0(z)}{\partial z}_{z=0}, \tag{A.115}$$

then we must take $R_*(z) = A\,\mathrm{e}^{-z}$ and still $\phi(x) = R_0(x) - R_*(x)$ so that the solution reads

$$\begin{aligned} R(z,t) &= R_*(z) + \frac{\phi(z+t) + \theta(z-t)\,\phi(z-t) + \theta(t-z)\,\phi(t-z)}{2} \\ &\quad -\frac{t}{2}\int_{-t}^{t} dx\, \frac{J_1\Big(\sqrt{t^2-x^2}\Big)}{\sqrt{t^2-x^2}}\Big[\theta(x+z)\,\phi(x+z) + \theta(x-z)\,\phi(x-z)\Big]. \end{aligned} \tag{A.116}$$

Also in this case $R(z,t)$ evolves towards a stationary value that, in dimensional units, reads

$$R(z, t\to\infty) = A\,\xi\,\mathrm{e}^{-z/\xi}, \tag{A.117}$$

hence growths exponentially at fixed A and z as the Mott transition is approached.

A.4 Gutzwiller Approximation for doped Hubbard model

Here we report the calculations that lead to the estimation of the critical chemical potential needed to dope a Mott insulator described within the single band Hubbard model

$$\mathcal{H} = \sum_{i,j\sigma} t_{ij} c^\dagger_{i\sigma} c_{j\sigma} + h.c. + \frac{U}{2}\sum_i (n_i - 1)^2 - \mu \sum_i n_i.$$

Here we shall not use the Φ matrix representation. Indeed, in this case the Gutzwiller projectors are easily parameterized in terms of the double occupancy density and the average doping computed over the variational wave-function

$$D \equiv \langle \Psi_G | n_{i\uparrow} n_{i\downarrow} | \Psi_G \rangle \tag{A.118}$$

$$\delta \equiv \langle \Psi_G | 1 - n_i | \Psi_G \rangle. \tag{A.119}$$

With these definitions we introduce the following parameterization of the Gutzwiller projector

$$\mathcal{P} = \sum_{n=0,\uparrow,\downarrow,2} P_n |n\rangle\langle n|, \tag{A.120}$$

where the sum extend over empty, singly and doubly occupied basis states.

Defining

$$P_0 = D + \frac{\delta}{2} \tag{A.121}$$

$$P_2 = D - \frac{\delta}{2} \tag{A.122}$$

$$P_1 = \sum_\sigma P_\sigma = 1 - 2D \tag{A.123}$$

the Gutzwiller constraints result automatically satisfied

$$P_0 + P_1 + P_2 = 1 \tag{A.124}$$

$$P_0 - P_2 = \delta \equiv 1 - n. \tag{A.125}$$

We compute the hopping renormalization $Z = R^2$ from Eq. A.12 obtaining

$$Z = \frac{2P_1}{1-\delta^2}\left(\sqrt{P_0} + \sqrt{P_1}\right)^2 = \frac{4(1-2D)}{1-\delta^2}\left(D + \sqrt{D^2 - \frac{\delta^2}{4}}\right). \tag{A.126}$$

The last equation implies $|\delta| < 2D$, so that we can write

$$\delta \equiv 2D\sin\theta \qquad \theta \in [-\pi, \pi] \tag{A.127}$$

and

$$Z(D,\theta) = \frac{4D(1-2D)}{1-\delta^2}\left(1 + \cos\theta\right). \tag{A.128}$$

We obtain the following variational energy as a function of D and of the angular variable θ

$$E(D,\theta) = \epsilon(\delta)Z(D,\theta) + UD - \mu\left(1 - 2D\sin\theta\right), \tag{A.129}$$

with

$$\epsilon(\delta) = \int_{-W}^{\epsilon_F(\delta)} \rho(\omega)\omega d\omega \quad \text{and} \quad \int_{-W}^{\epsilon_F(\delta)} \rho(\omega) d\omega = 1 - \delta.$$

For simplicity we consider a flat density of states $\rho(\omega) = \theta(W - |\omega|)/2W$ for which

$$\epsilon(\delta) = \epsilon_0(1 - \delta^2),$$

being ϵ_0 the average kinetic energy of the half filled band, so that Eq. A.129 becomes

$$E(D,\theta) = 4\epsilon_0 D(1-2D)\left(1 + \cos\theta\right) + UD - \mu\left(1 - 2D\sin\theta\right). \tag{A.130}$$

We minimize Eq. A.130 with respect to the variable θ to obtain the variational energy as a function only of the variable D

$$\frac{E(D)}{U_c} = -\frac{1}{2}D(1-2D)\left(1 + \frac{1-2D}{\sqrt{(1-2D)^2 + 16\mu_\star^2}}\right) + uD - \frac{8\mu_\star^2 D}{\sqrt{(1-2D)^2 + 16\mu_\star^2}} \tag{A.131}$$

where we defined $u \equiv U/U_c$ and $\mu_\star \equiv \mu/U_c$, being $U_c = -8\epsilon_0$ the critical value of the Brinkman-Rice transition.

Considering the insulating case $u > 1$ we can expand the variational energy for $D \simeq 0$ up to second order

$$\frac{E(D)}{U_c} \simeq \left(-\frac{1}{2} - \frac{1}{2}(1+16\mu_\star^2)\alpha_0 + u\right) D + (1+\alpha_1)\, D^2, \tag{A.132}$$

where

$$\alpha_0 = \frac{1}{\sqrt{1+16\mu_\star^2}} \quad \alpha_1 = \frac{2}{(1+16\mu_\star^2)^{3/2}} \tag{A.133}$$

For

$$\gamma \equiv -\frac{1}{2} - \frac{1}{2}(1+16\mu_\star^2)\alpha_0 + u < 0 \tag{A.134}$$

the variational energy has a minimum for $D > 0$, so that the critical value of the chemical potential as a function of U is obtained imposing the condition $\gamma = 0$ leading to

$$\mu_c(U) = \frac{1}{2}\sqrt{U(U-U_c)}. \tag{A.135}$$

Appendix B

Dynamical Mean Field Theory for inhomogeneous systems

In this Appendix we describe the Dynamical Mean Field Theory approach for inhomogeneous systems which we use in Chap. 6.

In the previous Appendix we introduced the Gutzwiller method for treating strong correlation effects. This approach is based on a very simple and intuitive variational ansatz for the ground state and time evolved wave-functions and becomes *variationally exact* in the limit of infinite coordination lattice. As we seen the method is able to describe non-perturbative effects of the electronic correlations as, *e.g.*, the metal-to-insulator transition. Nevertheless, it gives a simplified description of the transition: while the suppression of the spectral weight at the Fermi level is properly captured the insulating phase is represented by a trivial collection of electrons frozen on each lattice site. In particular, the Gutzwiller method does not account for the redistribution of the spectral weight, which in the insulating side of the transition should be located around the two atomic δ-peaks at $\pm U/2$, broadened by the hopping processes, *i.e.* the Hubbard bands.

The reason of such failure resides in the fact that within the Gutzwiller approach the electronic spectral weight is described in a standard mean-field fashion, namely solving an effective one-body problem determined by the *static* configuration of all the other electrons. This approach freezes all temporal quantum fluctuations and, as a matter of fact, it can give rise to a metal-insulator transition without long range order only if a correlation constraint on the weights of the local electronic configurations is introduced by means of the Gutzwiller projectors or similar slave particles approaches [136, 138–141].

The aim of DMFT is to systematically include in a mean-field like theory all the temporal fluctuations that describe the correlation induced redistribution of the spectral weight. As a mean-field approach, the focus of the DMFT is to construct an effective theory for a local quantity. In the case of DMFT this quantity is the local single-particle greens functions

$$G_{ii}^{\alpha\beta}(\tau,\tau') = -\langle \mathcal{T}_\tau \, c_{i\alpha}(\tau) c_{i\beta}^\dagger(\tau')\rangle. \tag{B.1}$$

Differently from a static mean-field this quantity is a dynamical object which naturally

encodes the informations on the time-dependent[1] fluctuations for an electron propagating from the site i in the state β at time τ' and returning to the same site i in the state α at time τ. In particular, this dynamical mean-field description of the local physics is obtained by means of an effective single-site problem in which a time-dependent field describes the coupling with the rest of the lattice. The latter is to be self-consistently determined. Similarly to the Gutzwiller approach the method relies on the limit of infinite lattice coordination where it gives an exact solution of the problem.

In the following we shall briefly review the method and then introduce its application in the case of the biased slab discussed in Chap. 6. In analogy with the discussion of the Gutzwiller method we shall consider the general multi-orbital Hamiltonian A.3 which we rewrite here for convenience

$$\mathcal{H} = \sum_{i,j} \sum_{\alpha,\beta} \left(t_{i,j}^{\alpha,\beta} c_{i,\alpha}^{\dagger} c_{j,\beta} + H.c. \right) + \sum_{i} H_i. \tag{B.2}$$

B.1 General formulation

The basic idea of DMFT is to map the original lattice problem onto an effective single-site problem. This idea is the starting point of all standard mean-field theories as *e.g.* the Weiss theory for a classical spin system $H = \sum_{ij} J_{ij} \boldsymbol{\sigma}_i \cdot \boldsymbol{\sigma}_j$. In this case the spin at a given site i is described in terms of an effective Hamiltonian containing a magnetic field determined by the average configuration of all the other spins $\boldsymbol{h}_i = \sum_j J_{ij} \langle \boldsymbol{\sigma}_j \rangle$

$$H_{eff}^{(i)} = \boldsymbol{h}_i \cdot \boldsymbol{\sigma}_i. \tag{B.3}$$

Therefore the effective magnetic field is computed self-consistently after solving the auxiliary problem (B.3). In close analogy the starting point of the DMFT approach is to assume that the local Green function at a given site, $G_{ii}^{\alpha\beta}(\tau, \tau')$ can be computed by means of an effective single-site dynamics defined by an effective action for the fermionic degrees of freedom at site i. This can be done rigorously integrating out the degrees of freedom for all the sites $j \neq i$ (cavity method). Important simplifications in the calculations arise from the limit of infinite coordination lattice $z \to \infty$. In fact, it turns out that in this limit the effective action can be expressed in terms of bare propagators which mimics all the exchange processes from the site i to the rest of the lattice. Explicitly

$$\mathcal{S}_{eff,i} = -\int_0^\beta d\tau \; H_i(\tau) - \int_0^\beta d\tau d\tau' \; \hat{c}_i^{\dagger}(\tau) \cdot \boldsymbol{\mathcal{G}}_{0,i}^{-1}(\tau - \tau') \cdot \hat{c}_i(\tau'), \tag{B.4}$$

where we used a vector notation for the fermionic Grassman variables

$$\hat{c}_i^{\dagger}(\tau) = \left(c_{i,1}^{\dagger}(\tau), \ldots, c_{i,L}^{\dagger}(\tau) \right),$$

being L the total number of local (orbital and spin) degrees of freedom. The symbol "$\cdot$" indicates the matrix product.

[1] Imaginary time in the case of (B.1).

The $L \times L$ matrix $\boldsymbol{\mathcal{G}}_{0,i}(\tau - \tau')$ contains the bare propagators of the effective single-site problem described by the action (B.4) and is the analogous of the effective magnetic field in Eq. B.3, hence the name *Weiss field*. The Weiss field completely determines the effective problem defined by the action B.4. It is straightforward to see that this action describes an effective single-impurity quantum impurity problem whose coupling with an effective bath is described by the Weiss field. Using different methods it is possible to solve the action B.4 to determine the impurity self-energy $\boldsymbol{\Sigma}_{imp,i}(i\omega_n)$, which describes the effects of the interaction at the single-particle level.

In order to solve the problem self-consistency relations connecting $\boldsymbol{\mathcal{G}}_{0,i}(\tau - \tau')$ to quantities computable from the action (B.4) must be supplemented. These latter, called *DMFT equations*, have a rigorous derivation in the limit of infinite lattice coordination $z \to \infty$, starting from the cavity method [115] or the linked cluster expansion around the atomic limit [115, 142]. In this limit the theory is local [134, 143], namely the self-energy including all the many-body correlations is diagonal in space

$$\boldsymbol{\Sigma}_{ij}(i\omega_n) = \delta_{ij}\boldsymbol{\Sigma}_{ii}(i\omega_n) \tag{B.5}$$

and the DMFT approach gives an exact solution of the problem, provided an exact solution of the auxiliary problem (B.4).

Here we shall not prove the rigorous derivation, while we will just present the DMFT equations which naturally arise from the DMFT approximation in systems with finite coordination lattices. In particular, this is based on the assumptions that *i*) the self-energy is local, as in the $z \to \infty$ case, and *ii*) coincides with the self-energy of the effective single-site problem

$$\boldsymbol{\Sigma}_{ij}(i\omega_n) = \delta_{ij}\boldsymbol{\Sigma}_{imp,i}(i\omega_n). \tag{B.6}$$

We shall show the consequences of these assumptions in the case of a finite-size lattice with N sites and N effective single-site problems. From the definition of the single-site problems (B.4) we can calculate the local Green's function for a given site using the Dyson equation for the auxiliary problem

$$\boldsymbol{G}_{ii}^{-1}(i\omega_n) = \boldsymbol{\mathcal{G}}_{0,i}^{-1}(i\omega_n) - \boldsymbol{\Sigma}_{imp,i}(i\omega_n). \tag{B.7}$$

Moreover, we can use the relation between the lattice and the impurity self-energies (B.6) to express the lattice Green's function

$$\left(\hat{\boldsymbol{G}}^{-1}\right)_{ij}(i\omega_n) = \delta_{ij}\left[i\omega_n \mathbb{I}_{L\times L} - \boldsymbol{\Sigma}_{ii}(i\omega_n)\right] - \boldsymbol{t}_{ij}, \tag{B.8}$$

where we indicate with $\hat{\boldsymbol{G}}$ the $LN \times LN$ Greens' function matrix constructed with all the $L \times L$ matrices $\boldsymbol{G}_{ij}$. Eqs. (B.7-B.8) provide an implicit functional relation between $\boldsymbol{G}_{ii}$ and $\boldsymbol{\mathcal{G}}_{0,i}(i\omega_n)$ that is used to determine both quantities in a self-consistent loop starting from initial guesses.

Eq. (B.8) can be readily extended to case of an infinite lattice with translational symmetry taking the Fourier transform of both sides. In this case the self-energy lose any spatial dependence and Eq. (B.8) simply reduces to

$$\boldsymbol{G}_{\mathbf{k}}^{-1}(i\omega_n) = i\omega_n \mathbb{I}_{L\times L} - \boldsymbol{\Sigma}(i\omega_n) - \boldsymbol{h}_{\mathbf{k}}, \tag{B.9}$$

with $\boldsymbol{h}_{\mathbf{k}} = \sum_i e^{i\mathbf{k}\mathbf{R}_\mathbf{i}} \boldsymbol{t}_{ij}$ and the single-site local Greens' function determined by

$$\boldsymbol{G}(i\omega_n) = \sum_{\mathbf{k}} \boldsymbol{G}_{\mathbf{k}}(i\omega_n). \tag{B.10}$$

For this latter case we stress the fact that if the model is defined on a lattice with infinite coordination, as *e.g.* the Bethe lattice or the ∞-dimensional hyper-cubic lattice, Eqs. B.7-B.9 provide an exact solution of the model. The $z \to \infty$ limit has as the most important consequence that the theory is local [134, 143], namely that equation (B.6) holds. This can be shown in the skeleton expansion of the self-energy using arguments similar to the one discussed in App. A.1 to derive the expression for the Gutzwiller energy functional in the $z \to \infty$ limit. On the contrary, the use of the DMFT in lattices with finite coordination is an approximation which corresponds to neglect all the spatial fluctuations. These latter can be included enlarging the number of sites which define the effective problems (B.4) in a procedure called cluster (or cellular) DMFT [144, 145]. However, due to fast growing complexity of the problem, only correlations on short length scales can be included.

To explicitly solve the DMFT equations (B.7-B.8) it is useful to give an explicit Hamiltonian representation for the auxiliary impurity problem B.4. In this case, we introduce for each site an interacting impurity coupled to a not-interacting bath which gives an explicit representation of the local Weiss field

$$H^{(i)}_{imp} = \sum_{\alpha=1}^{L} \sum_n \epsilon_{i,\alpha,n} d^\dagger_{i\alpha,n} d_{i\alpha,n} + \sum_{\alpha=1}^{L} \sum_n V_{i,\alpha,n} c^\dagger_\alpha d_{i\alpha,n} + H.c. + H_i. \tag{B.11}$$

The operators $c^\dagger_{i\alpha}$ are the impurity fermionic operators while the operators $d^\dagger_{i\alpha,n}$ describe the effective bath to which the local impurity is coupled. The effective bath is defined by the set of energy levels $\epsilon_{i,\alpha,n}$ and bath-impurities hybridizations $V_{i,\alpha,n}$. With this particular choice, the Weiss field is diagonal in the orbital index and read

$$\mathcal{G}^{\alpha\beta}_{0,i}(i\omega_n) = \delta_{\alpha,\beta} \mathcal{G}^{\alpha}_{0,i}(i\omega_n) = \frac{1}{i\omega_n - \Delta_{i,\alpha}(i\omega_n)}, \tag{B.12}$$

where

$$\Delta_{i,\alpha} = \sum_n \frac{V^2_{i,\alpha,n}}{i\omega_n - \epsilon_{i,\alpha,n}}. \tag{B.13}$$

Here we solve the effective impurities using a finite bath discretization and the Exact Diagonalization scheme based on the Lanczos method [146].

B.2 Application to the biased slab

In this section we give few details about the application of the DMFT method to the case of the layered slab in a constant electric-field discussed in Chap. 6. We recall for

convenience the Hamiltonian

$$\begin{aligned}\mathcal{H} = &\sum_{\mathbf{k}_\parallel\sigma}\sum_{z=1}^{N}\hat{c}^\dagger_{\mathbf{k}_\parallel z\sigma}\cdot\boldsymbol{h}_{\mathbf{k}_\parallel}\cdot\hat{c}_{\mathbf{k}_\parallel z\sigma} + \sum_{\mathbf{k}_\parallel\sigma}\sum_{z=1}^{N-1}\hat{c}^\dagger_{\mathbf{k}_\parallel z\sigma}\cdot\boldsymbol{t}_{\mathbf{k}_\parallel}\cdot\hat{c}_{\mathbf{k}_\parallel z+1\sigma} + H.c. \\ &+\frac{\Delta}{2}\sum_{z=1}^{N}\sum_{i\in z}(n_{i,z,1}-n_{i,z,2}) + \frac{U}{2}\sum_{z=1}^{N}\sum_{i\in z}(n_{iz}-2)^2 - \sum_z\sum_{i\in z}V(z)n_{i,z}.\end{aligned} \tag{B.14}$$

In this case we assume translational invariance to hold in the xy planes and introduce an auxiliary impurity problem for each layer

$$\begin{aligned}H^{(z)}_{imp} = &\sum_{\alpha=1,2}\sum_n \epsilon_{z,\alpha,n}d^\dagger_{z,\alpha,n}d_{z,\alpha,n} + \sum_{\alpha=1,2}\sum_n V_{z,\alpha,n}c^\dagger_\alpha d_{z,\alpha,n} + H.c. \\ &+\frac{U}{2}(n-2)^2 - \frac{\Delta}{2}(n_1-n_2) + V(z)n,\end{aligned} \tag{B.15}$$

where $n=\sum_\alpha c^\dagger_\alpha c_\alpha$, Δ is the crystal-field and $V(z)$ the linear potential drop. The DMFT equations are readily obtained inserting the self-energies extracted from the auxiliary impurities B.15 into the lattice Dyson equation. The latter can be defined for each $\mathbf{k}_\parallel$ point building the inverse of the $2N\times 2N$ matrix $\hat{\boldsymbol{G}}_{\mathbf{k}_\parallel}(i\omega_n)$ containing all the 2×2 matrices $\boldsymbol{G}_{\mathbf{k}_\parallel zz'}(i\omega_n)$

$$\hat{\boldsymbol{G}}_{\mathbf{k}_\parallel}(i\omega_n) = \begin{pmatrix}\boldsymbol{G}_{\mathbf{k}_\parallel 11}(i\omega_n) & \boldsymbol{G}_{\mathbf{k}_\parallel 11}(i\omega_n) & \dots \\ \boldsymbol{G}_{\mathbf{k}_\parallel 21}(i\omega_n) & \boldsymbol{G}_{\mathbf{k}_\parallel 22}(i\omega_n) & \dots \\ \vdots & \vdots & \ddots\end{pmatrix}, \tag{B.16}$$

where $\boldsymbol{G}_{\mathbf{k}_\parallel zz'}(i\omega_n)$ is the Fourier transform of

$$\boldsymbol{G}_{\mathbf{k}_\parallel zz'}(\tau) = \begin{pmatrix}-\langle\mathcal{T}_\tau\, c_{z1}(\tau)c^\dagger_{z'1}(0)\rangle & -\langle\mathcal{T}_\tau\, c_{z1}(\tau)c^\dagger_{z'2}(0)\rangle \\ -\langle\mathcal{T}_\tau\, c_{z2}(\tau)c^\dagger_{z'1}(0)\rangle & -\langle\mathcal{T}_\tau\, c_{z2}(\tau)c^\dagger_{z'2}(0)\rangle\end{pmatrix}, \tag{B.17}$$

The z,z' element of the inverse of $\hat{\boldsymbol{G}}_{\mathbf{k}_\parallel}(i\omega_n)$ reads

$$\left(\hat{\boldsymbol{G}}^{-1}_{\mathbf{k}_\parallel}\right)_{zz'}(i\omega_n) = \delta_{zz'}\left[i\omega_n\mathbb{I} - \boldsymbol{h}_{\mathbf{k}_\parallel} - \boldsymbol{\mathcal{H}}_{loc}(z) - \boldsymbol{\Sigma}_z(i\omega_n)\right] - \delta_{z,z\pm1}\boldsymbol{t}_{\mathbf{k}_\parallel}, \tag{B.18}$$

where

$$\boldsymbol{\mathcal{H}}_{loc}(z) = \begin{pmatrix}-\frac{\Delta}{2}-V(z) & 0 \\ 0 & \frac{\Delta}{2}-V(z)\end{pmatrix}. \tag{B.19}$$

Defining the $2L\times 2L$ matrix $\hat{\boldsymbol{T}}_{\mathbf{k}_\parallel}$ which contain all the hopping amplitudes from the layer z and orbital α to the layer z' and orbital α'

$$\hat{\boldsymbol{T}}_{\mathbf{k}_\parallel} = \begin{pmatrix}\boldsymbol{h}_{\mathbf{k}_\parallel} & \boldsymbol{t}_{\mathbf{k}_\parallel} & 0 & 0 & \dots \\ \boldsymbol{t}_{\mathbf{k}_\parallel} & \boldsymbol{h}_{\mathbf{k}_\parallel} & \boldsymbol{t}_{\mathbf{k}_\parallel} & 0 & \dots \\ 0 & \boldsymbol{t}_{\mathbf{k}_\parallel} & \boldsymbol{h}_{\mathbf{k}_\parallel} & \boldsymbol{t}_{\mathbf{k}_\parallel} & \dots \\ 0 & 0 & \ddots & \ddots & \ddots\end{pmatrix} \tag{B.20}$$

we can bring Eq. B.18 in the more compact form

$$\hat{\boldsymbol{G}}^{-1}_{\mathbf{k}_\parallel}(i\omega_n) = i\omega_n \mathbb{I} - \hat{\boldsymbol{T}}_{\mathbf{k}_\parallel} - \hat{\boldsymbol{\mathcal{H}}}_{loc} - \hat{\boldsymbol{\Sigma}}(i\omega_n), \tag{B.21}$$

where $\hat{\boldsymbol{\mathcal{H}}}_{loc}$ and $\hat{\boldsymbol{\Sigma}}(i\omega_n)$ are block diagonal matrices containing all the $\boldsymbol{\mathcal{H}}_{loc}(z)$ and $\boldsymbol{\Sigma}_z(i\omega_n)$ 2×2 matrices. From Eq. (B.21) we build up for each $\mathbf{k}_\parallel$ point the inverse of the $\hat{\boldsymbol{G}}_{\mathbf{k}_\parallel}$ and then compute the local components $\boldsymbol{G}_{\mathbf{k}_\parallel,zz}$ taking the diagonal $L \times L$ blocks of the inverted matrix. The local Green's function for each layer is then extracted summing over all the $\mathbf{k}_\parallel$ points

$$\boldsymbol{G}_{zz}(i\omega_n) = \sum_{\mathbf{k}_\parallel} \boldsymbol{G}_{\mathbf{k}_\parallel,zz}(i\omega_n). \tag{B.22}$$

The full $\mathbf{k}_\parallel$ dependent Green's function $\hat{\boldsymbol{G}}_{\mathbf{k}_\parallel}(i\omega_n)$ is used to compute the kinetic energy of the system, while the potential energy is is straightforwardly obtained from the impurity diagonalization. The explicit expression for the former reads

$$\begin{aligned} E_{kin} &= \sum_{\mathbf{k}_\parallel \sigma} \sum_{z=1}^{N} \langle \hat{c}^\dagger_{\mathbf{k}_\parallel z\sigma} \cdot \boldsymbol{h}_{\mathbf{k}_\parallel} \cdot \hat{c}_{\mathbf{k}_\parallel z\sigma} \rangle + \sum_{\mathbf{k}_\parallel \sigma} \sum_{z=1}^{N-1} \langle \hat{c}^\dagger_{\mathbf{k}_\parallel z\sigma} \cdot \boldsymbol{t}_{\mathbf{k}_\parallel} \cdot \hat{c}_{\mathbf{k}_\parallel z+1\sigma} + H.c. \rangle \\ &= \sum_{\mathbf{k}_\parallel} \mathrm{Tr}\left[\hat{\boldsymbol{T}}_{\mathbf{k}_\parallel} \cdot \hat{\boldsymbol{G}}_{\mathbf{k}_\parallel}(\tau = 0^-) \right] = \sum_{\mathbf{k}_\parallel} \frac{1}{\beta} \sum_{i\omega_n} \mathrm{Tr}\left[\hat{\boldsymbol{T}}_{\mathbf{k}_\parallel} \cdot \hat{\boldsymbol{G}}_{\mathbf{k}_\parallel}(i\omega_n) \right]. \end{aligned} \tag{B.23}$$

In this latter summation over Matsubara frequencies we considered the analytical contribution of the tails of the Green's function to obtain a good accuracy in the energy calculation with respect to the number of frequencies considered.

Bibliography

[1] I. Bloch, J. Dalibard, and W. Zwerger, Rev. Mod. Phys. **80**, 885 (2008).

[2] A. Polkovnikov, K. Sengupta, A. Silva, and M. Vengalattore, Rev. Mod. Phys. **83**, 863 (2011).

[3] T. Kinoshita, T. Wenger, and D. S. Weiss, Nature **440**, 900 (2006).

[4] M. Greiner, O. Mandel, T. W. Hansch, and I. Bloch, Nature **419**, 51 (2002).

[5] F. Krausz and M. Ivanov, Rev. Mod. Phys. **81**, 163 (2009).

[6] T. Brabec and F. Krausz, Rev. Mod. Phys. **72**, 545 (2000).

[7] S. Dal Conte, C. Giannetti, G. Coslovich, F. Cilento, D. Bossini, T. Abebaw, F. Banfi, G. Ferrini, H. Eisaki, M. Greven, A. Damascelli, D. van der Marel, and F. Parmigiani, Science **335**, 1600 (2012), http://www.sciencemag.org/content/335/6076/1600.full.pdf .

[8] P. B. Allen, Phys. Rev. Lett. **59**, 1460 (1987).

[9] C. Giannetti, F. Cilento, S. D. Conte, G. Coslovich, G. Ferrini, H. Molegraaf, M. Raichle, R. Liang, H. Eisaki, M. Greven, A. Damascelli, D. van der Marel, and F. Parmigiani, Nat Commun **2**, 353 (2011).

[10] S. Dal Conte, L. Vidmar, D. Golez, M. Mierzejewski, G. Soavi, S. Peli, F. Banfi, G. Ferrini, R. Comin, B. M. Ludbrook, L. Chauviere, N. D. Zhigadlo, H. Eisaki, M. Greven, S. Lupi, A. Damascelli, D. Brida, M. Capone, J. Bonca, G. Cerullo, and C. Giannetti, Nat Phys **11**, 421 (2015).

[11] C. L. Smallwood, J. P. Hinton, C. Jozwiak, W. Zhang, J. D. Koralek, H. Eisaki, D.-H. Lee, J. Orenstein, and A. Lanzara, Science **336**, 1137 (2012), http://www.sciencemag.org/content/336/6085/1137.full.pdf .

[12] J. Graf, C. Jozwiak, C. L. Smallwood, H. Eisaki, R. A. Kaindl, D.-H. Lee, and A. Lanzara, Nat Phys **7**, 805 (2011).

[13] F. Cilento, S. Dal Conte, G. Coslovich, S. Peli, N. Nembrini, S. Mor, F. Banfi, G. Ferrini, H. Eisaki, M. K. Chan, C. J. Dorow, M. J. Veit, M. Greven, D. van der Marel, R. Comin, A. Damascelli, L. Rettig, U. Bovensiepen, M. Capone, and F. Giannetti, C.and Parmigiani, Nat Commun **5** (2014).

[14] D. Fausti, R. I. Tobey, N. Dean, S. Kaiser, A. Dienst, M. C. Hoffmann, S. Pyon, T. Takayama, H. Takagi, and A. Cavalleri, Science **331**, 189 (2011), http://www.sciencemag.org/content/331/6014/189.full.pdf .

[15] L. Stojchevska, I. Vaskivskyi, T. Mertelj, P. Kusar, D. Svetin, S. Brazovskii, and D. Mihailovic, Science **344**, 177 (2014), http://www.sciencemag.org/content/344/6180/177.full.pdf .

[16] M. Först, R. I. Tobey, H. Bromberger, S. B. Wilkins, V. Khanna, A. D. Caviglia, Y.-D. Chuang, W. S. Lee, W. F. Schlotter, J. J. Turner, M. P. Minitti, O. Krupin, Z. J. Xu, J. S. Wen, G. D. Gu, S. S. Dhesi, A. Cavalleri, and J. P. Hill, Phys. Rev. Lett. **112**, 157002 (2014).

[17] W. Hu, S. Kaiser, D. Nicoletti, C. R. Hunt, I. Gierz, M. C. Hoffmann, M. Le Tacon, T. Loew, B. Keimer, and A. Cavalleri, Nat Mater **13**, 705 (2014), article.

[18] S. Kaiser, C. R. Hunt, D. Nicoletti, W. Hu, I. Gierz, H. Y. Liu, M. Le Tacon, T. Loew, D. Haug, B. Keimer, and A. Cavalleri, Phys. Rev. B **89**, 184516 (2014).

[19] M. Mitrano, A. Cantaluppi, D. Nicoletti, S. Kaiser, A. Perucchi, S. Lupi, P. Di Pietro, D. Pontiroli, M. Riccò, A. Subedi, S. R. Clark, D. Jaksch, and A. Cavalleri, ArXiv e-prints (2015), arXiv:1505.04529 [cond-mat.supr-con] .

[20] R. Mankowsky, A. Subedi, M. Forst, S. O. Mariager, M. Chollet, H. T. Lemke, J. S. Robinson, J. M. Glownia, M. P. Minitti, A. Frano, M. Fechner, N. A. Spaldin, T. Loew, B. Keimer, A. Georges, and A. Cavalleri, Nature **516**, 71 (2014), letter.

[21] S. Iwai, M. Ono, A. Maeda, H. Matsuzaki, H. Kishida, H. Okamoto, and Y. Tokura, Phys. Rev. Lett. **91**, 057401 (2003).

[22] F. Novelli, G. De Filippis, V. Cataudella, M. Esposito, I. Vergara, F. Cilento, E. Sindici, A. Amaricci, C. Giannetti, D. Prabhakaran, S. Wall, A. Perucchi, S. Dal Conte, G. Cerullo, M. Capone, A. Mishchenko, M. Grüninger, N. Nagaosa, F. Parmigiani, and D. Fausti, Nat Commun **5** (2014), article.

[23] L. Perfetti, P. A. Loukakos, M. Lisowski, U. Bovensiepen, H. Berger, S. Biermann, P. S. Cornaglia, A. Georges, and M. Wolf, Phys. Rev. Lett. **97**, 067402 (2006).

[24] D. Wegkamp, M. Herzog, L. Xian, M. Gatti, P. Cudazzo, C. L. McGahan, R. E. Marvel, R. F. Haglund, A. Rubio, M. Wolf, and J. Stähler, Phys. Rev. Lett. **113**, 216401 (2014).

[25] W. J. Hardy, H. Ji, E. Mikheev, S. Stemmer, and D. Natelson, Phys. Rev. B **90**, 205117 (2014).

[26] P. Stoliar, L. Cario, E. Janod, B. Corraze, C. Guillot-Deudon, S. Salmon-Bourmand, V. Guiot, J. Tranchant, and M. Rozenberg, Advanced Materials **25**, 3222 (2013).

[27] C. Zener, Proceedings of the Royal Society of London A: Mathematical, Physical and Engineering Sciences **145**, 523 (1934).

[28] H. Takagi and H. Y. Hwang, Science **327**, 1601 (2010), http://www.sciencemag.org/content/327/5973/1601.full.pdf .

[29] D. M. Newns, J. A. Misewich, C. C. Tsuei, A. Gupta, B. A. Scott, and A. Schrott, Applied Physics Letters **73** (1998).

[30] E. Janod, J. Tranchant, B. Corraze, M. Querr, P. Stoliar, M. Rozenberg, T. Cren, D. Roditchev, V. T. Phuoc, M.-P. Besland, and L. Cario, Advanced Functional Materials , n/a (2015).

[31] T. Fujimoto and K. Awaga, Phys. Chem. Chem. Phys. **15**, 8983 (2013).

[32] H. Shimotani, H. Suzuki, K. Ueno, M. Kawasaki, and Y. Iwasa, Applied Physics Letters **92**, 242107 (2008).

[33] S.-Y. Sung, S.-Y. Kim, K.-M. Jo, J.-H. Lee, J.-J. Kim, S.-G. Kim, K.-H. Chai, S. J. Pearton, D. P. Norton, and Y.-W. Heo, Applied Physics Letters **97**, 222109 (2010).

[34] M. Nakano, K. Shibuya, D. Okuyama, T. Hatano, S. Ono, M. Kawasaki, Y. Iwasa, and Y. Tokura, Nature **487**, 459 (2012).

[35] Y. Taguchi, T. Matsumoto, and Y. Tokura, Phys. Rev. B **62**, 7015 (2000).

[36] S. Yamanouchi, Y. Taguchi, and Y. Tokura, Phys. Rev. Lett. **83**, 5555 (1999).

[37] F. Sabeth, T. Iimori, and N. Ohta, Journal of the American Chemical Society **134**, 6984 (2012), pMID: 22475113, http://dx.doi.org/10.1021/ja302725e .

[38] V. Guiot, L. Cario, E. Janod, B. Corraze, V. Ta Phuoc, M. Rozenberg, P. Stoliar, T. Cren, and D. Roditchev, Nat. Commun. **4**, 1722 (2013).

[39] A. Camjayi, C. Acha, R. Weht, M. G. Rodríguez, B. Corraze, E. Janod, L. Cario, and M. J. Rozenberg, Phys. Rev. Lett. **113**, 086404 (2014).

[40] M. Yoshida, R. Suzuki, Y. Zhang, M. Nakano, and Y. Iwasa, ArXiv e-prints (2015), arXiv:1505.04038 [cond-mat.mtrl-sci] .

[41] P. Calabrese and J. Cardy, Journal of Statistical Mechanics: Theory and Experiment **2007**, P06008 (2007).

[42] M. Rigol, V. Dunjko, and M. Olshanii, Nature **452**, 854 (2008).

[43] M. Rigol, V. Dunjko, V. Yurovsky, and M. Olshanii, Phys. Rev. Lett. **98**, 050405 (2007).

[44] M. Moeckel and S. Kehrein, Phys. Rev. Lett. **100**, 175702 (2008).

[45] J. Berges, S. Borsányi, and C. Wetterich, Phys. Rev. Lett. **93**, 142002 (2004).

[46] A. Maraga, A. Silva, and M. Fabrizio, Phys. Rev. B **90**, 155131 (2014).

[47] G. Carleo, F. Becca, M. Schiró, and M. Fabrizio, Sci. Rep. **2** (2012), 10.1038/srep00243.

[48] M. Eckstein, M. Kollar, and P. Werner, Phys. Rev. Lett. **103**, 056403 (2009).

[49] M. Schiró and M. Fabrizio, Phys. Rev. Lett. **105**, 076401 (2010).

[50] B. Sciolla and G. Biroli, Phys. Rev. Lett. **105**, 220401 (2010).

[51] M. Sandri and M. Fabrizio, Phys. Rev. B **88**, 165113 (2013).

[52] M. Heyl, A. Polkovnikov, and S. Kehrein, Phys. Rev. Lett. **110**, 135704 (2013).

[53] P. Smacchia, M. Knap, E. Demler, and A. Silva, Phys. Rev. B **91**, 205136 (2015).

[54] A. Gambassi and P. Calabrese, EPL (Europhysics Letters) **95**, 66007 (2011).

[55] M. Behrmann, M. Fabrizio, and F. Lechermann, Phys. Rev. B **88**, 035116 (2013).

[56] B. Sciolla and G. Biroli, Phys. Rev. B **88**, 201110 (2013).

[57] A. Das, K. Sengupta, D. Sen, and B. K. Chakrabarti, Phys. Rev. B **74**, 144423 (2006).

[58] B. Sciolla and G. Biroli, Journal of Statistical Mechanics: Theory and Experiment **2011**, P11003 (2011).

[59] N. Tsuji, M. Eckstein, and P. Werner, Phys. Rev. Lett. **110**, 136404 (2013).

[60] P. Werner, N. Tsuji, and M. Eckstein, Phys. Rev. B **86**, 205101 (2012).

[61] M. Eckstein and P. Werner, Phys. Rev. B **84**, 035122 (2011).

[62] M. Eckstein and P. Werner, Phys. Rev. Lett. **110**, 126401 (2013).

[63] A. Rosch, D. Rasch, B. Binz, and M. Vojta, Phys. Rev. Lett. **101**, 265301 (2008).

[64] R. Sensarma, D. Pekker, E. Altman, E. Demler, N. Strohmaier, D. Greif, R. Jördens, L. Tarruell, H. Moritz, and T. Esslinger, Phys. Rev. B **82**, 224302 (2010).

[65] M. Sandri and M. Fabrizio, Phys. Rev. B **91**, 115102 (2015).

[66] M. Sandri, M. Capone, and M. Fabrizio, Phys. Rev. B **87**, 205108 (2013).

[67] A. Amaricci, C. Weber, M. Capone, and G. Kotliar, Phys. Rev. B **86**, 085110 (2012).

[68] J. E. Han and J. Li, Phys. Rev. B **88**, 075113 (2013).

[69] J. E. Han, Phys. Rev. B **87**, 085119 (2013).

[70] J. K. Freericks, Phys. Rev. B **77**, 075109 (2008).

[71] M. Eckstein and P. Werner, Phys. Rev. Lett. **107**, 186406 (2011).

[72] J. H. Davies and J. W. Wilkins, Phys. Rev. B **38**, 1667 (1988).

[73] C. Aron, G. Kotliar, and C. Weber, Phys. Rev. Lett. **108**, 086401 (2012).

[74] J. Li, C. Aron, G. Kotliar, and J. E. Han, Phys. Rev. Lett. **114**, 226403 (2015).

[75] T. Oka, R. Arita, and H. Aoki, Phys. Rev. Lett. **91**, 066406 (2003).

[76] M. Mierzejewski, L. Vidmar, J. Bonča, and P. Prelovšek, Phys. Rev. Lett. **106**, 196401 (2011).

[77] E. Arrigoni, M. Knap, and W. von der Linden, Phys. Rev. Lett. **110**, 086403 (2013).

[78] L. Vidmar, J. Bonča, T. Tohyama, and S. Maekawa, Phys. Rev. Lett. **107**, 246404 (2011).

[79] C. Zener, Proceedings of the Royal Society of London A: Mathematical, Physical and Engineering Sciences **137**, 696 (1932).

[80] L. D. Landau, Phys. Z. Sowjetunion **2**, 46 (1932).

[81] T. Oka and H. Aoki, Phys. Rev. Lett. **95**, 137601 (2005).

[82] U. Schollwöck, Rev. Mod. Phys. **77**, 259 (2005).

[83] S. R. White and A. E. Feiguin, Phys. Rev. Lett. **93**, 076401 (2004).

[84] J. Schwinger, Phys. Rev. **82**, 664 (1951).

[85] Z. Lenarčič and P. Prelovšek, Phys. Rev. Lett. **108**, 196401 (2012).

[86] S. Okamoto, Phys. Rev. B **76**, 035105 (2007).

[87] S. Okamoto, Phys. Rev. Lett. **101**, 116807 (2008).

[88] M. Eckstein, T. Oka, and P. Werner, Phys. Rev. Lett. **105**, 146404 (2010).

[89] M. Eckstein and P. Werner, Phys. Rev. B **88**, 075135 (2013).

[90] M. Srednicki, Phys. Rev. E **50**, 888 (1994).

[91] J. M. Deutsch, Phys. Rev. A **43**, 2046 (1991).

[92] V. Bapst and G. Semerjian, Journal of Statistical Mechanics: Theory and Experiment **2012**, P06007 (2012).

[93] M. Sandri, M. Schiró, and M. Fabrizio, Phys. Rev. B **86**, 075122 (2012).

[94] N. Tsuji, T. Oka, H. Aoki, and P. Werner, Phys. Rev. B **85**, 155124 (2012).

[95] N. Tsuji, T. Oka, P. Werner, and H. Aoki, Phys. Rev. Lett. **106**, 236401 (2011).

[96] M. Schiró and M. Fabrizio, Phys. Rev. B **83**, 165105 (2011).

[97] M. Fabrizio, in New Materials for Thermoelectric Applications: Theory and Experiment, edited by V. Zlatic and A. Hewson (Springer Netherlands, 2013) pp. 247–273.

[98] N. Lanatà, P. Barone, and M. Fabrizio, Phys. Rev. B **80**, 224524 (2009).

[99] P. André, M. Schiró, and M. Fabrizio, Phys. Rev. B **85**, 205118 (2012).

[100] M. Eckstein and P. Werner, Phys. Rev. Lett. **113**, 076405 (2014).

[101] F. Rodolakis, B. Mansart, E. Papalazarou, S. Gorovikov, P. Vilmercati, L. Petaccia, A. Goldoni, J. P. Rueff, S. Lupi, P. Metcalf, and M. Marsi, Phys. Rev. Lett. **102**, 066805 (2009).

[102] G. Borghi, M. Fabrizio, and E. Tosatti, Phys. Rev. Lett. **102**, 066806 (2009).

[103] G. Borghi, M. Fabrizio, and E. Tosatti, Phys. Rev. B **81**, 115134 (2010).

[104] M. Charlebois, S. R. Hassan, R. Karan, D. Sénéchal, and A.-M. S. Tremblay, Phys. Rev. B **87**, 035137 (2013).

[105] L. Chen and J. K. Freericks, Phys. Rev. B **75**, 125114 (2007).

[106] A. Branschdel, G. Schneider, and P. Schmitteckert, Annalen der Physik **522**, 657 (2010).

[107] N. Lanatà, Phys. Rev. B **82**, 195326 (2010).

[108] H. Zenia, J. K. Freericks, H. R. Krishnamurthy, and T. Pruschke, Phys. Rev. Lett. **103**, 116402 (2009).

[109] Y. Tanaka and K. Yonemitsu, Phys. Rev. B **83**, 085113 (2011).

[110] J. Hubbard, Proc. R. Soc. of London A **276**, 238 (1963).

[111] M. C. Gutzwiller, Phys. Rev. Lett. **10**, 159 (1963).

[112] J. Kanamori, Progress of Theoretical Physics **30**, 275 (1963).

[113] N. F. Mott, Proc. Phys. Soc. A **62**, 416 (1949).

[114] M. Imada, A. Fujimori, and Y. Tokura, Rev. Mod. Phys. **70**, 1039 (1998).

[115] A. Georges, G. Kotliar, W. Krauth, and M. J. Rozenberg, Rev. Mod. Phys. **68**, 13 (1996).

[116] J. Zaanen, G. A. Sawatzky, and J. W. Allen, Phys. Rev. Lett. **55**, 418 (1985).

[117] I. H. Inoue and M. J. Rozenberg, Advanced Functional Materials **18**, 2289 (2008).

[118] M. Potthoff and W. Nolting, Phys. Rev. B **59**, 2549 (1999).

[119] P. Werner and A. J. Millis, Phys. Rev. Lett. **99**, 126405 (2007).

[120] N. Manini, G. E. Santoro, A. Dal Corso, and E. Tosatti, Phys. Rev. B **66**, 115107 (2002).

[121] P. Werner and A. J. Millis, Phys. Rev. B **75**, 085108 (2007).

[122] M. C. Gutzwiller, Phys. Rev. **134**, A923 (1964).

[123] M. C. Gutzwiller, Phys. Rev. **137**, A1726 (1965).

[124] E. H. Lieb and F. Y. Wu, Phys. Rev. Lett. **20**, 1445 (1968).

[125] W. F. Brinkman and T. M. Rice, Phys. Rev. B **2**, 4302 (1970).

[126] M. J. Rozenberg, X. Y. Zhang, and G. Kotliar, Phys. Rev. Lett. **69**, 1236 (1992).

[127] X. Y. Zhang, M. J. Rozenberg, and G. Kotliar, Phys. Rev. Lett. **70**, 1666 (1993).

[128] J. Bünemann, W. Weber, and F. Gebhard, Phys. Rev. B **57**, 6896 (1998).

[129] N. Lanatà, H. U. R. Strand, X. Dai, and B. Hellsing, Phys. Rev. B **85**, 035133 (2012).

[130] G. Kotliar, S. Y. Savrasov, K. Haule, V. S. Oudovenko, O. Parcollet, and C. A. Marianetti, Rev. Mod. Phys. **78**, 865 (2006).

[131] G. Borghi, M. Fabrizio, and E. Tosatti, Phys. Rev. B **90**, 125102 (2014).

[132] H. Aoki, N. Tsuji, M. Eckstein, M. Kollar, T. Oka, and P. Werner, Rev. Mod. Phys. **86**, 779 (2014).

[133] G. Mazza and M. Fabrizio, Phys. Rev. B **86**, 184303 (2012).

[134] W. Metzner and D. Vollhardt, Phys. Rev. Lett. **62**, 324 (1989).

[135] J. Bünemann, F. Gebhard, and R. Thul, Phys. Rev. B **67**, 075103 (2003).

[136] F. Lechermann, A. Georges, G. Kotliar, and O. Parcollet, Phys. Rev. B **76**, 155102 (2007).

[137] H. Brunner and P.J. van der Houven, The numerical solution of Volterra Equations (North-Holland, Amsterdam, 1986).

[138] G. Kotliar and A. E. Ruckenstein, Phys. Rev. Lett. **57**, 1362 (1986).

[139] S. Florens and A. Georges, Phys. Rev. B **66**, 165111 (2002).

[140] L. de'Medici, A. Georges, and S. Biermann, Phys. Rev. B **72**, 205124 (2005).

[141] A. Rüegg, S. D. Huber, and M. Sigrist, Phys. Rev. B **81**, 155118 (2010).

[142] W. Metzner, Phys. Rev. B **43**, 8549 (1991).

[143] E. Mller-Hartmann, Zeitschrift fr Physik B Condensed Matter **74**, 507 (1989).

[144] M. H. Hettler, A. N. Tahvildar-Zadeh, M. Jarrell, T. Pruschke, and H. R. Krishnamurthy, Phys. Rev. B **58**, R7475 (1998).

[145] G. Kotliar, S. Y. Savrasov, G. Pálsson, and G. Biroli, Phys. Rev. Lett. **87**, 186401 (2001).

[146] C. Lanczos, Journal of Research of the National Bureau of Standards **45**, 255 (1950).